Tissue-sparing of Proton Minibeam Therapy depends on beam size, fractionation scheme and interlacing geometry

M. Sc. Matthias Sammer

Vollständiger Abdruck der von der Fakultät für Luft– und Raumfahrttechnik der Universität der Bundeswehr München zur Erlangung des akademischen Grades eines

Doktors der Naturwissenschaften (Dr. rer. nat.)

genehmigten Dissertation.

Vorsitzender: Prof. Dr. rer. nat. Michael Pfitzner
1. Gutachter: Prof. Dr. rer. nat. Günther Dollinger
2. Gutachter: Prof. Dr. rer. nat. Oliver Jäkel

Die Dissertation wurde am 04.03.2021 bei der Universität der Bundeswehr München eingereicht und durch die Fakultät für Luft– und Raumfahrttechnik am 27.07.2021 angenommen. Die mündliche Prüfung fand am 18.10.2021 statt.

Abstract

Proton Minibeam Radiotherapy (pMBRT) is a spatial fractionation method that widens the therapeutic window in the radiation therapy of cancers. Sub-millimeter planar or pencil proton beams (minibeams) are applied to the patient with a few mm center-to-center distances (*ctc*). Due to the small-angle scattering of protons, the sub-millimeter beams increase in size with depth. Adjusting the *ctc* distances to the tumor depth and its size yields an overlapping, up to homogeneous dose distribution in the tumor volume. Therefore, a tumor dose coverage as in conventional radiotherapy approaches can be maintained while the minibeam pattern within the entrance channel spares healthy tissues and reduces side effects due to the low dose regions in the valleys between the minibeams.

The goal of this work was to improve the understanding of the sparing potential of spatial fractionation by conducting experiments at the ion microprobe SNAKE as well as further developing proton minibeams based on theoretical dose and cell survival calculations.

In the first experiment, the dependence of the radiation response on the dose modulation within an in-vivo mouse ear model of healthy BALB/c mice was investigated. Proton pencil minibeam sizes from $\sigma = 95$ µm to $\sigma = 883$ µm (standard deviation) were applied with a 60 Gy mean dose on a 4×4 grid with 1.8 mm center-to-center distance *ctc*, corresponding to σ/ctc ratios between 0.05 and 0.5. The largest σ/ctc of 0.5 corresponds to a homogeneous irradiation. The results provide an insight into the sparing effect of different dose distributions of minibeam irradiations as they could be applied on the skin or as they occur in depth due to the lateral spread of the minibeams. Visible skin reactions and ear swelling were observed for 90 days post-irradiation. The results state that the closer the dose modulation is to that of a homogeneous irradiation ($\sigma/ctc = 0.5$), the stronger the tissue toxicities. Transferred to patient irradiation, the tissue-sparing potential of proton minibeams decreases with depth but proton minibeams are still superior to conventional proton irradiations even at large depths. The σ/ctc ratio without any side effects in the mouse model was extrapolated to $\sigma/ctc = 0.032$.

In the second animal trial, the combination of temporal and spatial fractionation

was studied within the BALB/c mouse ear model. Four daily fractions of 30 Gy mean dose were applied to the ears with 16 proton minibeams ($\sigma = 222$ µm; $ctc = 1.8$ mm). The minibeams were reirradiated accurately (fractionation scheme 1; FS1) or with a maximum spatial shift between the temporal fractions (FS2). The third irradiation group (FS3) accurately reirradiated the resulting 64 proton minibeam positions from FS2 ($\sigma = 222$ µm; $ctc = 0.9$ mm) with 30 Gy mean dose per fraction. Due to the halving of the *ctc* in FS3, the daily dose distribution changed with increased valley doses compared to FS1 and FS2. However, the integral dose distributions after the full treatment were equal to the integral dose distribution of FS2, allowing to evaluate the influence of different daily dose distributions. The achieved reirradiation accuracy of (110 ± 52) µm led to a maximum ear swelling of only 1.6-fold for the strongly modulated dose distributions of FS1. The irradiation with maximally shifted minibeams (FS2) led to a swelling of 2.4-fold ear thickness compared to sham irradiated ears. The accurate irradiation of the weaker dose modulations of FS3 yielded even three times the ear thickness of sham irradiated ears. An increased ear thickness was found for FS2 (~ 1.4-fold) and FS3 (~ 1.7-fold) ears at the end of the observational period of 160 days. In FS2 and FS3, histological sections confirmed a significantly increased amount of fibrotic tissue at the end of the observational period. The results suggest that most tissue-sparing in temporally fractionated proton minibeam therapy is achieved for accurate reirradiation of strong daily dose modulations (FS1). The same daily dose modulations as in FS1 but maximally shifted (FS2) are also of advantage compared to accurately reirradiated but weaker dose modulations (FS3). Hence, fractionated proton minibeam therapy presumably also has an advantage over fractionated conventional radiotherapy.

In theoretical proton minibeam dose calculations, further developments and potential application variations were considered. In a 5 cm thick tumor located at 10 cm depth, interlaced minibeams from two opposing or four orthogonal directions were calculated to maximize the clonogenic cell survival. Additionally, the combination of interlacing and heterogeneous tumor dose was examined to evaluate optimized tissue-sparing capabilities at the close tumor vicinity. The computed dose distributions were biologically weighted by the calculated clonogenic cell survival. Interlacing proton minibeams with homogeneous tumor irradiation was only of minor benefit in terms of mean clonogenic cell survival compared to unidirectional minibeam irradiations. Allowing a heterogeneous dose distribution within the tumor enabled larger *ctc* distances between the minibeams. This resulted in enhanced cell survival even for an elevated mean tumor dose, which was necessary to cover the tumor with a prescribed minimum dose. Interlaced minibeams with at least 10 Gy minimum tumor dose could still maintain a mean cell survival of up to 47 % even close to the tumor margin. According to

the calculations, the sparing-effect of proton minibeams is of most advantage for high dose fractions, which brings hypo- or even single-fractionated radiotherapy into reach. Similar benefits as for proton minibeams are expected for heavy-ion minibeams with the advantage of lower scattering and, therefore, smaller, less harmful minibeams in deeper tissues.

The elaborated results within this thesis elucidate in detail the sparing potential of proton Minibeam Radiotherapy. The resolution of proton minibeam dose distributions and their effect on biological tissue paves the way for a deeper understanding of the sparing potential of spatial fractionation. A first-of-its-kind temporal fractionation of proton minibeams suggests that the sparing effect of minibeam irradiation is preserved also when fractionated compared to conventional radiotherapy. Substantial improvements to conventional radiotherapy are revealed by dose simulations. Nevertheless, the experimental results need to be validated in other and human tissues. The theoretical cell survival calculations must also be placed in the context of a complex biological system. Furthermore, the technical feasibility of a clinically applicable proton or heavy ion minibeam needs to be elucidated, in particular for potential interlaced irradiation approaches.

Zusammenfassung

Die Protonen-Minibeamtherapie ist eine räumliche Fraktionierungsmethode der Strahlentherapie von Tumoren um das therapeutische Fenster zu erweitern. Die submillimeter großen Protonenbeams (Minibeams) werden als planare oder Pencil Beams mit einem Abstand (Mitte zu Mitte; engl.: center-to-center *ctc*) von wenigen mm auf den Patienten appliziert. Aufgrund der Kleinwinkelstreuung der Protonen weiten diese Kanäle mit zunehmender Tiefe auf und erlauben, durch die Anpassung der *ctc*-Abstände an die Tumortiefe und Tumorgröße, eine überlappende und bis zu homogene Dosisverteilung im Tumorvolumen. Somit kann der Tumor wie bei der konventionellen Strahlentherapie homogen bestrahlt werden, gleichzeitig sorgt das Minibeammuster, aufgrund der Niedrigdosisbereiche zwischen den Minibeams, für eine Schonung des gesunden Gewebes und führt zur Reduzierung der Nebenwirkungen.

Ziel dieser Arbeit war es, sowohl das Verständnis der räumlichen Fraktionierung im Hinblick auf die Gewebeschonung durch Experimente am Rasterionenmikroskop SNAKE zu verbessern, als auch die Protonen-Minibeamtherapie mit Hilfe von theoretischen Dosis- und Zellüberlebensberechnungen weiterzuentwickeln.

Im ersten Experiment wurde die Abhängigkeit von unterschiedlichen Protonen-Minibeam-Dosismodulationen und ihrer biologischen Strahlenantwort in einem in-vivo-Mausohrmodell gesunder BALB/c-Mäuse untersucht. Die Strahlgrößen der Pencil Minibeams von $\sigma = 95$ µm bis $\sigma = 883$ µm (Standardabweichung) wurden auf einem 4×4-Gitter mit 1,8 mm Gitterabstand (*ctc*) und einer mittleren Dosis von 60 Gy appliziert. Die Minibeammuster entsprachen dabei σ/ctc-Verhältnissen zwischen 0,05 und 0,5, wobei ein σ/ctc von 0,5 (oder größer) einer homogenen Bestrahlung gleichzusetzen ist. Die Ergebnisse dieser Mausstudie geben einen Einblick in die schonende Wirkung unterschiedlicher Dosisverteilungen von Minibeam-Bestrahlungen, so wie sie entweder auf der Haut appliziert werden können oder aufgrund der Aufstreuung der Minibeams mit zunehmender Tiefe auftreten. Sichtbare Hautreaktionen und Ohrschwellungen wurden für 90 Tage nach Bestrahlung beobachtet und gemessen. Dabei zeigte sich, dass die auftretenden Gewebetoxizitäten mit schwächer werdender Dosismodulation bzw. Annäherung an eine homogene Bestrahlung ($\sigma/ctc = 0{,}5$) zunahmen. Das Gewebeschonungspotenzial der Protonen-Minibeam-Bestrahlung nimmt also mit der Tiefe ab, ist

aber der konventionellen Bestrahlung mit Protonen über den gesamten Eintrittskanal überlegen. Das σ/ctc-Verhältnis ohne jegliche Nebenwirkungen im Mausohrmodell konnte zu $\sigma/ctc = 0{,}032$ extrapoliert werden.

Im zweiten Tierversuch wurde ebenfalls das Ohrmodell der BALB/c-Maus verwendet um die Kombination aus zeitlicher und räumlicher Fraktionierung zu untersuchen. Vier Fraktionen wurden im Abstand von 24 h mit 16 Protonen-Minibeams ($\sigma = 222$ µm; $ctc = 1{,}8$ mm) und einer mittleren Dosis von 30 Gy pro Fraktion bestrahlt. Die Minibeams wurden exakt (FS1) oder mit einer maximalen räumlichen Verschiebung zwischen den zeitlichen Fraktionen (FS2) wiederbestrahlt. In der dritten Bestrahlungsgruppe (FS3) wurden die resultierenden 64 Protonen-Minibeam-Positionen aus FS2 ($\sigma = 222$ µm; $ctc = 0{,}9$ mm) ebenfalls mit 30 Gy mittlerer Dosis pro Fraktion exakt wiederbestrahlt. Der halbe Gitterabstand (ctc) in FS3 veränderte die tägliche Dosisverteilung zu erhöhten Dosen zwischen den Minibeams im Vergleich zu FS1 und FS2, wobei die integrale Dosisverteilung nach der vollständigen Behandlung identisch mit der integralen Dosisverteilung von FS2 war. Dadurch konnte der Einfluss der Dosisverteilung pro Fraktion bewertet werden. Die Wiederbestrahlungsgenauigkeit betrug (110 ± 52) µm mit welcher die Bestrahlung der stark modulierten Dosisverteilungen von FS1 zu einer maximalen Ohrschwellung von nur 1,6-mal der Kontrollgruppe resultierte. Die Bestrahlung mit maximal verschobenen Minibeams (FS2) führte zu einer 2,4-fachen Ohrschwellung im Vergleich zur Kontrollgruppe (sham). Die genaue Bestrahlung mit den schwächeren Dosismodulationen von FS3 ergab sogar eine dreifache Ohrdicke im Vergleich zur sham-Gruppe. Eine erhöhte Ohrdicke wurde sowohl für die FS2 ($\sim 1{,}4$-fach) also auch für die FS3 ($\sim 1{,}7$-fach) Gruppe am Ende der Beobachtungszeit von 160 Tagen gefunden. In FS2 und FS3 wurden durch histologische Schnitte eine signifikant erhöhte Menge an fibrotischem Gewebe nachgewiesen. Die Ergebnisse deuten darauf hin, dass die größte Gewebeschonung bei der zeitlich fraktionierten Protonen-Minibeam-Bestrahlung bei genauer Wiederbestrahlung mit starken Dosismodulationen erreicht wird (FS1). Das maximale Verschieben pro Fraktion der gleichen, starken Dosismodulationen wie in FS1 (FS2) ist weiterhin von Vorteil, verglichen mit der genauen Wiederbestrahlung einer schwächeren Dosismodulationen (FS3). Zudem ist zu erwarten, dass die zeitlich fraktionierte Protonen-Minibeam-Therapie einen Vorteil gegenüber der fraktionierten konventionellen Strahlentherapie hat.

Im letzten Teil dieser Arbeit wurden Weiterentwicklungen und mögliche Anwendungsvarianten von Protonen-Minibeams anhand von theoretischen Dosisberechnungen betrachtet und bewertet. Dazu wurde ein 5 cm dicker Tumor als Modell angenommen, der sich in 10 cm Tiefe befand. Es wurde eine Bestrahlungsplanung für aus zwei gegenüberliegenden oder vier orthogonalen Richtungen mit ineinander verschachtel-

ten (engl.: interlaced) Minibeams berechnet. Zusätzlich wurde die Kombination von verschachtelten Minibeams und heterogener Tumordosis untersucht. Die Dosisberechnungen wurden in ein klonogenes Zellüberleben übersetzt, um ein optimiertes Zell-überleben in unmittelbarer Tumornähe zu evaluieren. Die Verschachtelung von Protonen-Minibeams in Kombination mit homogener Tumorbestrahlung erzielte nur geringe Vorteile für das mittlere klonogene Zellüberleben im Vergleich zur „herkömmlichen" Minibeam-Bestrahlung aus nur einer Richtung (unidirektional). Wurden heterogene Dosisverteilungen unter der Voraussetzung einer Mindestdosis innerhalb des Tumors erlaubt, konnten größere *ctc*-Abstände zwischen den Minibeams gewählt werden. Dies führte zu einem verbesserten Zellüberleben trotz einer erhöhten mittleren Tumordosis, welche notwendig ist, um den Tumor mit der vorgeschriebenen Mindestdosis abzudecken. Verschachtelte Minibeams mit einer minimalen Tumordosis von mindestens 10 Gy konnten auch in der Nähe des Tumorrandes noch ein mittleres Zellüberleben von bis zu 47 % erreichen. Den Berechnungen zufolge ist die Schonung durch Protonen-Minibeams vor allem bei hohen Dosisfraktionen von Vorteil und erlaubt möglicherweise eine hypofraktionierte Strahlentherapie oder sogar eine kurative Einzelfraktion. Ähnliche Vorteile wie für Minibeams mit Protonen werden ebenfalls für Schwerionen erwartet, welche den zusätzlichen Vorteil einer geringeren Aufstreuung haben und damit geringerer Schaden der einzelnen Minibeams zu erwarten ist.

Die im Rahmen dieser Dissertation erarbeiteten Ergebnisse zeigen im Detail das Schonungspotential der Protonen-Minibeam-Therapie. Eine differenzierte Auflösung der Protonen-Minibeam-Dosisverteilungen und deren Wirkung auf biologisches Gewebe ebnet den Weg für ein tieferes Verständnis der Schonungseffekte durch räumliche Fraktionierung. Eine erstmalige zeitliche Fraktionierung von Protonen-Minibeams deutet darauf hin, dass die schonende Wirkung der Minibeambestrahlung auch bei Fraktionierung im Vergleich zur konventionellen Strahlentherapie erhalten bleibt. Wesentliche Verbesserungen gegenüber der konventionellen Strahlentherapie konnten durch Dosis-Simulationen aufgezeigt werden. Dennoch müssen die experimentellen Ergebnisse in weiteren sowie menschlichen Gewebearten validiert werden. Die theoretischen Zellüberlebensberechnungen müssen in den Kontext eines komplexen biologischen Systems gestellt werden. Darüber hinaus muss die technische Machbarkeit eines klinisch einsetzbaren Protonen- oder Schwerionen-Minibeams geklärt werden, insbesondere für mögliche verschachtelte Minibeam-Bestrahlungsansätze.

Abbreviations

ctc	center-to-center
FCT	Fibrous Connective Tissue
FS	fractionation scheme
ICRU	International Commitee for Radiation Units
LET	Linear Energy Transfer
LQ-model	Linear-Quadratic model
MCS	Multiple Coulomb Scattering
MRT	Microchannel Radiation Therapy
NTCP	Normal Tissue Complication Probability
OAR	Organ At Risk
pMBRT	proton Minibeam Radiation Therapy
PVDR	Peak-to-Valley Dose Ratio
RBE	Relative Biological Effectiveness
SNAKE	Superconducting Nanoscope for Applied nuclear physics (german: Kernphysikalische) Experiments
SOBP	Spread-Out Bragg Peak
TCP	Tumor Control Probability

Contents

Chapter 1

Introduction

The second leading cause of death with about 9.6 million deaths in 2018 is caused by cancer according to the WHO [1]. One of the main treatment approaches for cancer in developed countries is radiotherapy. Around 50 % of cancer patients can benefit from the treatment with ionizing radiation [2]. The idea behind radiotherapy is the application of a sufficient amount of radiation dose to every tumor cell in a cancerous volume. If the dose is sufficiently high the ionizations cause damage to cell structures, e.g. the sensitive DNA, and further tumor development is prevented. However, the radiation damage does not only affect the tumor volume but also healthy tissues. Dependent on the type of radiotherapy, the close surroundings, e.g. in brachytherapy, or the whole entrance channel as in external beam radiotherapy can be affected. The side effects caused by the radiation damage can be a limiting factor to the tumor dose, especially if sensitive organs, so-called Organs At Risk (OAR) are close to the treated volume [3]. The main goal of radiotherapy can therefore be stated as the compromise between high enough tumor dose for tumor control and the least possible side effects. Improving radiotherapy can be achieved easiest, if not only, by reducing side effects in healthy tissue.

At current state, the main radiation source to treat cancer patients is external Megavoltage X-rays. The second most established form of external radiotherapy is hadron therapy, especially with protons. While X-rays follow an exponential dose decrease with depth after the build-up region, hadrons deposit their energy in a Bragg curve (cf. Fig. 1.1). Most of the energy of a particle is deposited at the end of its range, which is usually planned to be within the target volume by adjusting the initial energy of the particle. Due to the inherent advantage of the Bragg curve in its dose deposition, hadron therapy deposits less integral dose to the healthy tissue than X-ray therapy for similar tumor dosage.

To reduce the local dose in the entrance channel, irradiation from several directions

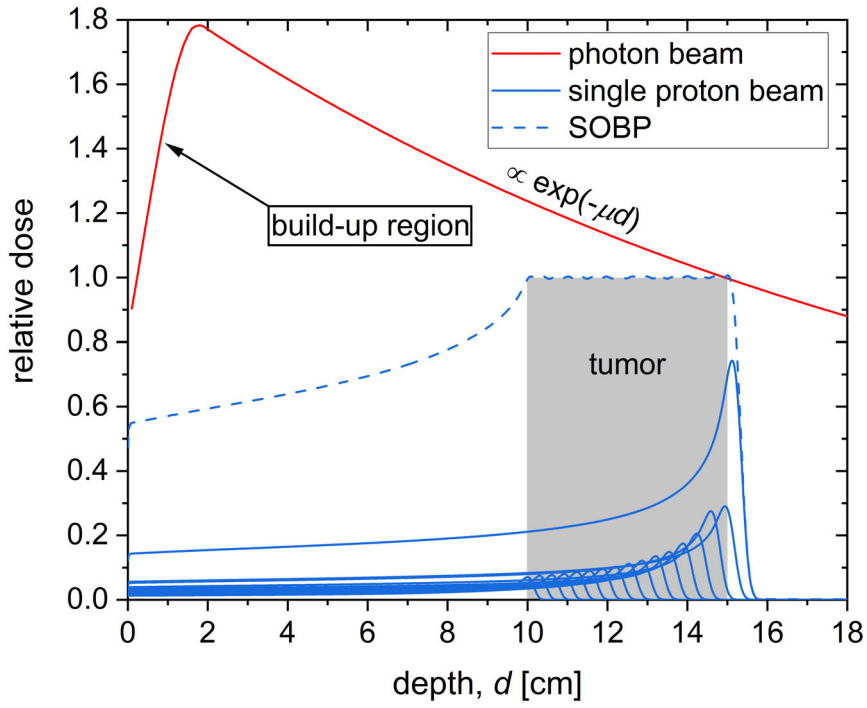

Figure 1.1: *Schematic depth-dose curves for X-rays (red line) and protons (blue lines). After the build-up region, an exponential decrease is found for X-rays with dependence on the material specific attenuation coefficient μ. The solid blue lines represent the mono-energetic proton beams. The sum of properly weighted proton beams is called Spread-Out Bragg Peak (SOBP), which ensures a homogeneous tumor coverage in depth.*

is commonly used and an overlap in the tumor volume causes a dose escalation. Parts of the entrance channel can additionally be spared by combining the irradiation from several directions with modulating the beam intensity. The two latest techniques in X-ray therapy are the Intensity Modulated Radiation Therapy (IMRT) and the Volumetric Modulated Arc Therapy (VMAT) with the difference of a rotating (VMAT) and fixed positioned (IMRT) radiation source during irradiation. In IMRT, the intensity modulation is obtained by collimation, whereas in VMAT, the intensity modulation is achieved by adjusting the rotation speed of the X-ray source. In particle therapy approaches, the intensity modulation can also be applied by using spot scanning systems. However, due to the more complex beam delivery of heavy particles (e.g. protons, carbon ions), the number of incidence angles is limited compared to photons, but the inherent physical advantages remain(see Fig. 1.1). An evaluation between conventional

X-ray versus conventional proton therapy is highly complex and often ambiguous [4], which makes the long-term concurrent existence of both techniques comprehensible. However, the number of particle therapy centers is rapidly increasing, with 111 centers currently operating, additionally 35 under construction and 28 in the planning stage according to the PTCOG (Particle Therapy Co-Operative Group) website as of February 2021 [5].

In modern radiotherapy, the curative dose is applied in multiple fractions, called temporal fractionation, to reduce tissue toxicities. A tumor is typically irradiated five times a week for several weeks with $\sim 2\,\mathrm{Gy}$/fraction in conventional radiotherapy [6], but schedule and dosage can differ with tumor type. In between the temporal fractions, the healthy tissue can recover whereas tumors are sensitized to radiation [7, 8], resulting in a gentle but efficient treatment.

Besides the modern techniques to reduce side effects in conventional radiotherapy, a promising attempt to reduce healthy tissue toxicities even further is spatial fractionation. Spatial fractionation was already proposed as early as 1909 by Alban Köhler in the form of grid therapy [9]. He suggests that using a kilovoltage X-ray tube with a large focal spot (1 - 1.5 cm) in a few cm distance to a grid out of metal wires (mesh size ~ 1 - 2 mm) laying on the skin spares healthy tissue. Moreover, due to the large focal spot, a homogeneous dose distribution is applied to the tumor [9]. The resistance of healthy tissue to higher doses of grid irradiation compared to conventional irradiation was proven in patients by Köhler [10] and used for several decades as an irradiation method [11–14]. However, when using photons of higher energies and filters for beam hardening, severe skin ulcers, one of the most concerning side effects in early radiotherapy, can also be prevented. Therefore, grid therapy has eventually been abandoned and substituted by megavoltage radiotherapy. For palliative purposes, GRID therapy is used in combination with megavoltage X-rays to relieve symptoms for patients with massive or recurring tumors [15].

The principle of sparing healthy tissue by spatial fractionation is mainly based on the dose-volume effect [16, 17]. The dose-volume effect describes the higher dose tolerance for decreasing irradiation volumes. Detailed underlying mechanisms are still not fully understood, although first studies using microbeams were already carried-out at the Brookhaven National Laboratory in the 1960s [18, 19]. Fast tissue repair effects, especially for capillaries [20], as well as the higher resistance of capillaries [21] to radiation may also add to the dose-volume effect and the higher tissue tolerance. The high resistance of tissues to small beams has led to the development of Microchannel Radiation Therapy (MRT) at the Brookhaven National Laboratory [22] and the European Synchrotron Radiation Facility [23]. On the principles of spatial fractionation, arrays of

a few dozens of micrometer-sized planar beams with about 50 - 400 µm center-to-center distance (*ctc*) are applied to the patients. Usually, highly brilliant synchrotron sources are used for beam generation. Therefore, the spatially fractionated pattern persists within the whole irradiation field and the generated valleys between the microbeams spare the traversed tissues [24, 25]. The beam characteristics in MRT, however, also prevent uniform irradiation of tumor volumes, which is a paradigm in conventional radiotherapy. A similar method using collimated carbon minibeams with sub-millimeter beam sizes was proposed by Dilmanian et al. [26, 27]. The limited range of the particles as well as its increased Relative Biological Effectiveness *RBE* [28] may have advantages over MRT. In both methods as suggested, the uniform irradiation of a tumor volume is only achieved by interlacing the pattern from several directions, which requires a very precise patient positioning due to the small beam dimensions. In 2013, Zlobinskaya et al. [29] and Prezado et al. [30] suggested to use spatially fractionated protons of sub-millimeter size, called proton minibeams. Due to the small-angle scattering in tissue, the beams increase in size with depth. By adjusting the *ctc* such that the beams overlap in the tumor volume ensures its uniform irradiation. Thus, reduced side effects due to the spatial fractionation in healthy tissues as well as a tumor control probability on the base of homogeneous tumor irradiation can be expected. The first experiments in animals show the immense sparing potential of proton minibeams [31, 32] but also the maintained high tumor control as in conventional radiotherapy [33–35].

In this work, proton Minibeam Radiotherapy (pMBRT) is further investigated in experiments using the ion microprobe SNAKE[(1)] and in theory by dose and cell survival calculations for idealistic tumors. After discussing the physical and biological background in chapter2, the experimental setup for the two main mouse experiments is presented (chapter 3). The first mouse experiment elaborates in detail different dose distributions and the corresponding sparing potential in chapter 4. The second mouse experiment combines proton minibeams with temporal fractionation and the effect of reirradiating proton minibeams in chapter 5. In chapter 6, the development of proton minibeams concerning interlacing and tumor homogeneity is proposed and discussed on the basis of dose calculations and the resulting cell survival. The last chapter summarizes the theoretical and experimental results and discusses possible future implementations in clinics as well as an outlook for future research.

[(1)] Superconducting Nanoprobe for Applied nuclear (German: Kern-) physics Experiments

Chapter 2

Radiation effects of energetic, charged particles

2.1 Interactions of energetic ions with matter

The most prominent member of energetic particles is the alpha particle, an energetic $^4_2$He ion. Energetic ions belong to the class of directly ionizing radiation, which is a term for any energetic particle that can remove orbital electrons from atoms or molecules [7]. The main component of interactions between incoming positively charged ions and the traversed matter is based on the Coulomb forces between the ion and the orbital electrons as well as the (partly shielded) atomic charge of the nuclei. Interactions of particles with nuclei are also possible, but occur only rarely and depend on energy, particle type, and traversed matter or in other words: the chance to overcome the Coulomb barrier. However, the secondary particles from nuclear reactions such as neutrons, protons, or other fragmented elements from the initial beam influence the distribution of ionizing events. With every ionization or excitation of an orbital electron, energy is deposited in the traversed matter. The physical quantification of the deposited mean energy ΔE in a mass Δm is called dose D and defined by

$$D = \frac{\Delta E}{\Delta m}. \tag{2.1}$$

The physical unit is Gray [Gy] where 1 Gy = 1 J/kg. The dose deposition of a particle within a target is based on statistical processes. For small volumes, it can include strong fluctuations in dependence of the actual considered volume size and is described in the field of micro-dosimetry [36, 37]. Additionally, the physical dose varies both in beam direction and perpendicular to the beam direction. Hereafter, the variation of the dose in beam direction, which is described by the depth dose

distribution, and the variation perpendicular to the beam direction described by the radial dose distribution will be discussed.

2.1.1 Energy loss, Linear Energy Transfer and depth dose distribution of ions

The energy loss of a charged particle traversing matter is well described by the so-called stopping power, although physically it is a stopping force. The stopping power S is defined as the quotient of $\mathrm{d}E$ and $\mathrm{d}l$, where $\mathrm{d}E$ is the mean energy lost by a charged particle in traversing the distance $\mathrm{d}l$, thus

$$S = \frac{\mathrm{d}E}{\mathrm{d}l}. \tag{2.2}$$

The physical unit is typically expressed as $\frac{\mathrm{keV}}{\mu\mathrm{m}}$. The stopping power adds the three components of electronic, radiative and nuclear stopping power by

$$S = \left(\frac{\mathrm{d}E}{\mathrm{d}l}\right)_{\mathrm{el}} + \left(\frac{\mathrm{d}E}{\mathrm{d}l}\right)_{\mathrm{rad}} + \left(\frac{\mathrm{d}E}{\mathrm{d}l}\right)_{\mathrm{nuc}}. \tag{2.3}$$

The electronic stopping power $\left(\frac{\mathrm{d}E}{\mathrm{d}l}\right)_{\mathrm{el}}$ is based on interactions with orbital electrons resulting in ionizations or excitations. The radiative stopping power $\left(\frac{\mathrm{d}E}{\mathrm{d}l}\right)_{\mathrm{rad}}$ originates from the emitted bremsstrahlung due to the appearing electric fields of atomic nuclei or electrons. The nuclear stopping power $\left(\frac{\mathrm{d}E}{\mathrm{d}l}\right)_{\mathrm{nuc}}$ describes the elastic collisions between projectile and the target nuclei. Nuclear collisions that produce new particles or change the internal structure of either the target nucleus or the projectile are considered as inelastic [38]. The stopping power does not cover the inelastic nuclear collisions which can also be considered as energy loss. In the energy ranges of radiotherapy ($< 250\,\mathrm{MeV}$ protons; $< 400\,\mathrm{MeV/nucleon}$ for heavier ions), the overall stopping power is strongly dominated by the electronic stopping power [39], which can be very well described by the Bethe equation [40] as

$$-\left(\frac{\mathrm{d}E}{\mathrm{d}l}\right)_{\mathrm{el}} = \left(\frac{e^2}{4\pi\epsilon_0}\right)\frac{4\pi n}{m_e}\frac{Z^2}{v^2}\ln\left(\frac{2m_e}{I}v^2\right) + \text{relativistic corrections}, \tag{2.4}$$

where Z is the charge of the projectile and v its velocity, n is the electron density of the target material, m_e is the electron mass, ϵ_0 is the electric field constant and I is the mean excitation potential of the target material.

Strongly related to the stopping power and more commonly used in radiobiology and medicine is the Linear Energy Transfer, LET. The LET is defined as the deposited energy, ΔE, per covered distance of the ion, Δl, in the surrounding material as

$$LET = \frac{\Delta E}{\Delta l}. \tag{2.5}$$

The physical unit is also $\frac{\mathrm{keV}}{\mu\mathrm{m}}$. The LET can be given as the restricted quantity LET_Δ, where all electrons with energy $> \Delta$ (delta rays) are excluded and therefore focuses on the vicinity of the primary particle track. The unrestricted Linear Energy Transfer LET_∞ is identical to the electronic stopping power $\left(\frac{\mathrm{d}E}{\mathrm{d}l}\right)_{\mathrm{el}}$.

For particle energies relevant in radiotherapy ($< 400\,\mathrm{MeV/nucleon}$), the LET is mainly proportional to $\sim Z^2 \left(\frac{\ln v^2}{v^2}\right)$ according to equation 2.4. The relativistic correction is below 2 % for kinetic energies of $\sim 400\,\mathrm{MeV/u}$ and only starts to contribute substantially for energies above $1\,\mathrm{GeV/u}$ ($\sim 7\,\%$). Eventually, the radiative energy loss will also contribute significantly for very high particle energies $\geq \mathrm{GeV}$ [38]. For small ion energies ($< 100\,\mathrm{keV}$ for protons and $< 1\,\mathrm{MeV/u}$ for carbon ions), where not all orbital electrons are stripped off the projectile, the shielding reduces the Coulomb interaction between projectile and target electrons, leading to a reduced LET. Several models are discussed by Sigmund [41]. The elastic nuclear stopping will also increase the LET for very low ion energies of few keV/u [36]. The range of these very slow particles is only in the µm range and therefore has little effect in radiotherapy.

The energy loss increases with decreasing energy and leads to maximum energy or dose deposition at the end of a charged particle's range. The statistical processes involved in the stopping of a particle lead to a scattering of the particle range around its mean. In water, the range straggling increases almost linearly with increasing depth or initial energy of the particle [42, 43]. The resulting depth-dose distribution from energy deposition of many particles is named the Bragg curve. The Bragg curve increases slowly with depth with a peak at the end of the range, the so-called Bragg peak (see Fig. 1.1). To irradiate the tumor uniformly in depth, several beam energies with weighted fluences are overlaid to form the Spread-Out Bragg Peak (hereafter: SOBP). In radiotherapy, the inherent advantage of the SOBP in comparison to X-ray therapy is used to reduce the overall dose in the healthy tissue. Especially the vanishing dose distally of the tumor is of great benefit and leads to reduced side effects [44, 45].

2.1.2 Lateral dose distribution

Considering a single particle, the lateral dose distribution is only dependent on the energy transfer to the secondary electrons. The maximum energy transfer occurs for a central elastic collision between projectile and electron and can be stated as $E_{\max} \approx 4E\frac{m_e}{m_p}$, where m_e is the electron mass, m_p is the projectile mass and E is the energy of the projectile. For carbon ions with energies of maximally $400\,\mathrm{MeV/u}$, an electron would maximally reach an energy of $\sim 0.2\,\mathrm{MeV}$, which refers to a maximum range of $0.45\,\mathrm{mm}$ in tissue [46]. The area, where these so-called delta electrons deposit their energy is called the penumbra, whereas the area around the ion track is called the core

($\ll 1$ µm in tissue) [47]. Due to the dose fall-off with $\frac{1}{r^2}$ from the initial ion track until the range maximum of the electrons [47, 48], the penumbra plays only a minor role in conventional radiotherapy.

A much higher impact on the overall lateral dose deposition of an ion needs to be accounted for the deflection of the ions themselves. The high masses of charged particles allow neglecting the deflection caused by the electron collisions. In contrast, a close pass by to an atomic nucleus will deflect the projectile due to the repulsive positive charge of the atom. While the impact of these kind of reactions at high particle energies ($\gg \frac{m}{2}v_0^2$, where v_0 is the Bohr velocity) is negligible on the stopping power [49], it might have a severe impact on the trajectory of the projectile. The elastic Coulomb scattering is usually classified in numbers of scattering events (N_S) within the considered volume of the target material. Single scattering events ($N_S = 1$) can be well described by Rutherford scattering. The differential cross-section $\mathrm{d}\sigma$ for the solid angle $\mathrm{d}\Omega$ is given as

$$\frac{\mathrm{d}\sigma}{\mathrm{d}\Omega} = \left(\frac{1}{4\pi\epsilon_0}\frac{Z_1 Z_2 e^2}{4E_0}\right)\frac{1}{sin^4\left(\frac{\vartheta}{2}\right)}, \tag{2.6}$$

where ϵ_0 is the electric field constant, $Z_1 e$, and $Z_2 e$ are the electric charges of the projectile and atomic nucleus, respectively, E_0 is the energy of the projectile and ϑ its scattering angle [50, 51]. A low number of scattering events ($1 < N_S < 20$) is called plural scattering and is difficult to describe analytically. For more scattering events ($N_S > 20$), stated as Multiple Coulomb Scattering (MCS), where statistical approaches are taking effect, is most comprehensively described by the theory of Molières [52] and its expansions of Scott [53] and Bethe [54, 55]. Although very detailed and in good agreement with experiments [56, 57], Molières theory is rather unwieldy for a simple representation of MCS effects. A parameterization of Molières theory is developed by Highland [58] and subsequently improved by Lynch and Dahl [55]. The Gaussian approximation for the beam width resulting from MCS (standard deviation σ) can accordingly be determined by

$$\sigma = 13.6\frac{\sqrt{X/X_0}}{p\beta}\left[1 + 0.088\log_{10}\left(X/X_0\right)\right], \tag{2.7}$$

where X is the thickness of the material, X_0 is the material-specific radiation length (0.02753/cm for water/biological equivalent [59]) and p the momentum of the particle. The presented approximation describes Molières theory as accurate as 11 % [55], but only for thin targets. An extension for thick targets is found in the work of Gottschalk et al. [57], resulting in a dependency of $\sigma \propto X^{3/2}$.

The core of an ion beam can be approximated very well with a Gaussian distribution

due to MCS. The non-Gaussian tales of the appearing distributions resulting from the single or plural scattering also need to be considered for therapeutic dose calculations. This tail of much lower amplitude (max. $\sim 20\,\%$ of the central Gaussian [60]) can again be approximated by a second, broader Gaussian distribution with sufficient accuracy for most practical demands in proton therapy [61]. Secondary particles from inelastic nuclear reactions can also disturb the lateral dose profiles (e.g. secondary protons) or deposit energy beyond any beam path or target (neutrons). In proton therapy, up to $15\,\%$ of the dose can be attributed to the beam halo resulting from large-angle scattered protons and secondary particles from nuclear reactions [61].

2.2 Radiation effects on living cells and tissues

The physical properties of cells and tissues can be approximated by its main component water ($> 70\,\%$ of total cell mass). Therefore, all ionization events and their distribution caused by highly energetic particles is well described and can be calculated. Living material, however, is extremely complex with many mechanisms on nano/micrometer, millimeter, or even centimeter scales. In radiotherapy, the well-being of the patient is of highest priority and usually assessed in very macroscopic measures like organ functions, tumor shrinkage, and overall tissue reactions to the applied radiation dose. The smallest independently living component of mammalian tissues is the cell. To understand the effects of radiation on tissues it is essential to also recognize the impact of radiation on its smallest component. The next sections are supposed to give an overview of radiation effects on single cells and its consequences on healthy and cancerous tissues. Afterwards, a discussion of how these mechanisms are used in conventional radiotherapy as well as in academic research for future radiotherapy approaches is presented.

2.2.1 Cell effects

The most radiation sensitive part of a cell is the DNA[(1)] molecule. The DNA only appears once or, dependent on the cell cycle, maximally twice in the cell nucleus and carries the genetic information, making it a particularly vulnerable component of the cell. The DNA consists of two polynucleotide chains that form a double-helix structure. A single component of the polynucleotide chain is called a nucleotide, which is again composed of one out of four nucleobases (adenine, cytosine, guanine, or thymine), the sugar part deoxyribose, and a phosphate group. The two polynucleotide chains are connected via hydrogen bonds between the complementary nucleotides adenine/thymine

[(1)] deoxyribonucleic acid

and cytosine/guanine. In total, the sequence encoding the genetic information of humans contains 3×10^9 base pairs [62].

Damage to the molecule can either happen directly by traversal of an ion or indirectly by radiation-induced radicals. DNA damage is categorized into two types, single-strand breaks (SSB) and double-strand breaks (DSB). Only one of the two polynucleotide chains is harmed in the SSB. Due to the intact complementary side, internal DNA repair mechanisms are highly reliable. If more ionizations occur close to each other (< 10 base pairs), the DNA molecule can rip apart and a DSB is induced. Although there are also biological repair mechanisms, the lack of redundancy causes a much higher error probability in the repair of a DSB. One Gray of low-LET radiation induces around 10^3 SSBs and 35 DSBs [63]. For high doses, an additional quadratic increase in DSB can be observed due to the statistical chance that two SSBs form one DSB [64]. While SSBs are only of minor danger to the cell, the vulnerability of the DSB repair can have serious consequences. Programmed cell death (apoptosis), cell cycle arrest or mitotic catastrophe followed by necrosis can be induced by incorrect or incomplete repair. Stable repair errors cause mutations or chromosomal aberrations with possible malfunctions of the whole cell, or even the induction of carcinogenesis [65].

The amount of DNA-damages increases with LET due to the higher ionization density [66]. High LET particles such as heavy ions are therefore biologically more effective, which is described by the Relative Biological Effectiveness *RBE*. The *RBE* puts the dose of the used radiation type in relation to the dose of the reference radiation that causes the same level of biological effect. The γ-rays of the ^{60}Co decay are usually used as the reference radiation.

In summary, the response of a cell to radiation is a complex system and detailed predictions depend on many factors. A simplification of this complexity is given by the consideration of the entire cell survival, as often used in radiobiology. Cell survival is usually defined as the proliferative potential of a cell stock and can be quantified by the colony formation assay [67]. Repeating the colony forming assay for different irradiation doses results in a dose-response or cell survival curve. The shape of the cell survival curve depends on the sort of radiation and the cell line. The differing shape due to sort of radiation, especially high LET radiation, and the inherent occurring curve differences are expressed as the *RBE* as mentioned above. The reference curve for any cell line is usually elaborated for γ-rays (mostly ^{60}Co). A schematic cell survival curve is exemplarily presented in Fig. 2.1. The cell survival follows a linear-quadratic behavior in the semi-logarithmic presentation. One model that describes the cell survival is

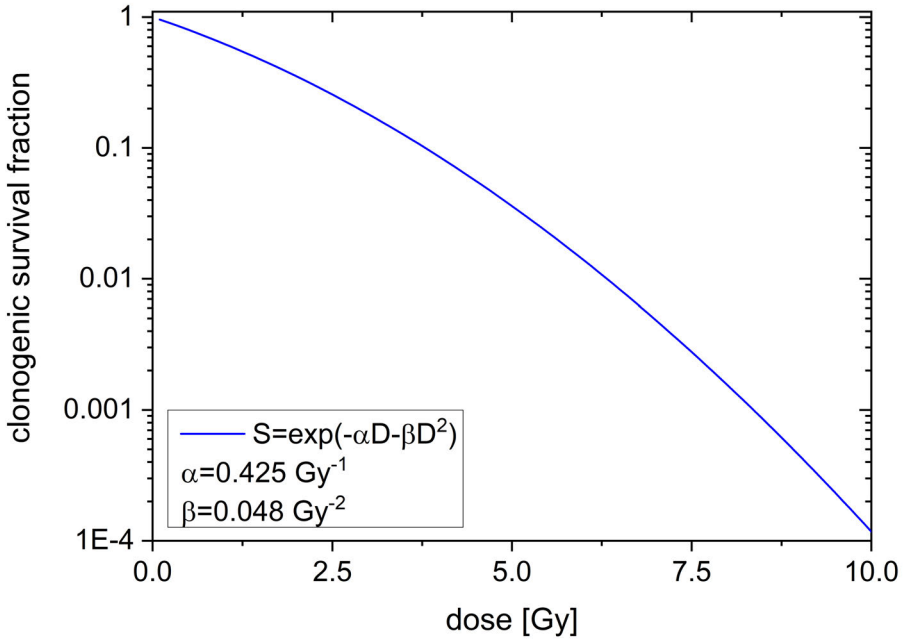

Figure 2.1: *Calculated clonogenic cell survival over radiation dose by the linear-quadratic model. The α and β values are mean values of all human cells listed in the PIDE database [68].*

therefore called the Linear-Quadratic model (LQ-model). It is defined as

$$S = S_0 \times \exp\left(-\alpha D - \beta D^2\right), \tag{2.8}$$

where S is the number of proliferating cells, S_0 is the number of irradiated cells, D [Gy] is the dose and α [Gy^{-1}], β [Gy^{-2}] are cell-specific parameters. α and β are determined empirically and vary with cell line. The mechanistic interpretation of α and β is an ongoing discussion that already started decades ago. The most common interpretation states that the α term serves as a description of directly induced DSB, which increases linearly with dose. The β term is the quadratic increase of DSB based on accumulated SSB (< 10 base pairs) [69]. The simplicity of the mechanistic description and the model itself is very appealing, but excludes many other biological factors that may influence the cell survival as nicely discussed in the review of McMahon [70]. This originates, that e.g. the LQ-model becomes less accurate with high doses above ~ 13 Gy [71–73], due to the overestimation of the β term. For higher doses, a linear continuation of the LQ-model is suggested by the local effect model III (LEMIII) [74]. The biological verification of its accuracy is, however, hardly realizable due to the limits of the colony formation assays. The cell survival curve for protons follows the same behavior as

for X-rays with the difference of a constant *RBE* of 1.1, as commonly assumed in radiotherapy [75].

2.2.2 Tissue effects

The effects of radiation on cells have been discussed in section 2.2.1. Tissues are a complex structural organisation of differentiated cells each with their own specific purpose or function. The function of tissue after irradiation is dependent on its organization, the irradiated dose which can be translated into surviving cells, and the irradiated volume. These parameters are combined within the concept of functional subunits (FSUs). A functional subunit is defined as the maximal tissue volume that can recover from only one surviving clonogenic cell [16, 76]. In other words, the FSU gives the clonogenic cell surviving density that is necessary to fully recover the tissue. The importance of a single FSU to the overall tissue is dependent on its organization. There are either parallel (e.g. skin, liver) or serially (e.g. spinal cord, intestine) organized tissues. In parallel tissues, FSUs work independently of each other and only a minimum amount of FSUs are necessary to keep a parallel tissue intact [76]. In serial tissues, a single malfunction of an FSU can be critical for the entire tissue. The distribution of the dose might therefore be adapted and optimized by the tissue sort. However, no organ or tissue is purely parallel or serial but rather tends towards serial or parallel organization [76]. The description of tissues by FSUs is only meaningful for healthy tissues, since tumors have no vital function or structural benefit.

2.2.3 Tumor treatment with radiation

The primary goal in tumor treatment is the reduction of growth and ideally, even its complete stop. Hence, all clonogenic cells of a tumor need to be damaged such that they, at least, stop proliferation [76]. In radiotherapy, ionizing radiation is used to induce severe damages to the cancerous cells. The uniform irradiation with a sufficient amount of dose to the tumor volume is necessary to inactivate every cell. Only a small amount of surviving cells can lead to the recurrence of the tumor [77]. Typical integral doses applied to the tumor are between 40 - 70 Gy, but depend on tumor type, sort of radiation used, and also the application schedule. In general, the probability to control a tumor increases with dose and is expressed as Tumor Control Probability (TCP; see Fig. 2.2). However, with more dose, the chance of adverse side effects also increases, which is defined as the Normal Tissue Complication Probability (NTCP). The progression of the NTCP is similar to the TCP and increases with dose. For the well-being of

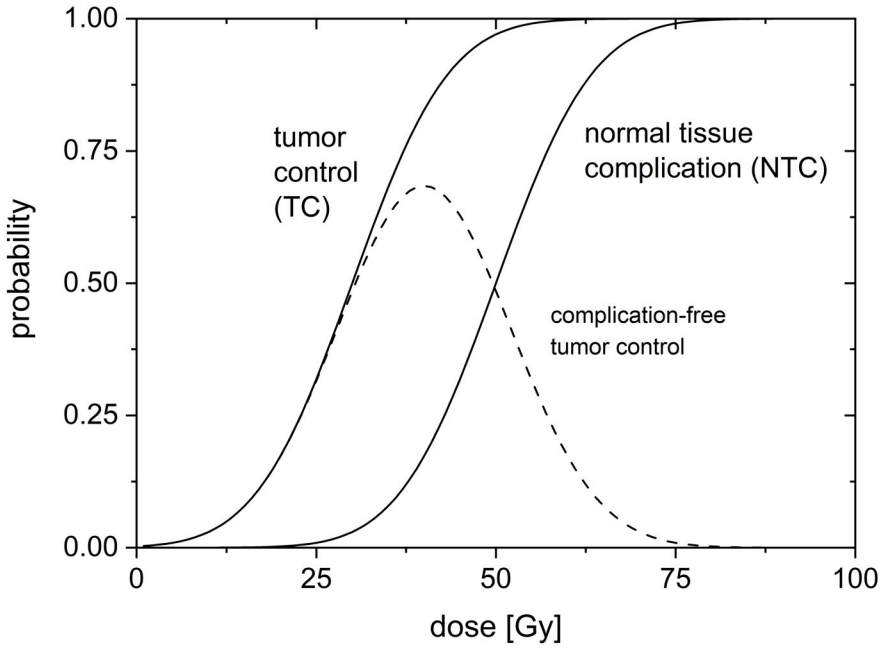

Figure 2.2: *Tumor Control Probability (TCP) and Normal Tissue Complication Probability (NTCP) over dose. The curve of complication-free tumor control (dashed line) determines the compromise between acceptable side effects with maximum tumor control.*

the patient, it should be kept as small as possible. The compromise between acceptable TCP and NTCP is the so-called therapeutic window [7, 76]. The optimized treatment setup lies in the maximum of the complication-free tumor control curve (dotted line in Fig. 2.2).

The side effects of an untreated fast growing malignant tumor are very diverse and depend mainly on the sort of tumor and its location. Eventually, an uncoordinated growth of tissue adversely affects the patient and if it interferes with vital functions, it leads to death. Although the treatment with radiation may control the tumor, it can lead to severe side effects for the patient. Side effects depend on the irradiated tissue and its radio-sensitivity [7]. They are categorized in acute (< 90 days) and late side effects (> 90 days). Acute side effects are often observed in the skin of the irradiated fields with damage as severe as moist desquamation. Other acute side effects are nausea and vomiting, sore mucosa, especially in mouth, throat and stomach, intestinal discomfort, or any other inflammatory response to radiation [78–82]. Although very uncomfortable, acute side effects are usually fastly recovering processes and already heal a few weeks after treatment. Late side effects are of even greater importance than

acute side effects since they can last for months, years, or even decades and might be severely detrimental to the quality of life after treatment. Typical late side effects are dryness of mouth or eyes, lymphedema, cardiovascular diseases, epilation, gastrointestinal toxicity, or fibrosis [83–88]. Tissues that have been exposed to radiation are also more prone to developing secondary cancers [89, 90].

Decreasing the side effects of radiation treatment widens the therapeutic window and radiotherapy can substantially be improved. The standard method to keep side effects within an acceptable range is temporal fractionation. The radiation response is reduced if the total dose is applied in multiple fractions over time. Standard fractionated irradiations are scheduled on five days a week with $\sim 2\,\mathrm{Gy}$ per fraction over several weeks [7, 76]. The underlying mechanisms behind fractionation are called the 5 Rs of fractionated radiotherapy. Healthy tissues benefit from cell Repair and Repopulation between the fractions, which are less efficient for tumor tissues. Additionally, the Radio-sensitivity of tumors can increase due to the Redistribution of the cell cycle phases as well as the possible change of the oxygenation status of the tumor due to Reoxygenation [7, 76]. The treatment parameters of fractionated radiotherapy have been established over decades of oncology experience. Nevertheless, modern radiation therapies (e.g. ion beam therapy, intensity-modulated therapies, etc.) that are more gentle to patients, as well as new radiobiological findings of tissue responses, open the possibility to adapt treatment parameters. It is under current investigation if hypofractionation, the reduction of dose fractions, reduces the treatment effort and costs without adverse side effects. It is also possible that higher doses per fraction are advantageous for tumor control [91], but is discussed controversially [92]. However, it is not possible to generalize such a statement at the moment, since studies differ in treatment modalities, applied doses, amount of fractions, and time between fractions [93].

2.2.4 Spatial fractionation

The basic idea of spatial fractionation is the geometrical sparing of healthy tissue. The treatment dose is applied in a pattern where small parts of the irradiated volume receive very high (up to several hundred Gy) doses but large parts of the irradiated volume are spared, receiving only very low to no doses. The geometrical sparing achieves higher tissue tolerances based on the principles of the dose-volume effect [16, 17]. The dose-volume effect describes the general volume dependency of the applied dose to induce a certain effect [16] and might be attributed to migration and repopulation of irradiated areas by healthy cells from the close surrounding [94]. Further effects like the fast repair of capillary blood vessels [20] and strong capillar resistance [21] to radiation dose may also add to the higher tissue tolerance.

Despite the early attempts of Köhler and Liberson [9, 95], spatial fractionation has mostly gained attention in the last two decades. At date, the two main techniques in spatial fractionation with sub-millimeter beams are the X-ray Microchannel Radiation Therapy (MRT) [22, 23] and the ion minibeam therapy, suggested by Dilmanian et al. [27] and extended for protons by Zlobinskaya et al. [29] and Prezado et al. [30]. MRT uses planar beam shapes with beam sizes of few tens of micrometer and up to several hundreds of micrometer center-to-center (hereafter: *ctc*) distances. The dimensions within the minibeam therapy with ions are usually in the sub-millimeter range and *ctc* distances of few millimeters.

The main differences between MRT and ion minibeams appear within the propagation through tissue. The inherent physical advantages of ion beams due to the Bragg Peak remain also for spatial fractionation. No dose is deposited behind the tumor in ion minibeam therapy. In MRT, the exponential decrease of the dose also significantly affects tissues distally of the tumor. Moreover, the planar shape of X-ray microbeams remains unchanged with depth. Hence, the dose modulation is strong within the tumor in MRT, which affects the mechanisms of tumor control. Not every tumor cell receives a lethal dose, which has always been the paradigm of radiotherapy. However, tumor growth delay or even tumor control can be induced [96], but needs further clarifications.

In the case of ion minibeams, the beam size σ increases with depth due to small-angle scattering. It is described by the initial beam size σ_0 and the small-angle scattering $\sigma_{sc}(d, E)$, which depends on depth, energy, and sort of the incoming particle, as $\sigma = \sqrt{\sigma_0^2 + \sigma_{sc}(d, E)^2}$ for a first-order approximation of a Gaussian dose profile. The energies, which determine the range of the particles, are adjusted to the location and size of the tumor to fully irradiate the tumor volume. Therefore, location and tumor thickness predetermine the appearing beam sizes. The second parameter required to fully describe the dose distribution is the *ctc* distance between the minibeams. The dose modulation at any depth in the entrance channel is given by the ratio between beam size (σ) and center-to-center distance (*ctc*) σ/ctc. The dose modulation within the tumor can be adjusted by varying the *ctc* distances. Even conventional, homogeneous irradiation of the tumor after the ICRU limits [97, 98] is possible when a σ/ctc ratio of > 0.5 within every location of the tumor is fulfilled. Spatial fractionation with ions is in principle independent of the ion sort, if *ctc* distances are adjusted to the beam sizes. The combination of spatial fractionation in healthy tissues with a homogeneous irradiation of the tumor volume is, however, technically easier for proton minibeams. The weaker scattering of heavier particles requires smaller *ctc* distances to cover a tumor homogeneously, which in turn needs smaller, technically more sophisticated, initial beam sizes for a spatial fractionation effect. Furthermore, the acceleration of protons

up to radiotherapy-relevant energies ($\sim 250\,\mathrm{MeV}$) is also less demanding and cheaper than for heavier ions like He or C, making protons the most common ion therapy approach. Hence, studies concerning ion minibeams have focused much more on protons than on heavy ions, especially from an experimental point of view.

The first proof of principle experiment for the reduced side effects in healthy tissue irradiated mouse ears with 20 MeV proton [31]. The healthy ears of BALB/c mice were irradiated with either a $7.2\,\mathrm{mm} \times 7.2\,\mathrm{mm}$ homogeneous field or 4×4 minibeams of squared $180\ \mu\mathrm{m} \times 180\ \mu\mathrm{m}$ with 1.8 mm *ctc* distance. The average dose was 60 Gy in both groups, raising the peak dose within the squared minibeams up to 6000 Gy. During the whole monitoring time of 90 days, there were no radiation responses visible in the minibeam irradiated group whereas strong skin reactions were observed in the homogeneously irradiated group. Similar distinct results were found by the same research group in a human skin model checking for tissue viability, cytokine expression, and even genetic damage expressed by micronuclei [31].

A french group investigated the proton Minibeam Radiotherapy (pMBRT) effects on rat brains [32]. In healthy brains, a 25 Gy mean dose was applied homogeneously with a beam size of $1.6\,\mathrm{cm} \times 2\,\mathrm{cm}$ using 100 MeV protons. The same mean dose and particle energy were used for the minibeam group with a minibeam width reported to 1.1 mm in 1 cm tissue depth and a *ctc* distance of 3.2 mm. The minibeam group showed only minor brain damage and no visible skin effects. Severe skin toxicities and significant brain damages were found in the homogeneously irradiated group [32]. The first tumor irradiation with minibeams in rat brain gliomas showed a superior outcome for proton minibeams than for conventional irradiation. 67 % of the rats treated with minibeams survived over the 170 days observation time in comparison to only 22 % of the conventionally treated rats. It needs to be mentioned that the dose distribution within the tumor volume in this experimental setup was not fully homogeneous but had a Peak-to-Valley Dose Ratio *PVDR* of 1.2 [34]. A follow-up study investigating into different dose modulations within the tumor volume did not show any adverse effects of proton minibeams for tumor control [35].

In a theoretical study, proton minibeam dose distributions of different patterns were calculated for a uniform irradiation of a tumor located in 10 - 15 cm depth. For the first time, dose distributions could be analyzed in any depth and the calculated mean clonogenic cell survival served as the biological weight to compare minibeam patterns with the corresponding conventional proton irradiation. The tumor dose in the study was kept homogeneous according to the ICRU report [97, 98]. Exemplary dose distributions and cell survival results for proton minibeams as well as broadbeam irradiation are presented in Fig. 2.3, adapted from [99].

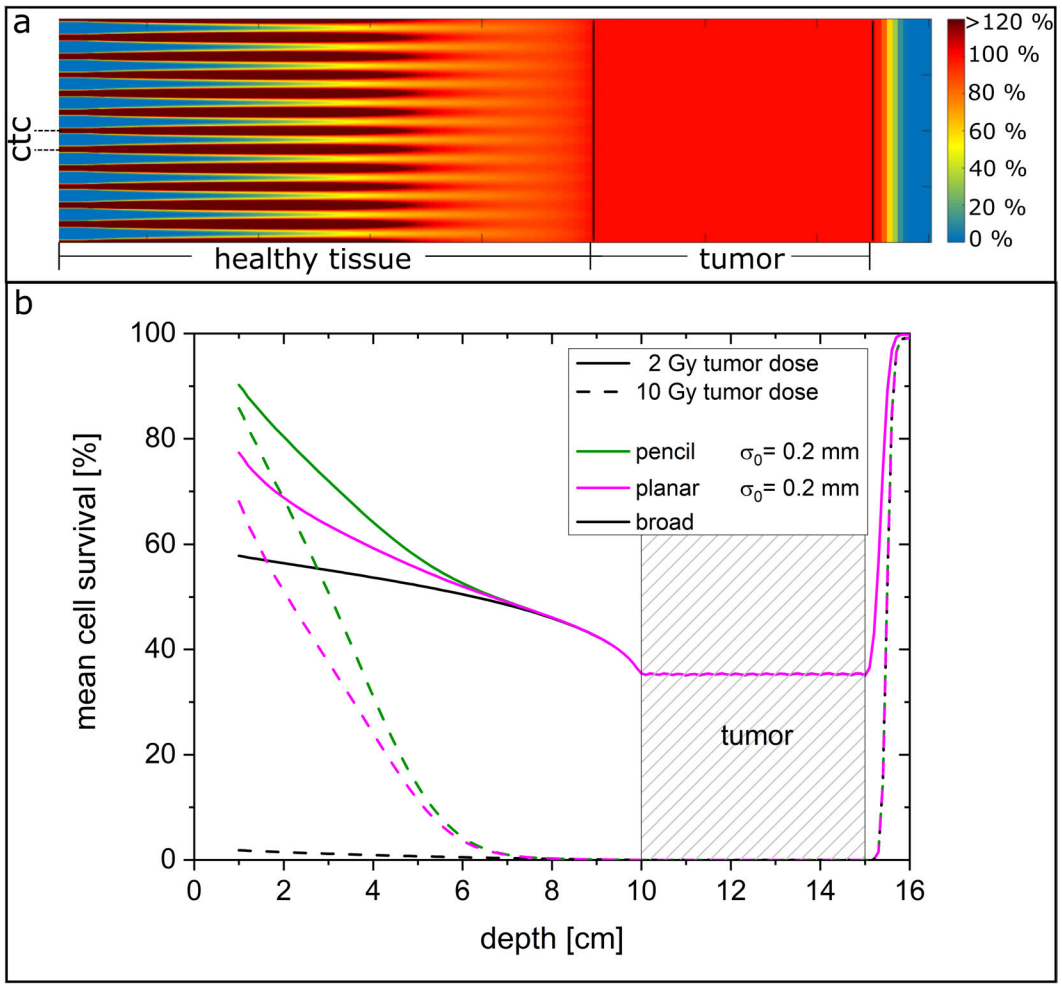

Figure 2.3: *Schematic dose distribution for pMBRT (a) and calculated mean clonogenic cell survival for a unilateral proton minibeam irradiation for 2 and 10 Gy homogeneous tumor dose (b). The minibeams were either arranged on a quadratic pattern for pencil minibeams or planarly for planar minibeams. The curves were adapted from Sammer et al. [99]*

.

The main sparing is achieved in the first centimeters and decreases with depth due to the small-angle scattering of the minibeams. Hence, most sparing is found for the smallest σ/ctc ratio at the superficial layers. After around 7 cm of depth, no significantly enhanced cell survival can be obtained by proton minibeams compared to conventional broadbeam irradiation. Due to the geometrical sparing in spatial fractionation, the findings are almost independent of the dose in the superficial layers.

Chapter 3

Proton minibeam irradiation at SNAKE in an in-vivo mouse ear model

The ion microprobe SNAKE (**S**uperconducting **N**anoscope for **A**pplied nuclear physics (german: **K**ernphysikalische) **E**xperiments) is installed at the Munich 14 MV Van-de-Graaff tandem accelerator. It is capable of focussing any sort of ion beam with a mass-energy product of 200 MeV·A/q^2 to sub-micrometer sizes [100]. SNAKE is used in material analytics, especially for the 3D detection of hydrogen using the special characteristics of proton-proton scattering in combination with the sub-micrometer lateral beam resolution [101]. Besides the development of the microprobe itself [100, 102, 103], it was extended for biological experiments within two PhD theses [104, 105]. The microbeam allows for extraordinary radiobiological experiments due to its capability to target sub-cellular structures in single cells [106–108]. The additional adaptation for the irradiation of small animals [36, 109] turns SNAKE into the ideal instrument to carry out proton minibeam experiments within this work.

The following sections serve both as a summary of beam preparation for proton minibeams and as an overview of SNAKE. More detailed information is available in the cited original literature.

3.1 Minibeam preparation

A schematic overview of the microbeam preparation is presented in Fig. 3.1. Dependent on ion sort, several ion sources are available at the Munich tandem accelerator. The negatively charged ions (-1e) are inserted into the tandem accelerator after pre-acceleration with a voltage between 100 - 180 kV [110] and attracted by the terminal voltage of several MV (max. 14 MV). Within the terminal, electrons of the negatively

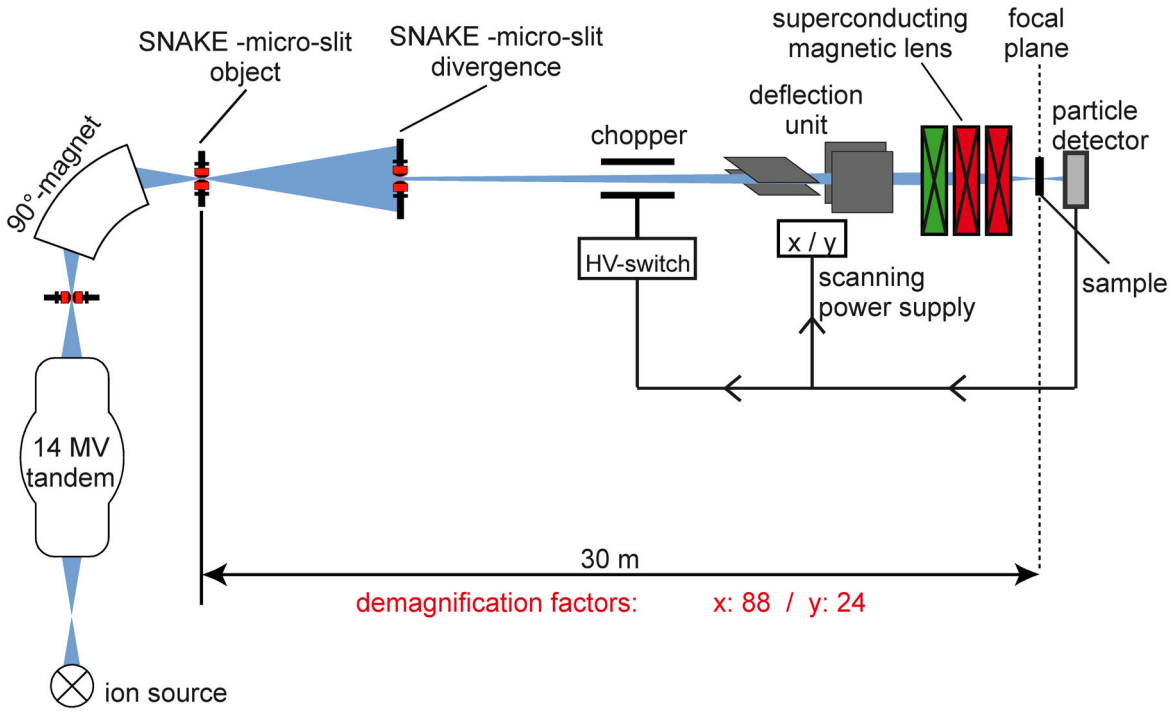

Figure 3.1: *Schematic illustration of the beam line for a microbeam at SNAKE. The slit system defines the object that is focused by the superconducting lenses to a spot of* $< 1\,\mu m$ *in the focal plane. Adapted from [109]*

.

charged ions are stripped using a thin carbon foil [111]. The resulting positive ions traverse the terminal, which repels the ion due to the high positive terminal voltage. The resulting ion energy E behind the tandem is dependent on the two voltages of the pre-acceleration U_{PA} and terminal voltage U_T, as well as the ion charge q behind the stripper foil. It can be stated as $E = eU_{PA} + e(q+1)U_T$, where e is the elementary charge. The Munich tandem accelerator is designed for a 14 MV voltage at the terminal and can be stably operated with around 11 MV. Maximum energy of 28 MeV is possible for protons of which 21 MeV were used within this work.

After the accelerator, the beam is deflected by the 90° analyzing magnet. For heavy ions, the analyzing magnet is used to select for $\frac{mv}{q}$, where m is the mass, v the velocity and q the ion charge. Due to the pre-selection by ion mass before the tandem, the selection of the analyzing magnet corresponds to an energy selection. For protons, only the $+1e$ state can undergo the full acceleration of the tandem. To form the ion-optical object, micro-slits are used to cut out around 20 µm × 10 µm. This object is demagnified by a superconducting multipole triplet with a factor of 1/100 in x-direction and 1/25 in y-direction [100] enabling a focal spot of less than 1 µm. The divergence of the

beam is limited by the second pair of micro-slits, limiting the divergence to ±10 µrad. Behind the multi-pole lenses, the beam exits the vacuum through the beam exit nozzle covered by a 7.5 µm capton foil, and the samples can be irradiated in the focal plane [105, 112].

To create a minibeam of several tens to hundreds of µm, the microbeam has to be enlarged. Therefore, a 200 µm thick aluminum plate is attached to the beam exit nozzle. The aluminum reduces 21 MeV protons by around 1 MeV, resulting in the desired irradiation energy of 20 MeV for all experiments conducted within the course of this thesis. The metal layer also scatters the proton beam to larger, mainly Gaussian distributed angles and by simply adjusting the distance d of the sample to the aluminum, any desired minibeam size (< 900 µm Gaussian σ) can be generated (cf. Fig. 3.2) [109, 113].

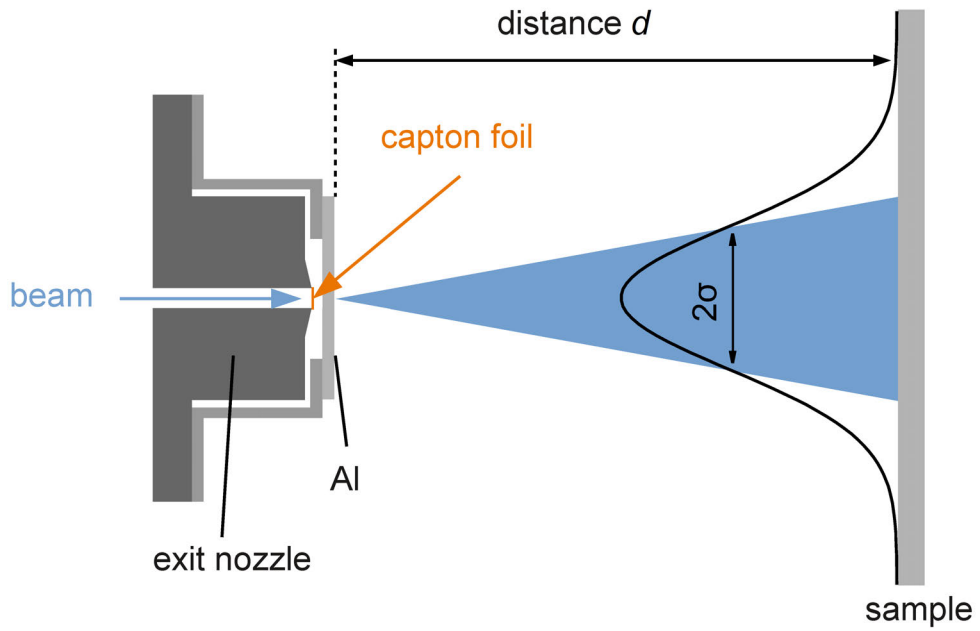

Figure 3.2: *Scatter of a microbeam to generate a Gaussian-shaped minibeam. A 200 µm aluminum platelet is mounted directly behind the exit nozzle with capton foil. The beam size can be adjusted by adapting the sample distance d. Adapted from [109]*

.

3.2 Mouse irradiation setup

The adaptation for biological samples and eventually small animal irradiations has been carried out in years of development within four PhD theses [36, 104, 105, 109].

Focusing the ions on the focal plane right behind the beam exit foil enables the irradiation of biological samples under atmospheric pressure. An inverse microscope (Axiovert 200M, Carl Zeiss AG, Oberkochen) is installed on a slide with a step motor (1.56 µm per step) in beam direction (z-axis). The sample is fixed on the xy-stage of the microscope for highly precise positioning. The focal planes of SNAKE and the microscope can be matched, allowing for microscopic monitoring before, during, and after irradiation [36]. In the case of the macroscopic sample of a small animal, only the positioning system of the microscope is used. The slide in z-direction allows to adjust the distance of the sample from the aluminum platelet and, therefore, set the minibeam size due to the lateral straggling of the beam. The xy-stage of the microscope is used to generate the minibeam pattern of 4×4 minibeams with a center-to-center distance of 1.8 mm.

A specially designed mouse holder [109] was mounted to the xy-stage for mouse irradiations (cf. Fig. 3.4b). To ensure the well-being of the animals during treatment, the holder and the beam nozzle were heated at a controlled temperature of 37°C. Behind the mouse holder, a BC-418 plastic scintillator in combination with a photomultiplier tube (PMT; Hamamatsu R7400P) was mounted in the objective revolver of the microscope for ion detection. The single-ion preparation of [104] and its extension [36] was used to count every ion, enabling a highly accurate dosage. The counting of the ions was realized by a hardware-counter (N1145, Caen, Italy), which also triggered a high voltage chopper that deflects the beam after the application of all ions. The counting electronics are reliable up to some MHz count rate [36]. Since the time of irradiation was limited to a maximum of 30 minutes due to anesthesia of max. 45 minutes, count rates of up to 5 MHz were necessary. The resulting dead times of detector and detection electronics were calibrated for different count rates using radiochromic EBT3 films (GafChromic™, Ashland, US). The results are presented in Fig. 3.3. A 500 µm × 500 µm field was prepared using the electrostatic scanning unit of SNAKE [36] and irradiated homogeneously on a radiochromic film with 1,180,000 protons (mean dose of ~ 2 Gy) with different count rates. The electronic count rate was determined by the time it took to count the particles and compared to the count rate determined over the actual dose irradiated, measured via radiochromic evaluation. The particle loss due to PMT dead times was calculated as the ratio between the dose determined count rate and the electronic count rate. A particle loss of 25 % was measured for a 4 MHz electronic count rate resulting in a real application count rate of 5 MHz. This was subsequently compensated by adjusting the number of counted ions.

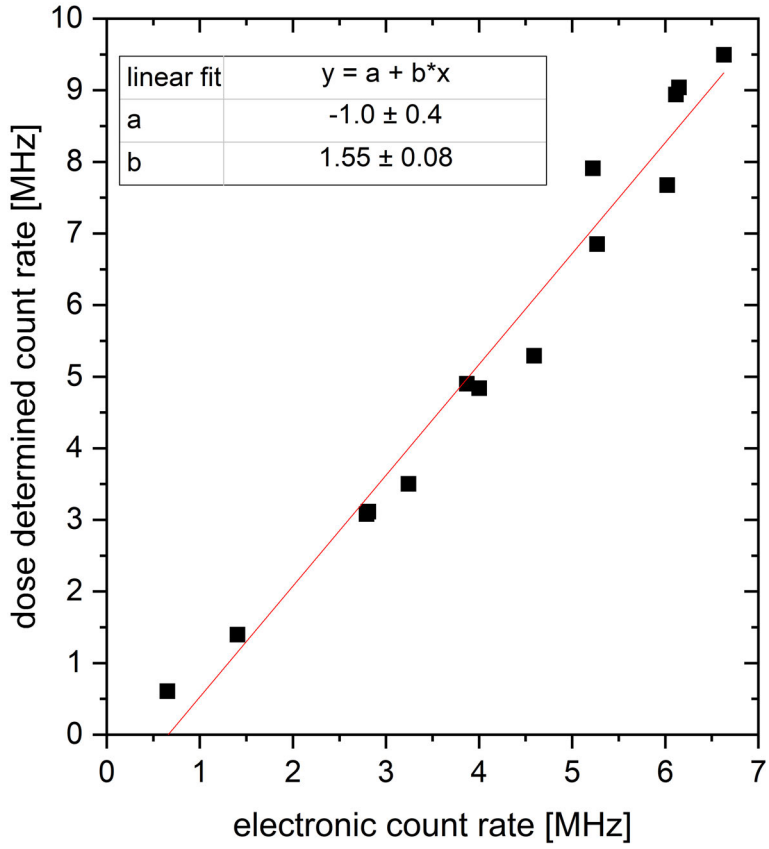

Figure 3.3: *Dose-determined count rate over electronical count rate. The linear fit is a first-order approximation and is only valid for electronic count rates below ∼ 7 MHz. The deviations between both count rates are based on the electronic dead times of the particle detector.*

3.3 Mouse ear and beam positioning for fractionated irradiation

Most of the content in this section is reprinted with permission (author reprint) from: Sammer, M. and Dombrowksy, A. *et al.* Normal tissue response of combined temporal and spatial fractionation in proton Minibeam Radiotherapy.
International Journal of Radiation Oncology Biology* Physics* **109** (2021) 76-83.

The conduction of a minibeam experiment with consecutive daily fractions in mouse ears required a positioning system that allowed for high irradiation accuracies of ∼ 100 µm. Therefore, a customized positioning system including image guidance was developed (Fig. 3.4) to correct for morphological, rotatory, and translatory errors.

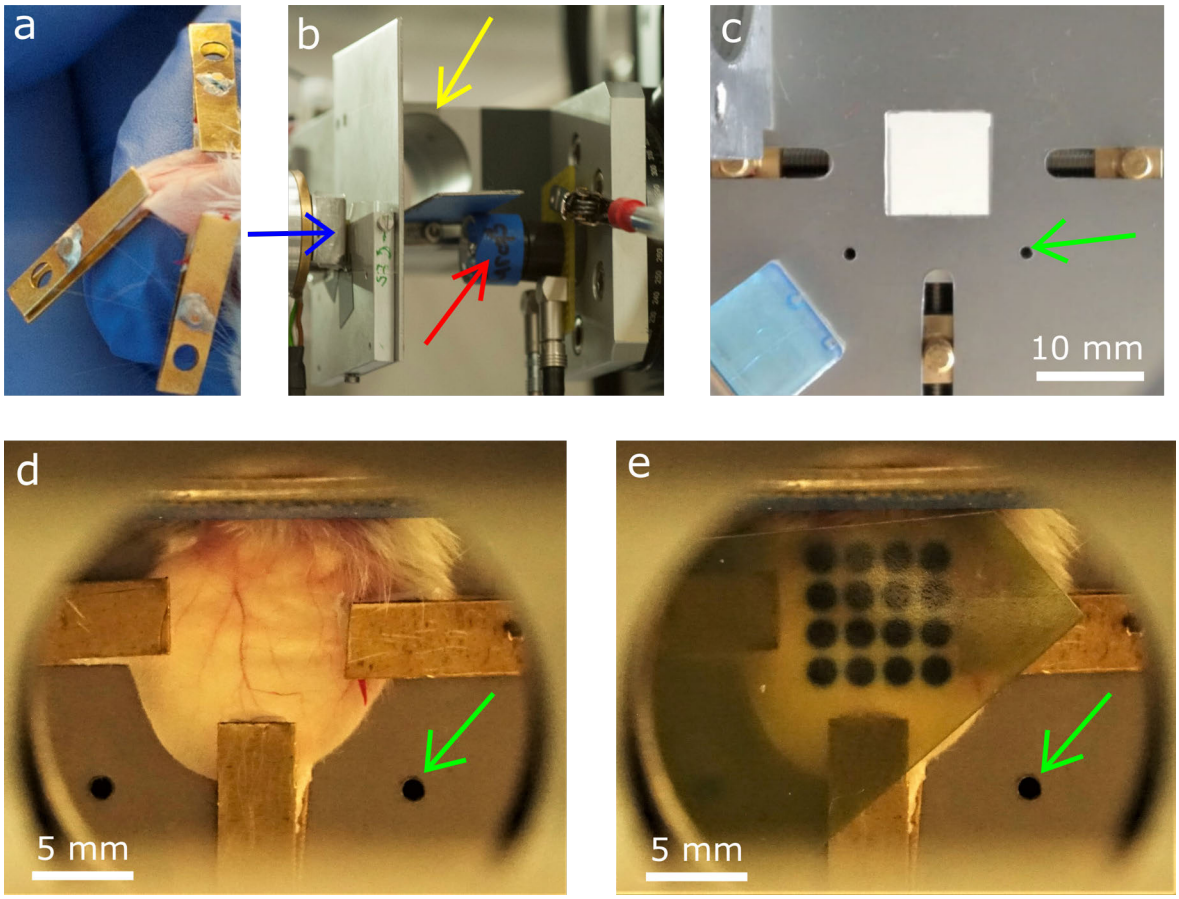

Figure 3.4: *a) Mouse ear with three attached clamps. b) The installed mouse holder at SNAKE. The colored arrows present the beam nozzle and beam direction (blue), the aluminum holder for mouse insert (yellow), and the particle detector (red). c) Pin mechanism of the holder. All pins can be adjusted by a screw in both directions. The pins serve to fix the ear clamps. The green arrow marks the absolute zero of the positioning mechanism. The white square is the hole to let the beam pass through. The clamp to hold the radiochromic film can be seen in the lower right corner (transparent blue). d) Picture of the mouse ear without radiochromic film. The green arrow marks the absolute zero of the positioning mechanism. e) Picture of the mouse ear with radiochromic film.*

After anesthesia, three clamps were removably attached to the mouse ear using skin compatible tape in such a way as to not damage the ears (Fig. 3.4a) and the prepared mouse was placed in a cylindric mouse holder insert. The mouse was placed into an aluminum, temperature-controlled holder fixed on a rotational stage (High-Precision Rotation Stage PR01(/M), Thorlabs Inc., US; vernier scale resolution: 5'), which was subsequently screwed on the xy-stage of the microscope at SNAKE ($\sim$1 µm absolute

position accuracy) (Fig. 3.4b). A pin system was mounted at the ear location to attach the ear clamps for a careful ear stretching (Fig. 3.4c) and neat irradiation without folds. A camera (SonyRX10 III) was installed over the microscope for visualizing the irradiation field with a resolution of 12.6 µm/px. A mirror was mounted on the turret to direct the light path towards the ear. Pictures were taken before and after irradiation with and without radiochromic film (Fig. 3.4d - e) for retrospective positioning analysis. The pictures of day one served as a template for the following fractions. During the positioning process at day 2 - 4, a picture was taken after rough ear fixation. A self-written Matlab [114] script analyzed the translatory and rotatory position of the individual vessel structure via cross-correlation. The potential irradiation field on the mouse ear picture was cropped regarding the absolute zero (mechanical hole in the holder) to only match for the vessel structure. After correction for rotation and translation by the corresponding stages, morphological errors could be degraded using the pin system. When touching the pins, the positioning process with the holder at absolute zero was repeated to iteratively optimize the ear position. After fixation and positioning of the ear, a radiochromic film was placed behind the ear for ensuring correct irradiation as well as localizing the irradiation field. A work flow chart for the ear positioning procedure is shown in Fig. 3.5.

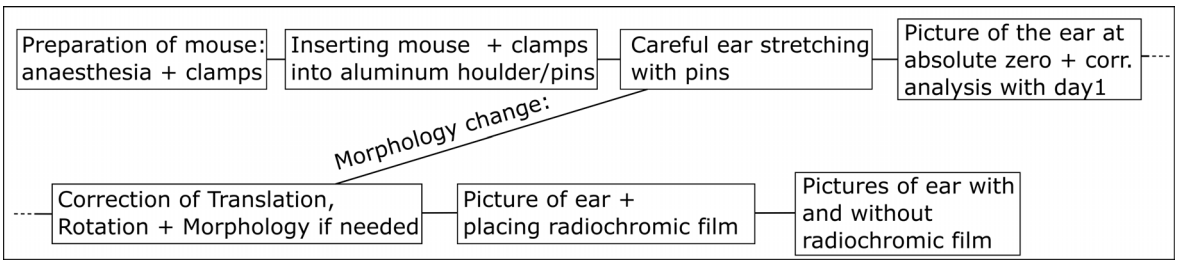

Figure 3.5: *Workflow chart for ear positioning.*

Additionally, the beam position was checked and corrected after every third mouse using a similar workflow due to mostly thermical effects on the superconducting lens. A radiochromic film was irradiated on day 1 serving as a template. Variations on the beam position for the following days was determined via cross-correlation. Since the beam is radially symmetrical, only translative beam movements were corrected by the microscope stage.

The overall reirradiation accuracy combining ear positioning and beam correction was determined by cross-correlating the ear locations of the radiochromic-determined irradiation fields of day 2 - 4 with the template of day 1. To include the unavoidable morphological errors, the analyzed irradiated field was divided into four quadrants,

which were independently analyzed with the corresponding quadrants of day 1. The scatter around the centroid of the four fractions per quadrant is determined via cross-correlation. The mean value of the reirradiation accuracy for all mice, fractions and quadrants analyzed was (110 ± 52) µm. A graphical example is depicted in Fig. 3.6 for better visualization.

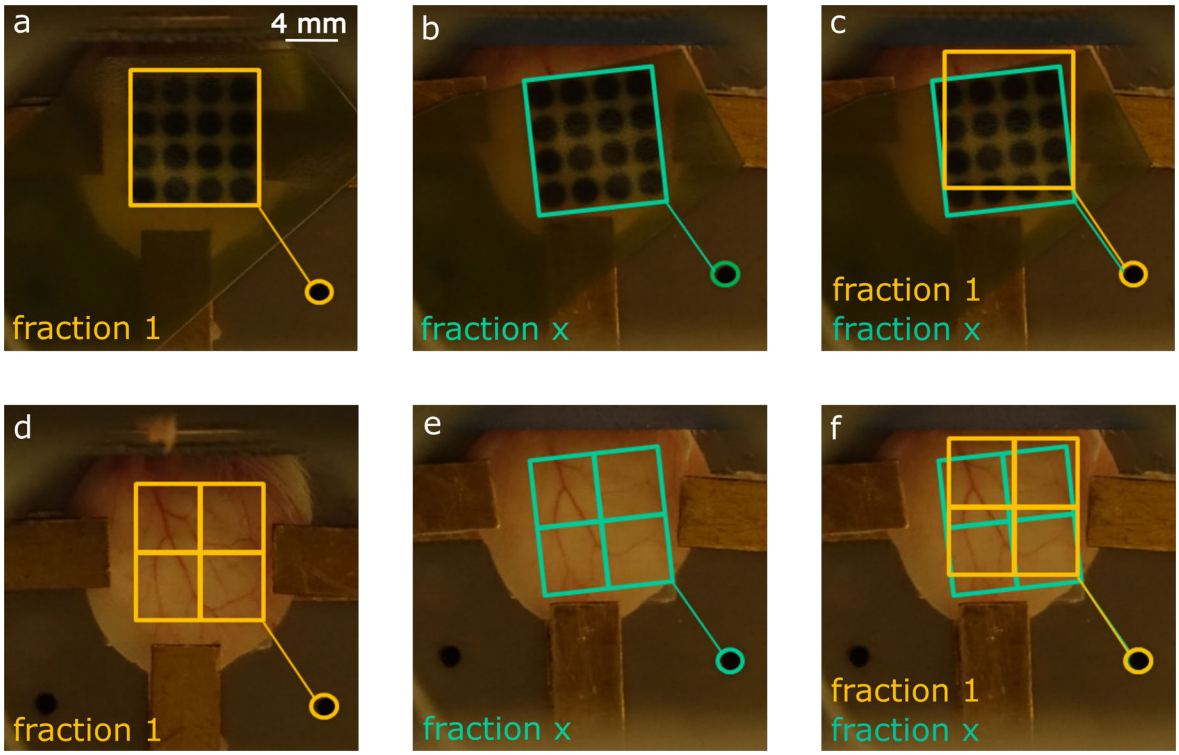

Figure 3.6: *Example for positioning analysis. Determination of the irradiation field from fraction 1 (yellow) with respect to absolute zero via the Gafchromic film (a) yields the irradiation field on the ear (d). Determination of the irradiation field of a subsequent fraction (geen) with respect to absolute zero via Gafchromic film (b) and the same irradiation field (green) transferred to the image of the ear (e). Cross-correlation between the irradiation fields (depicted in (c)) delivers the rotatory and translatory difference as determined and mechanically set on the irradiation day between the two fractions. The cross-correlation of the irradiation fields on the mouse ears (depicted in (f)) must result in the same rotatory and translatory difference as the cross-correlation of the yellow and green irradiation fields in (c) if a perfect matching was achieved. Differences between the cross-correlations determine the misalignment. Note that the misalignment also delivers the accuracy for the FS2 group (desired "misalignment") as shown in the pictures.*

3.4 Setup calibration for fractionated mouse ear irradiation

When the standard SNAKE setup was changed to fractionated mouse irradiation, it had to be calibrated for reliable positioning. At first, the SonyRX10 III camera was installed such that the resolution at the mouse ear location was maximal. Therefore, the camera was adjusted to be in focus at full optical zoom (600 mm lense).

At first, the angle between the camera and microstage had to be determined such that a table movement in the x- or y-axis also corresponded to a movement in x- or y-axis within the Matlab environment. A picture at absolute zero was compared to a picture after moving along the x- or y-axis. The offset of a pure x- or y-movement in the y- or x-direction yielded the angle between both systems and was compensated for any further calibrations and calculations within Matlab. This had to be repeated after any mechanical change of the setup (e.g. change of microstage, installing the camera).

As a second step, the absolute image resolution was determined using the microstage. A picture before and after a pre-determined movement (e.g. 2 cm) allowed for converting the pixel differences between the "absolute zero" into absolute distances. In the experimental setup, the pixel resolution was 12.6 µm/px.

At last, to determine the correct mechanical compensation, the mismatch of the rotational centers of the rotational stage and the analyzed picture had to be determined. The location of the irradiation field of fraction 1 was cropped out from the image of the inserted ear of a subsequent fraction. The cross-correlation of the cropped image with the image of fraction 1 delivered the necessary compensation factors within the Matlab environment. Applying the calculated rotation induced a translation if the rotational center of the images did not match the rotational center of the mechanical rotation stage. This translation depends on the angle and the difference between the two rotational centers. While the rotational center of the cropped image was set, the mechanical rotational center had to be determined. Therefore, a dummy at the ear location and absolute zero was compared with the same, only mechanically rotated dummy. The induced translation to the dummy image was used to calculate the difference between the two rotational centers using a transformation of coordinates. In turn, knowing the rotational center differences and the absolute center of mechanical rotation allowed for compensating the mismatch using a coordinate transformation and the falsely observed translations for any angle.

3.5 Animal model, ethic statements and treatment preparation

The animal studies were conducted within the healthy ear of 6 - 12-week-old, female BALB/c mice (Charles River Laboratories, Sulzfeld, Germany; Fig. 3.7) according to the German animal welfare regulations, with permission of local authorities and approval of an ethics committee.

Figure 3.7: *Picture of an adult female Balb/c mouse.*

The animal facilities of the Klinikum rechts der Isar (Munich) and the Helmholtz Center Munich (Neuherberg) were used for animal housing of the beam size study and the fractionation study, respectively. Both facilities are temperature-regulated and offer ad libitum access to water and food with a 12-hr day/night cycle.

BALB/c mice are an ideal target for irradiation experiments, since BALB/c is an albino mouse strain and typical external radiation responses such as reddening can easily be observed. The thin ears of the mice ($\sim$200 - 250 µm) allows for the irradiation with 20 MeV protons (range in water $\sim$4.6 mm) with a basically constant dose throughout the ear. Additionally, protons can be detected behind the ear, enabling an accurate absolute dose application. The size of the ears ($\sim$1 cm diameter) also allows for comfortable handling and observation during the treatment and monitoring period. The treatment of the ears is mouse-friendly in comparison to other skin models such as skin fold chambers. Finally, the unique vessel structure of every mouse is the ideal biological orientation for an accurate ear positioning for temporal fractionation (see section 3.3).

Mouse ears consist of two layers of skin separated by a cartilage layer, enabling a redundant observation of the skin response [109]. Only a few fat cells can be found in the ears of BALB/c mice, instead of the typical fat layer beneath the dermis [115].

The characteristics of mouse ear skin are not expected to change the radiation response compared to other skin parts [31, 109]. A histological section of a mouse ear is presented in Fig. 3.8. Although there are several differences of murine and human skin,

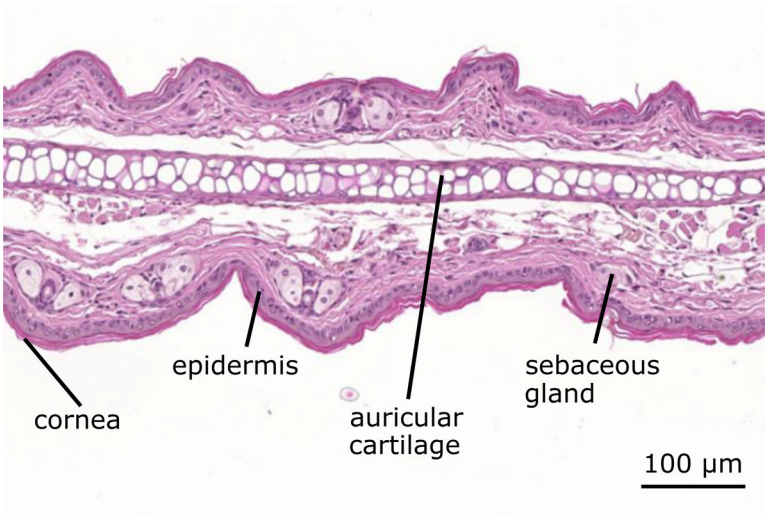

Figure 3.8: *Histological section of a BALB/c mouse ear.*
credit: Michaela Aichler

such as thicker skin in humans or differences in wound healing, murine skin helped a lot to understand the reactions of human skin [116]. The main radiation responses are similar in human and murine skin but the dose sensitivity is approximately twice as high in human skin [117].

All mice were anaesthetized by intraperitoneally injected medetomidine (0.5 mg/kg), midazolam (0.5 mg/kg) and fentanyl (0.05 mg/kg) for irradiation. The antagonist atipamezole (2.5 mg/kg), flumazenil (0.5 mg/kg) and naloxone (1.2 mg/kg) was administered subcutaneously after a maximum of 45 minutes [118].

3.6 Biological endpoints

The irradiation of mouse skin with 20 MeV protons causes damage in the cells and subsequently induces macroscopic radiation responses. Typical acute radiation responses are reddening, desquamation, and ear swelling, which appear within the first 2 - 6 weeks after irradiation according to Girst et al. [31]. Acute skin reactions were monitored over 90 days and 150 days after irradiation for the beam size study and the fractionation study, respectively. All persisting radiation responses were categorized as long-term side effects. After the monitoring period of the fractionated minibeam experiment,

histological ear sections were taken for observing any long-term changes within the microscopic anatomy of the ears.

3.6.1 Skin response scoring

After the exposure to radiation, initial damages and responses are only present on the cell level. When big areas of tissue are hit severely, a whole immune response starts. For an observation period of several months, a non-invasive and gentle quantification of the reactions needs to be established. Among the visible reactions, erythema and desquamation are not only easily accessible and quantifiable reactions, but also common side effects in radiotherapy [119]. Erythema or reddening of the skin is based on the increased blood flow (hyperemia) in superficial, dilated capillaries [120]. It can easily be diagnosed with e.g. finger pressure since it makes the erythema vanish. Desquamation, also known as skin peeling, describes the shedding of corneocytes from the stratum corneum, the outermost layer of the epidermis [121]. Nonpathologic desquamation is a normal mechanism, where individual keratinocytes are unnoticeably shed after being pushed upwards by descendant cells for several days (14 days in humans) [122]. Pathologic desquamation may result after injury of the skin. In case of radiation, the keratinocytes in the basal cell layer can be damaged, causing the detachment of clusters of cells, scaling the reaction to a visible level from dry to moist desquamation [122]. The severity of the desquamation is attributed to the damage within the basal cell layer. The reduction of clonogenic cells leads to dry desquamation whereas the damage of high proportions of the basal cell layer results in loss of epidermis and uncovering of the dermal layer characterizing moist desquamation [123]. Finally, the healing process of open, wounded irradiation areas leads to crust formation, an outer layer formed by drying out body exudate or secretion.

Erythema and desquamation were scored under the four-eyes principle in four grades (see Table 3.1), as established within the PhD thesis of Stefanie Girst [109]. The individual scores were summed to a total skin reaction score with equal maximum weight. A non-linear scale was chosen for erythema due to the inconclusive transition from “no” to “mild” erythema and allowed for further discrimination of the reaction.

In radiotherapy, erythema and desquamation appear after around 2 - 4 weeks [123]. In mice, the turnover time, which is the time until the epidermis replaces itself, was determined to $\sim$ 8 - 9 days [124]. The maximum visible skin reaction appeared at around 25 - 30 days [31, 109].

Other visible skin reactions such as hair loss and morphological changes were evaluated but could not be quantified.

erythema	score	desquamation	score
no	0	no	0
mild	0.5	dry	1
definite	1.5	crust formation	2
severe	3	moist	3

Table 3.1: *Skin score table. The scores were evaluated independently by four-eyes principle. The total skin reaction score was defined as the sum of the corresponding erythema and desquamation score.*

3.6.2 Ear thickness measurement

The ear thickness of the right, treated ear and the left, untreated ear was obtained by an electronic measuring gauge. The contacts of the measuring gauge were 6 mm. For the beam size study, the C1X079 (Kröplin GmbH, Schlüchtern, Germany) was used and was substituted by the C1X018 (Kröplin GmbH, Schlüchtern, Germany; see Fig. 3.9) for the fractionated minibeam study due to mechanical failure during experimental preparation. The design and the properties of both are, however, identical. To conduct the measurement, the second person fixed the mouse and the author measured the ear thickness three times each ear.

Figure 3.9: *Electronic measuring Gauge C1X018 (Kröplin GmbH, Schlüchtern, Germany) as used for ear thickness determination.*

3.6.3 Histology

Most of the content in this section is reprinted with permission (author reprint) from: Sammer, M. and Dombrowksy, A. *et al.* Normal tissue response of combined temporal and spatial fractionation in proton Minibeam Radiotherapy.
International Journal of Radiation Oncology Biology* Physics* **109** (2021) 76-83.

After the observation time of 150 days of the fractionation experiment, mice ears were prepared for histological analysis. The pinnae were excised after the cervical dislocation, fixed in formaldehyde solution, and exhaustively sectioned into transversal, equidistant ($\sim 2\,\mathrm{mm}$), parallel slices by the pathology of the Helmholtz Center Munich. Per pinna, three to four slices were systematically randomly sampled, embedded in paraffin, sectioned, and stained with either hematoxylin and eosin (H&E), or Sirius Red [125]. H&E staining allows for resolving the fine structure of the ears and its examination. Sirius Red stains the collagen within the mouse ears, allowing to detect fibrosis. The quantification of Sirius Red stained collagen was performed by automated digital image analysis (Definiens Architect XD, Definiens Inc., Carlsbad, CA, USA). In the sections, the volume fraction of dermal Fibrous Connective Tissue (FCT) within the pinna ($V_{V(FCT/pinna))}$ was determined as

$$V_{V(FCT/pinna))} = A_{A(FCT/pinna))} = \frac{A_{FCT}}{A_{pinna}}, \tag{3.1}$$

where A_{FCT} is the FCT area in the section and A_{pinna} is the total pinna tissue area in the section. The volume fraction or volume density $V_{V(FCT/pinna))}$ and the area fraction $A_{A(FCT/pinna))}$ are equal according to the principle of Delesse [126, 127]. To conclude to the total FCT content of the pinna, the volume density represented by $A_{A(FCT/pinna))}$ was multiplied with the measured ear thickness as it is the only geometrical dimension influenced by irradiation. Furthermore, inflammation was assessed and semi-quantitatively graded from 0 to 2 as otitis score according to the study of Dombrowsky and Schauer et al. [125], performed in the same animal model.

Chapter 4

Proton pencil minibeam irradiation with different beam sizes

The content in this chapter has already been published. Several sections, which are adapted and minorly corrected for this thesis, are mainly reprinted with permission from:
Sammer M. *et al.* Proton pencil minibeam irradiation of an in-vivo mouse ear model spares healthy tissue dependent on beam size.
PLoS ONE **14**, e0224873 (2019).

The first experiments concerning proton Minibeam Radiotherapy [29, 31, 32] showed a tremendous sparing potential by this novel spatially fractionated irradiation method. A detailed theoretical investigation states that the tissue-sparing decreases with depth due to the small-angle scattering of the proton beams [99]. The tissue-sparing is dependent on the beamsize σ to *ctc* ratio σ/ctc and the applied mean dose. Both parameters allow to fully describe the spatially fractionated dose distributions (see also section 2.2.4). As a third parameter, the single beam size has to be taken into account. The application of a single X-ray beam (with comparable biological effects, *RBE* of protons ∼1.1 [75]) with a 60 Gy plateau dose showed that only beams smaller or equal to 2 mm FWHM (Full Width at Half Maximum) resulted in minor side effects in mice ears [128]. Skin toxicities increased strongly up to the applied maximum beam size of 6 mm [128]. In pMBRT, a grid of beams is applied with several mm *ctc* distance. With tissue depth, the beam size increases and adjacent beams start to overlap. Hence, the cells and areas between the beams are also significantly harmed and tissue-sparing is decreased. Additionally, if beam sizes are smaller than 2 mm (FWHM), the radiation response is mainly dependent on the σ/ctc ratio.

The presented study investigated the radiation response dependency on the σ/ctc

ratio. Due to the limited ear size the beam sizes were varied rather than the *ctc* distances. Proton pencil minibeam sizes from $\sigma = 95$ µm to $\sigma = 883$ µm were applied with a 60 Gy mean dose on a 4×4 grid with center-to-center distance $ctc = 1.8$ mm, corresponding to σ/ctc ratios between 0.05 and 0.5. The largest σ/ctc of 0.5 corresponds to a homogeneous irradiation. The radiation responses visual scoring and ear thickness (see section 3.6) were monitored for 90 days post-irradiation. The results provide an insight into the sparing effect of different dose distributions of minibeam irradiations as they could be applied on the skin or as they occur in depth due to the lateral spread of the minibeams. Also, cell survival calculations were made as a first-order approximation to get a deeper understanding of the mechanistic effects involved in the sparing effect.

4.1 Materials and methods

The right ears of BALB/c mice were irradiated with a minibeam pattern, which consisted out of 4×4 beams with *ctc* distances of 1.8 mm, as in previous studies [29, 31]. This *ctc* is suitable for a tumor in 5–8.5 cm depth as illustrated in Fig. 4.1 and the number of beams was the largest fitting on the mouse ears and is – in therapy — adapted to the lateral tumor dimensions. The number of protons ($\sim 4.58 \times 10^8$) within the single beams were kept constant, such that a mean dose of 60 Gy was applied over the irradiated area (7.2 „ $\times$ 7.2 mm; similar to the previous study of Girst et al. [31]).

Seven groups, each consisting of 8 BALB/c mice, were exposed to a single fraction minibeam irradiation and classified by the applied σ/ctc ratios of 0.053, 0.11, 0.17, 0.23, 0.31, 0.49 (corresponding beam sizes in standard deviation σ: 95, 199, 306, 411, 561, 883 µm, respectively). The desired beam sizes were selected by the expected valley doses of 0, 0, > 0, ~ 15, ~ 30 and 60 Gy. One group was sham irradiated as a control. All mice were monitored in intervals of 1 – 4 days dependent on the extent of the reaction for a 90-day follow-up period.

4.1.1 Calculation of clonogenic cell survival in epidermal keratinocytes

The survival of cells in the ears after irradiation contributes to the measurable ear reactions such as desquamation and ear swelling. One of the main responsible cell types for the acute skin reaction after irradiation are keratinocytes [125, 129]. Hence, the Linear-Quadratic model was applied to the irradiated dose distributions of the six different minibeam sizes, using the corresponding $\alpha = 0.2\,\mathrm{Gy}^{-1}$ and $\beta = 0.06\,\mathrm{Gy}^{-2}$ values

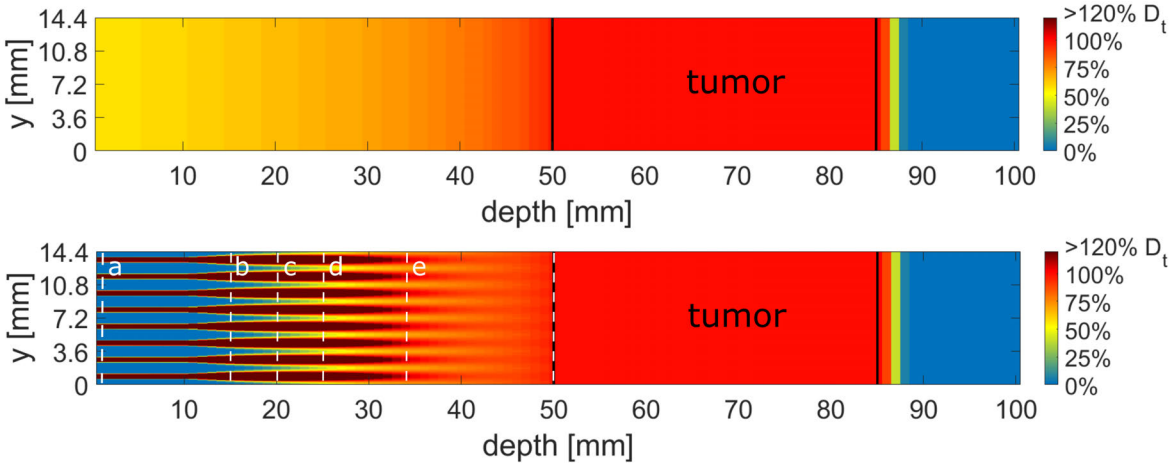

Figure 4.1: *A side cut of the calculated dose distribution of a conventional proton irradiation (upper image) and a proton minibeam irradiation (lower image) for a tumor in 5–8.5 cm depth. The mean dose for both scenarios is the same in every depth, however, the distribution of the dose varies strongly. The dose is color-coded with a cut-off at 120 % of the desired tumor dose D_t. The black lines indicate the beginning and the end of the tumor. The dashed white lines labeled with a–f show the location where calculated minibeam sizes are the same as in the experimental setup with ∼ 95, 199, 306, 411, 561 and 883 µm, respectively.*

for keratinocytes according to Parkinson et al. [130]. Ideal Gaussian dose distributions of standard deviation σ were taken for the minibeams that are placed on a quadratic grid of center-to-center distances $ctc = 1.8$ mm. The dose per minibeam was chosen such that a mean dose of 60 Gy was calculated for an infinite irradiation field. Within this approximation, the clonogenic cell survival depends only on the ratio σ/ctc. For each σ/ctc, the physical doses were translated into clonogenic cell survival via the Linear-Quadratic model and subsequently the mean within a unit cell of the pattern was determined similarly to the theoretical study of Sammer et al. [99]. The effects of the high doses within the beams were overestimated using the Linear-Quadratic model, which is only accurate up to ∼ 10 Gy. However, they differed only slightly in their absolute values if a linear extended model was used and could be neglected if only the percentage scale was taken into consideration [99].

4.2 Results

4.2.1 Dose distributions for proton pencil minibeams and size verification

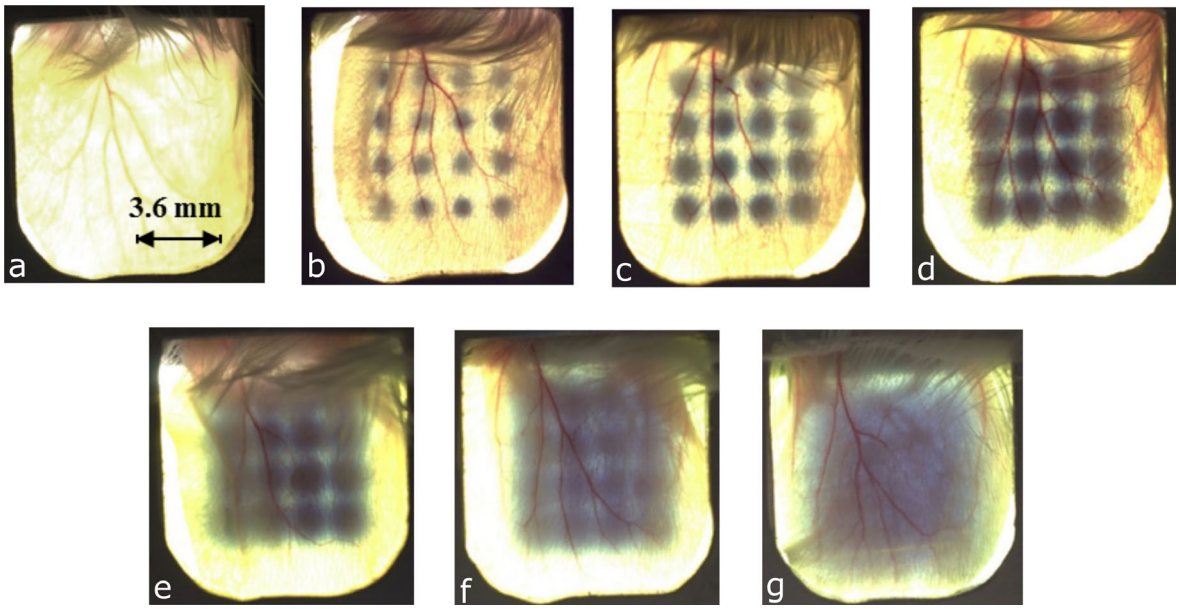

Figure 4.2: *Gafchromic films mounted behind mouse ears show the irradiation pattern for non-irradiated ears (a) and irradiations with σ/ctc ratios of 0.053 (b), 0.11 (c), 0.17 (d), 0.23 (e), 0.31 (f) and 0.49 (g) at $ctc = 1.8\,mm$ each. (g) corresponds to a homogeneous dose distribution. Owing to the limited sensitivity range of the films, no absolute dose values or minibeam sizes can be extracted from these images.*

Fig. 4.2 shows a photograph of one mouse ear from each group after irradiation with a mean dose of 60 Gy. A Gafchromic EBT3 film was placed behind the ear to verify the irradiation and visualize the different minibeam sizes. The applied 60 Gy mean dose was larger than the sensitivity range of the Gafchromic films and the shown films were therefore unsuitable for absolute dose verification. The absolute mean dose was measured by particle counting as (60 ± 3) Gy. The dose uncertainties result from the radiochromic dosimetry which was necessary to correct for the dead times of the proton detection. The dose profiles and beam sizes were analyzed by additionally irradiated Gafchromic EBT3 films, where doses were adjusted such that they matched the sensitivity range. The measured beam sizes, i.e. standard deviations were obtained from fitting a Gaussian distribution over the profile of a single irradiated beam for each beam size (cf. Table 4.1). Beam size uncertainties result from two independent

σ [µm]	95.3 ± 1.4	198.6 ± 1.7	305.7 ± 2.5	411.0 ± 2.1	561 ± 4	883 ± 5
$PVDR$	> 540	> 132	47 ± 20	10.1 ± 0.9	2.69 ± 0.19	1.11 ± 0.10
σ/ctc	0.053	0.110	0.170	0.228	0.312	0.491

Table 4.1: *Beam sizes were measured twice with a Gafchromic film placed at the corresponding ear positions. The PVDR was extracted from the profile cuts. The PVDR values of the pattern with the two smallest beam sizes can just be given as a lower limit since the valley doses are lower than the noise level of the Gafchromic film. The given uncertainties arise from the Gaussian propagation of the determination of the maxima and minima to calculate the PVDR. The σ/ctc values are calculated as the corresponding beam size σ divided by the center-to-center distance ($ctc = 1.8\,mm$).*

measurements of the beam sizes. Fig. 4.3 shows the dose modulation differences, which varied from Peak-to-Valley Dose Ratios $PVDR > 540$ to $PVDR \sim 1.1$ for the smallest to the largest beams, respectively.

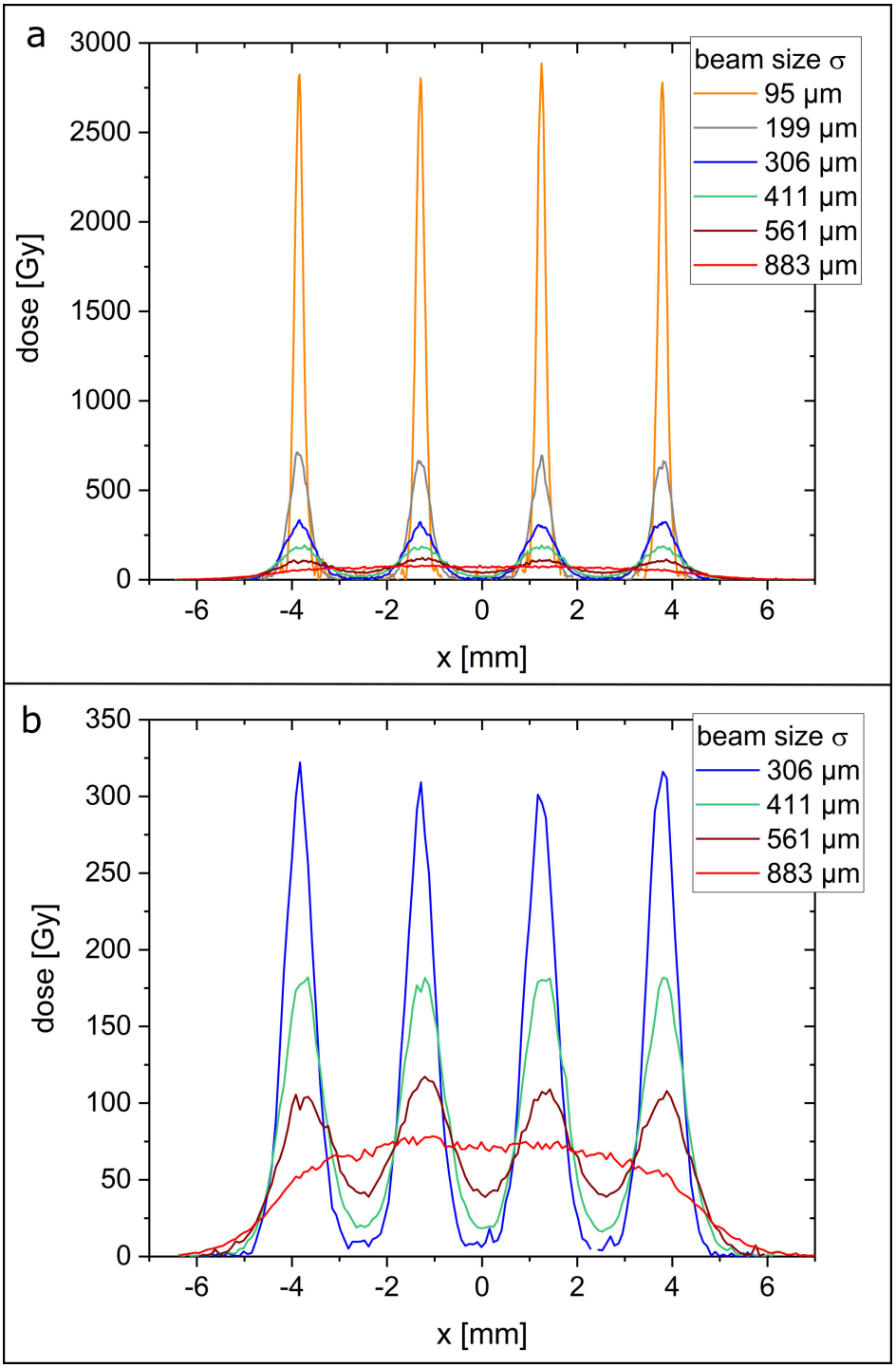

Figure 4.3: *a) Exemplary measured dose profiles via radiochromic film irradiation extrapolated to an average dose of 60 Gy. b) The dose profiles of the largest four beam sizes are shown on an enlarged dose scale. All profiles were cut diagonally to the pattern to show the absolute minimum and maximum dose, hence the shown ctc distances are increased by the factor* $\sqrt{2}$.

4.2.2 Skin response scoring

The skin response was scored according to the scores of Table 3.1 in intervals of 1 – 4 days dependent on the severity of the acute skin response for 90 days post-irradiation. The skin response score, defined as the sum of erythema and desquamation, is shown in Fig. 4.4. The error bars result from the statistical errors of the eight in-

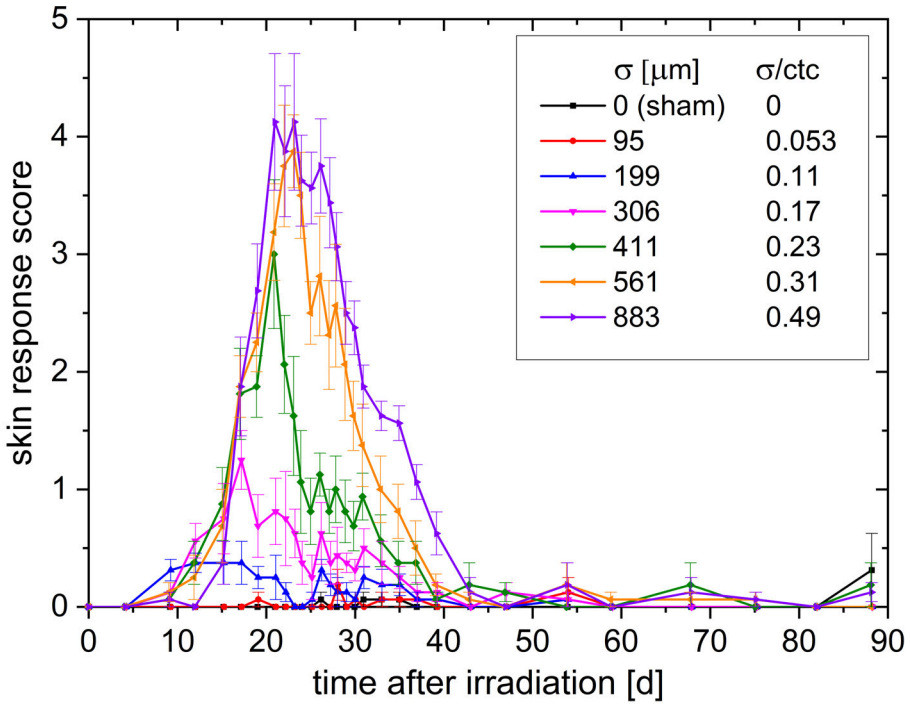

Figure 4.4: *Mean score over monitoring time (sum of desquamation and erythema score ± SEM).*

dependent mouse measurements in addition to an estimated systematic error of 0.5. The score of the mouse group irradiated with the smallest minibeams ($\sigma/ctc = 0.053$, red line in Fig. 4.4) was not distinguishable from the sham score (black line) during the 90-day monitoring period ($p > 0.15$). For all groups irradiated with σ/ctc ratios ≥ 0.11, a clear skin response was observable ($p < 0.05$). However, the skin response became more severe with increasing σ/ctc. The strongest overall reaction was obtained for the $0.49\,\sigma/ctc$ ratio, which corresponds to a homogeneously irradiated field. No skin reactions were found for any group later than ~ 45 days after irradiation. The temporal progression, i.e. onset, fall off and the maximum of the reaction started earlier for smaller beam sizes and therefore correlated with higher peak doses.

4.2.3 Measurement of ear thickness

The measurement of the ear swelling was conducted at the same time points as the skin response scoring. The mean ear thickness over the monitoring time of 90 days is shown in Fig. 4.5. The ear thickness over time of each mouse is depicted groupwise in Appendix A.

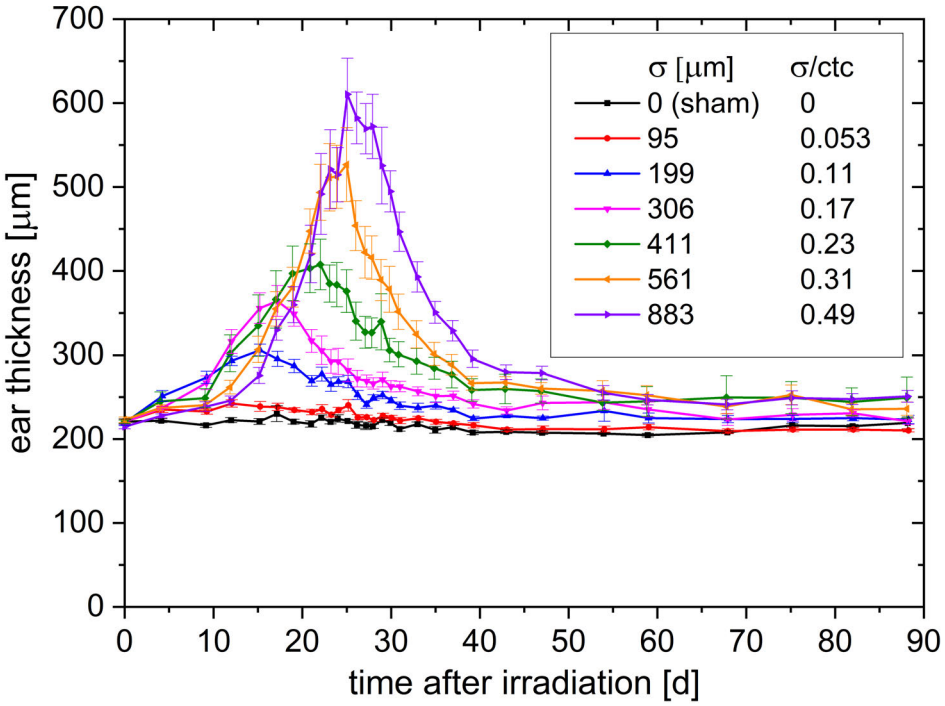

Figure 4.5: *Mean ear thickness (± SEM) over time after irradiation.*

There was a strong correlation between maximum ear swelling and applied beam size ($p < 0.01$). While the $\sigma/ctc = 0.053$ induced just a little ear swelling compared to the sham irradiated control group, the thickness increased strongly with increasing beam sizes. The homogeneously irradiated field with $\sigma/ctc = 0.49$ induced the strongest to a maximum ear thickness of about 610 µm, hence about a 3-fold ear swelling (initial ear thickness $\sim$ 200 µm; $p < 0.01$). The temporal progression of the swelling curve confirmed the observed skin score data, with a trend towards earlier onset and maximum for the smaller σ/ctc ratios. The ear thickness of time points later than 60 days after irradiation reached a steady state. This was similar for the skin response scoring, where no significant visible reaction was scored for time points later than 45 days after irradiation. However, the irradiation groups with $\sigma/ctc > 0.11$ tended towards a slightly

increased ear thickness up to the end of the experimental observation time, with even thicker ears (swelling $\sim 30-40$ µm) for larger irradiated σ/ctc ratios (>0.23). This persisting ear thickening might indicate long term side effects like fibrosis, but needs to be clarified in further studies.

If the maximum ear thickness (appearing at different time points for the individual groups) is plotted over σ/ctc as shown in Fig. 4.6a, a linear correlation between maximum ear thickness and σ/ctc is obtained. The control group was excluded for the fit since no radiation-induced ear swelling appeared in the untreated ears and would, therefore, falsify the linear effect observed.

A point of intersection was found at $\sigma_{min}/ctc \sim 0.032$ between the fit and the minimum thickness of the mouse ear (control $t_0 = 225$ µm). This represents the σ/ctc below which no ear swelling could be detected and corresponds to a minibeam size of $\sigma \sim 58$ µm for the utilized ctc of 1.8 mm. The skin responses and thickening reactions showed some interesting details in their time courses. While the maximum reactions were reduced for smaller beam sizes, the start of the reactions began earlier. Thus, the reactions of the smaller minibeam sizes were even slightly enhanced at the first 10 to 20 days compared to the close to homogeneous irradiations. A monotonic increase was observed between the time point of the half maximum ear swelling t_{50} and σ/ctc as shown in Fig. 4.6b. The time shift towards earlier time points for smaller σ/ctc and thus higher maximum doses may indicate an influence of different cell death pathways for the high dose irradiated cells within the ears.

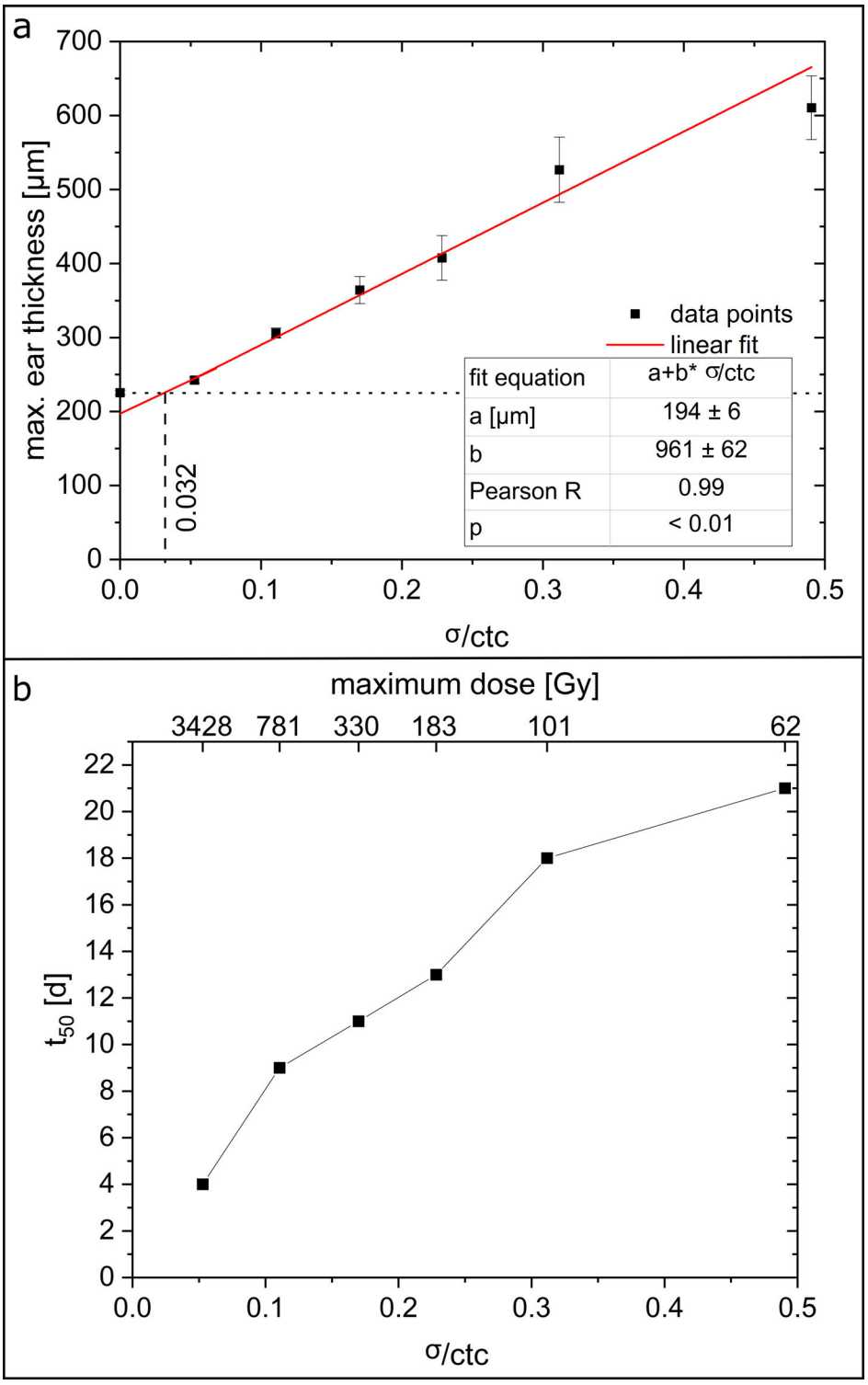

Figure 4.6: *a) Maximum ear thickness over beam size σ to ctc ratio σ/ctc. The red line corresponds to a linear fit ($R = 0.99$). The dashed lines mark the ear thickness of the control ear and the intersection point of control ear thickness and linear fit. b) Time point t_{50} of half the maximum ear swelling over σ/ctc. The corresponding maximum doses are shown on the top x-axis.*

4.2.4 Clonogenic cell survival calculation

The clonogenic cell survival within minibeam irradiated areas was calculated as a first-order approach to get a deeper understanding of the observed reactions. The calculated clonogenic cell survival using the LQ-model is plotted over σ/ctc in Fig. 4.7a for a 60 Gy mean dose. For σ/ctc greater than 0.2, there was less than 5 % clonogenic cell survival with a sharp decrease for even bigger σ/ctc, while the survival rate was larger than 90 % for σ/ctc ratios smaller than 0.1 due to the spatially fractionated sparing. The clonogenic cell survival remained the same for all beam sizes as long as the σ/ctc and the mean dose stayed the same. The radiation responses may still change depending on the absolute size of the minibeams due to the repair mechanisms of the tissue. A single-beam experiment showed a restriction of < 2 mm (FWHM) for the occurrence of only mild skin reactions [128].

The measured maximum acute radiation toxicity, represented by the maximum mouse ear thickness, is plotted versus the calculated clonogenic cell survival for the corresponding σ/ctc in Fig. 4.7b. While the maximum ear thickness increased just slowly with decreasing cell survival, a close to zero cell survival did not show a saturation effect. The three biggest σ/ctc (> 0.23), which all resulted in < 1 % cell survival, showed very different responses with the strongest response for the $\sigma/ctc \sim 0.5$, equivalent to a homogeneous irradiation.

Thus, the number of proliferating cells may not be the only parameter that determines the radiation responses. On the one hand, cells that are stopped from proliferation can still maintain their function for a certain time before they start behaving differently or vanish. On the other hand, cells irradiated with hundreds of Gy may not only be stopped from proliferating but may have a higher probability of necrosis or apoptosis, which in turn alters the tissue repair. Furthermore, migration of viable cells adjacent to the minibeams needs to be taken into account for tissue repair, which is again dependent on the size of the radiation-injured area. However, detailed models may also include cell signaling between irradiated and un-irradiated cells and are missing to calculate the cell death pathway fractions for different doses as they appear in the inhomogeneous dose distributions of spatial fractionation.

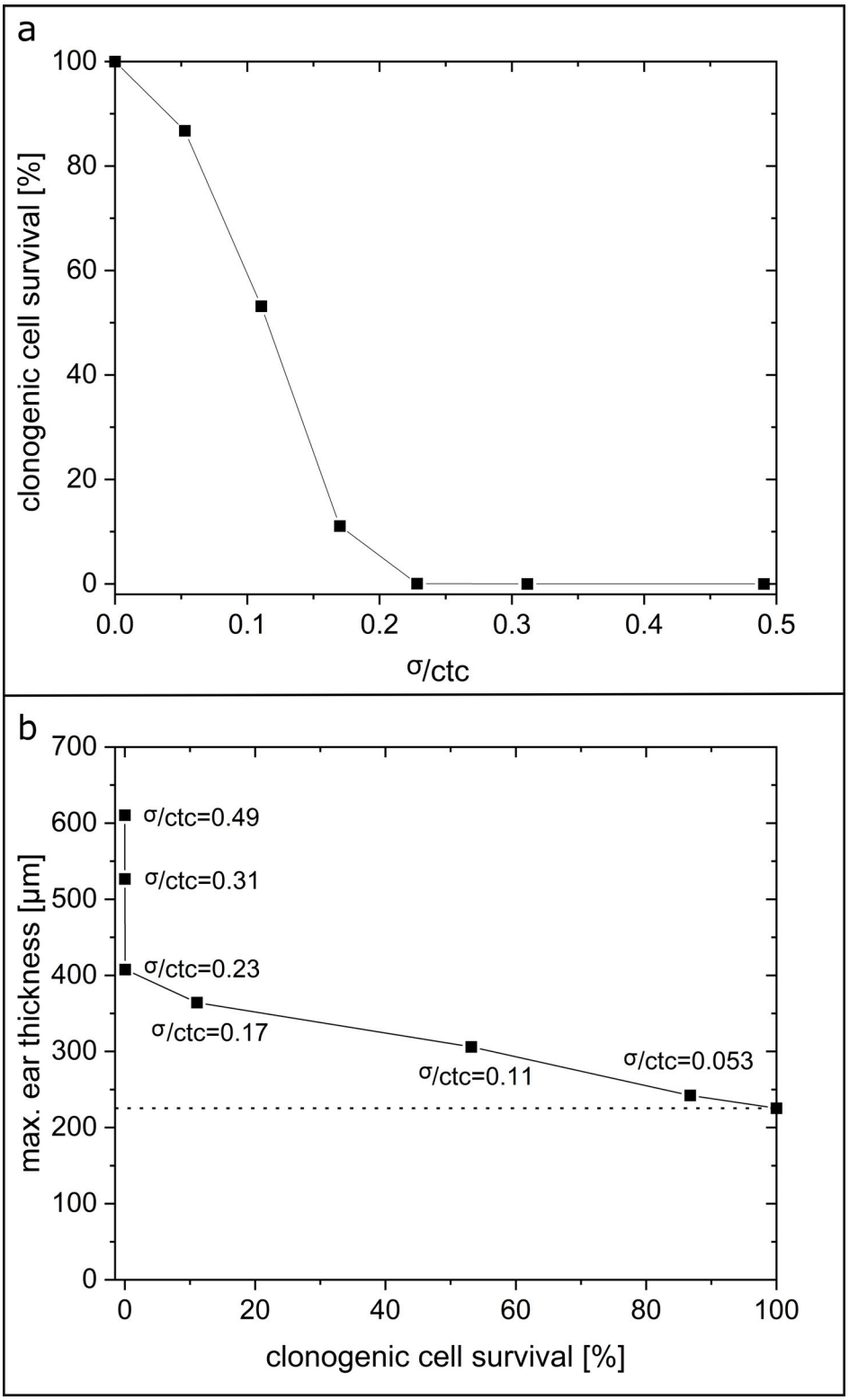

Figure 4.7: *a) Clonogenic cell survival of mouse keratinocytes in dependence of the σ/ctc ratio. b) Maximum ear thickness over the calculated clonogenic cell survival of the corresponding σ/ctc. The dotted line marks the max. ear thickness of the unirradiated group.*

4.3 Discussion

The scheme of a unidirectional proton Minibeam Radiotherapy (as discussed in [29, 31, 99]) allows a homogeneous dose coverage of the tumor while profiting from spatial dose fractionation in the healthy tissue. A similar unidirectional approach by applying X-ray micro- or minibeams to cover the tumor homogeneously is not possible since dose is also deposited distally to the tumor. Heavy ions (e.g. He-ions, boron, carbon, or oxygen ions) are also suitable for minibeam therapy just as protons, but the beams have to be initially smaller since the lower scattering of heavier ions requires smaller *ctc* distances to form a homogeneous tumor dose, while also sparing healthy tissue.

Unidirectional proton or heavy-ion minibeam therapy is technically less demanding than using interlacing minibeams from various directions. Interlacing particle minibeams would have even larger sparing potential since spatial fractionation effects can be maintained close to the tumor. Particle minibeams from more directions can be interlaced due to the limited range of the particle beams, enabling interlacing even from opposite directions [27, 29, 131]. Nevertheless, interlacing beams is technically more demanding to fulfill due to the necessary precision of beam adjustments to obtain dose homogeneity in the tumor. Besides, interlacing micro- or minibeams would suffer much more from organ and/or tumor movement.

In either case, tumor control can be expected to be the same as in conventional radiotherapy when the same homogeneous dose distribution is applied within the tumor. This may be an advantage compared to the proposed X-ray micro- and minibeam approaches which retain an inhomogeneous dose distribution within the tumor [132, 133]. Even though the results of the animal studies in terms of tissue-sparing of healthy tissues are very promising for future implementation into clinics, more detailed investigations need to be carried out in terms of beam sizes, *ctc* distances of the beams, mean doses applied, and the dependence on penetrated tissues by the minibeams. Only afterwards, the sparing effects can be predicted and the full advantage of proton Minibeam Radiotherapy can be exploited.

The present study was carried out to compare side effects of proton pencil minibeam irradiations of different pencil beam sizes for a given grid pattern with 1.8 mm *ctc* distances in an in-vivo mouse ear model. The animal model allowed for a radiation response study of proton pencil minibeams in a living mammalian organism with similar radiation responses as in human skin, even though the doses necessary to induce similar side effects in humans might vary. The direct comparability of the different irradiations was ensured by keeping the mean dose (60 Gy) and the *ctc* distances (1.8 mm) constant. Only the beam sizes of the proton pencil minibeams were varied from approximated Gaussian σ between 95 µm and 883 µm (σ/ctc ratios between 0.053 and

0.49). The experimental setup allows for different perspectives and interpretations of the results.

4.3.1 Determination of beam size to obtain full tissue-sparing by spatial fractionation

The results (Figs. 4.4 - 4.6) show the dependency of the skin reaction on the σ/ctc ratios for a mean dose of 60 Gy. By applying different beam sizes to the skin of the mice ears for a square grid of 1.8 mm *ctc* distances, the maximum σ/ctc ratio for a proton pencil minibeam radiotherapy which would result in no side effects was extrapolated to $\sigma/ctc = 0.032$. The results show that larger σ/ctc ratios were still beneficial compared to homogeneous irradiation, but side effects increased with increasing σ/ctc ratios. Considering a clinical irradiation scenario, beam sizes should be chosen smaller than given through the limit $\sigma < 0.032 \cdot ctc$. The *ctc* distances are generally determined by the size and the location of the tumor to realize a homogeneous dose distribution in the tumor [31, 99]. The closer the tumor is to the skin, the smaller the *ctc* distances have to be chosen to fulfill the homogeneity constraints for the tumor. This leads to even smaller initial beam sizes to obtain negligible radiation responses. Smaller proton beams are harder to prepare or cannot even deliver the beam currents for an efficient proton pencil minibeam radiotherapy treatment. The presented study showed that larger beams with $\sigma > 0.032 \cdot ctc$ showed some, but still less skin reaction than a homogeneous irradiation. Hence, when beam sizes are limited through technical constraints, a compromise of the tissue-sparing potential may still be acceptable and, most important, beneficial for the patients.

Since the critical σ/ctc ratio below which no side effects occurred is determined to $\sigma/ctc = 0.032$, the critical beam size is $\sigma = 60$ µm (FWHM ~ 140 µm) for the given $ctc = 1.8$ mm. In a previous experiment, single X-ray pencil beams were applied to the same mouse ear model and no side effects were found for sharply shaped beams up to 1 mm in diameter and a 60 Gy plateau dose [128]. The appearing difference may be due to the reduced number of proliferating cells in the close neighborhood of the minibeams within the grid pattern caused by the overlapping dose distributions. In addition, the number of apoptotic or necrotic cells, leading to a fast loss of the cells within the tissue, may be increased in the proton grid irradiation experiment since the maximum doses exceeded the 60 Gy mean dose by factors (see Fig. 4.3). This may lead to the faster but smaller reactions for the small minibeams (σ/ctc ratios: 0.11 – 0.23; σ: 199 µm to 411 µm; Figs. 4.4 and 4.5). According to the theoretical study [99], typical *ctc* distances to treat a tumor in a human body are between 1 – 6 mm. Concluding from

the mouse data, technical developments should ideally aim for $\sigma = 32$ µm. However, even σ/ctc ratios of $\sim 0.1-0.15$ induce only minor side effects, corresponding to beam sizes of $\sigma = 100-900$ µm at the assumed *ctc* range.

4.3.2 Dose distributions within a tumor irradiation scenario

Another perspective of the results is the interpretation of side effects for the different σ/ctc ratios as they appear in different depths for proton pencil minibeams on their way to the tumor in deeper-lying tissues (such as muscles or organs). The 1.8 mm *ctc* would be ideal to treat a target volume in $\sim 5-8.5$ cm depth (according to [99]). The necessary energies to irradiate such a target are between 79 and 107 MeV. The Relative Biological Effectiveness is $RBE \sim 1.1$ of both the used 20 MeV as well as the higher clinical energies and therefore barely influences the results. By increasing the beam sizes with 20 MeV protons, the dose distributions were similar to those appearing in depth from the higher energetic protons in the healthy tissue due to the small-angle scattering of the protons. A tumor treatment plan with proton minibeams was calculated and the dose distribution is shown in Fig. 4.1. The corresponding depths to the applied dose distributions are marked in Fig. 4.1 (white dashed lines) and the values are listed in Table 4.2.

σ/ctc	0.053	0.110	0.170	0.228	0.312	0.491
Beam size σ [µm]	95	199	306	411	561	883
Depth d [cm]	0	1.5	2.0	2.5	3.4	5.0

Table 4.2: *Corresponding depths to the irradiated σ/ctc ratios and beam sizes for an exemplary tumor in 5 – 8.5 cm depth.*

All irradiated dose distributions could be considered as artificial cuts (perpendicular to the beam incidence) from deeper layers of a unidirectional proton pencil minibeam treatment. The group with the biggest σ/ctc ratio of 0.49 played a particular role in this interpretation, as it represents the homogeneous dose distribution. From the unidirectional proton pencil minibeam treatment point of view, it is the dose distribution that appears in the target volume. For conventional proton therapy, however, it represents the (homogeneous) dose distribution in each depth of a tumor treatment, including the whole entrance channel in healthy tissues. Of course, the mean dose would increase with depth similar to conventional proton radiotherapy due to the Bragg curve in a unidirectional proton minibeam treatment. However, the study was conducted to observe the geometrical influences of a spatially fractionated proton pencil minibeam radio-

therapy on the healthy tissue response. Hence, it was necessary to keep the mean dose constant (60 Gy) to have a distinct outcome due to pure geometrical variations of the dose distributions rather than any additional influence of varying mean doses. Eventually, it is possible to compare the different minibeam irradiations, which represent the dose distributions of certain depths, to the corresponding conventional irradiation, all represented by the σ/ctc ratio = 0.49 group. Nevertheless, differences in proliferation, necrosis, migration, and repair in normal tissue types other than skin may influence the absolute beam sizes required for certain tissue reactions and will have to be elaborated in future studies.

The presented study revealed that most damage is caused by the homogeneous irradiation as it appears close to and within the tumor. Furthermore, not only the smallest σ/ctc ratios, but also larger σ/ctc ratios were found beneficial regarding the skin reaction and compared to the homogeneous case. This result may hold for any minibeam treatment case as long as the minibeam sizes are small enough so that radiation toxicities from single-beam irradiations also remain small. Total beam sizes smaller than 2 mm diameter for minor and less than 1 mm diameter for no skin reaction of single beams were obtained as upper limits for minibeam sizes [128]. The interaction of the beams in an irradiation grid depends only on the σ/ctc ratios as long as beam sizes are smaller than these single-beam limits. Thus, fewer side effects are expected in the whole entrance channel compared to conventional irradiation, with increasing benefits for tissues closer to the surface for a proton pencil minibeam radiotherapy treatment, as long as the discussed single-beam limits are not exceeded.

4.4 Conclusion

This study of skin reactions in a mouse ear model showed a clear reduction of side effects after proton pencil minibeam irradiation compared to conventional homogeneous irradiation. The variations of the beam size while keeping dose and *ctc* distances constant allowed for a differentiated insight into the beneficial effects of spatially fractionated dose distributions with protons that appear in the skin as well as in deeper layers. The study confirmed that technical developments need to aim for minibeam sizes below 0.1 mm at best. However, it was observed that any spatial fractionation with submillimeter proton beams led to reduced side effects compared to conventional treatment and therefore could become an attractive option in clinical proton therapy to increase the therapeutic index.

Chapter 5

Fractionated proton Minibeam Radiotherapy

The content in this chapter has already been published. Several sections, which are adapted and minorly corrected for this thesis, are mainly reprinted with permission (author reprint) from:
Sammer, M. and Dombrowksy, A. *et al.* Normal tissue response of combined temporal and spatial fractionation in proton minibeam radiotherapy.
International Journal of Radiation Oncology Biology* Physics* **109** (2021) 76-83.

The experiment of the previous chapter has shown clear evidence for the sparing of healthy tissue in the in-vivo mouse model. Additionally, it showed that the strongest adverse reactions were found for the homogeneous irradiation as it appears in the tumor. However, the irradiations were conducted in one fraction. In standard therapy, tumors are treated with temporal fractions on the basis of the 5 Rs of radiotherapy (see section 2.2.3). While the reduced side effects of temporal fractionation may be compensated by spatial fractionation for the healthy tissue, the tumor control can suffer due to cell cycle or reoxygenation effects, if not enough fractions or even only a single fraction are applied. Therefore, temporal fractionation may also be required in treatment with proton minibeams. The delivery of multiple fractions of proton minibeams can lead to a blurring of the minibeam pattern, when the minibeams are not irradiated to the exact same spots in each fraction. A change in patient positioning across multiple fractions leads to a pattern shift, affecting different tissue spots with each temporal fraction. This raises the question if radiation toxicity is influenced, for example due to an increased total valley dose. Hence, the tissue-sparing effect may be reduced, even if the daily Peak-to-Valley Dose Ratio $PVDR$ remains high. Repositioning in current radiation therapy can cause positioning errors of several

millimeters [134], which would be unacceptable for maintaining the same minibeam array over a full treatment schedule. Therefore, highly accurate patient positioning, within a few hundred micrometers, may be required to exploit the sparing effect of multiple fractions of proton minibeams in a clinical setting.

In this study, the effects of temporally fractionated proton Minibeam Radiotherapy in the context of reirradiation accuracy were investigated. Highly dose-modulated proton minibeams were applied in the extreme scenarios of either always (fractionation scheme 1; FS1) or never (FS2) hitting the same tissue spots in four daily fractions. Both scenarios produced either a high (FS1) or a low total dose modulation (FS2) after all four fractions. In a third scenario, a proton minibeam pattern with lower daily dose modulation but the same total dose modulation as FS2 was irradiated precisely at the same tissue spots for comparison. FS1 and FS2 answered the question of whether precise reirradiation with minibeams is necessary to sustain the extraordinary tissue-sparing effect of proton minibeams. In addition, the impact of the daily and integral dose modulation of minibeam arrays was tested.

5.1 Materials and methods

Four daily fractions of 20 MeV proton minibeams with a size of $\sigma = (222 \pm 5)$ µm were delivered every 24 hours to the right healthy pinna of female, 10- to 12-week-old Balb/c mice at the ion microprobe SNAKE at the Munich tandem accelerator in Garching, Germany. The left ear served as a control.

A mean fractional dose of (30 ± 4) Gy was applied to induce strong acute toxicity, as shown in the study of Dombrowsky and Schauer et al. [125] using the same mouse model. The correct dosage was ensured by a scintillator-photomultiplier detector counting particles behind the mouse ear (see section 3.2). Each minibeam was irradiated with 2.29×10^8 protons, delivering a 30 Gy mean dose to a 7.2 mm × 7.2 mm field, as used in previous studies [31, 118]. The beam size of an individual minibeam was determined by irradiating six radiochromic films at the ear location. The scans (1200 dpi) were evaluated by a Gaussian fit, resulting in a mean minibeam size of $\sigma = (222 \pm 5)$ µm.

Three fractionation schemes (FS) were tested (Fig. 5.1) and compared with sham-irradiation, using six mice per group (seven in FS2). Daily fractions of 16 minibeams at a *ctc* distance of 1.8 mm and a peak dose of 314 Gy were applied and accurately reirradiated in each fraction (FS1). In FS2, the same array was shifted by 0.9 mm (in x- or y- direction or both, respectively) for each fraction, hence avoiding any pre-

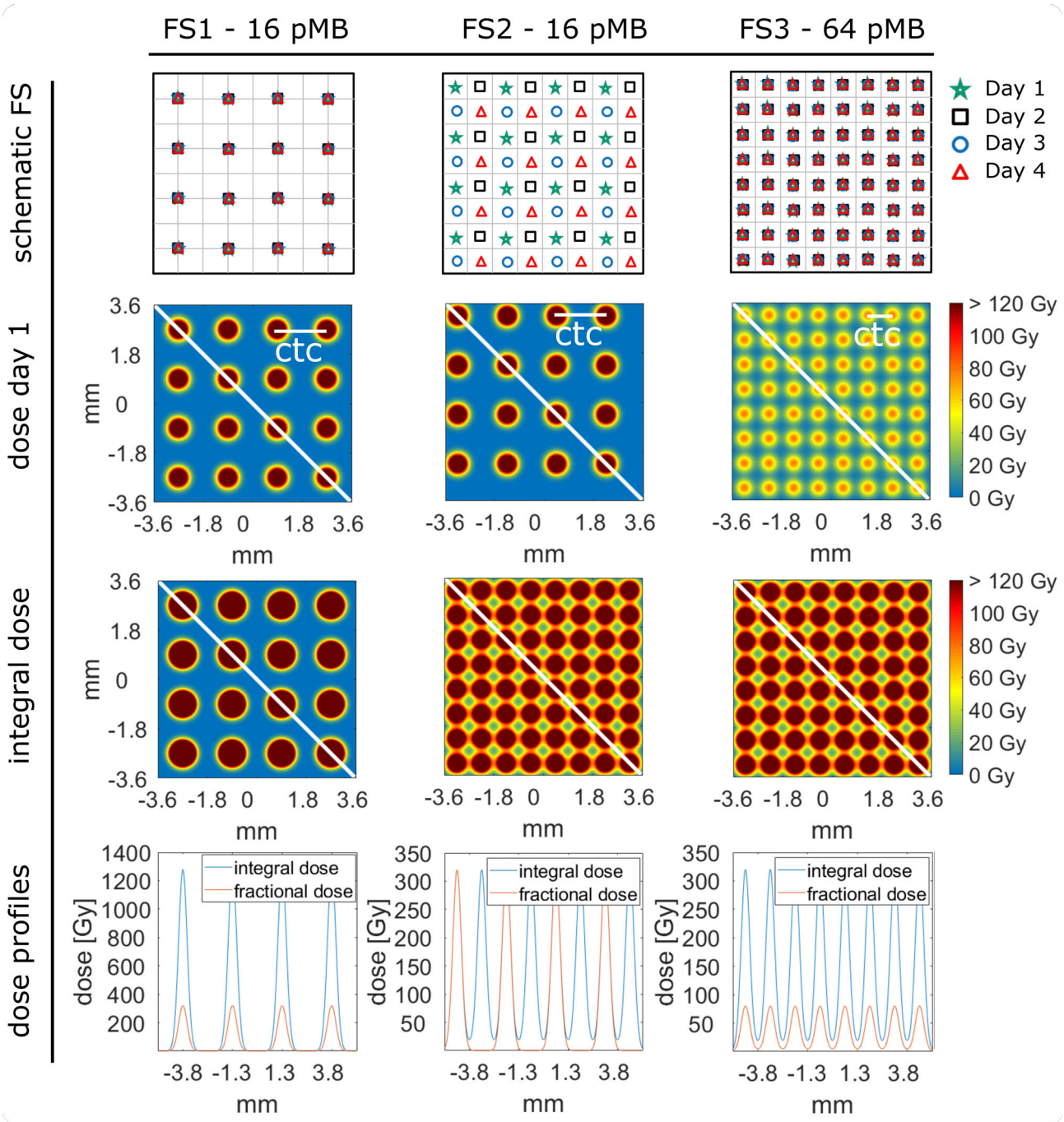

Figure 5.1: *Illustration of the three fractionation schemes (FS) and the corresponding fractional dose distributions and profiles. Four consecutive daily fractions of 16 proton pencil minibeams were delivered to either the same tissue spot (FS1; first row) or shifted by the half distance (0.9 mm) between two minibeams (FS2; second row) in each fraction. FS3 (third row) administered 64 minibeams with 25 % of the dose per minibeam used in FS1 or FS2. In every fraction of FS3, the same minibeam positions were irradiated to result in the same integral dose distribution as FS2.*

viously irradiated tissue. In the third scheme (FS3), four fractions of 64 minibeams with a *ctc* distance of 0.9 mm were applied to the same tissue spot, with 25 % of the protons per beam compared with FS1 and FS2 (peak dose of 78.6 Gy). The total dose modulation of both FS2 and FS3 coincided after all fractions. FS3 both served as a positive control and allows for comparison between FS2 and FS3, where the same total dose distribution was delivered but produced by different areal dose partitioning per temporal fraction.

The positioning setup (see section 3.3) allowed the reirradiation with an accuracy of (110 ± 52) µm. In the context of beam blurring in FS1 and FS3, the scatter in repositioning resulted in a fitted Gaussian beam size of $\sigma = (230 \pm 7)$ µm, assuming the sum of two Gaussians with $\sigma = 222$ µm and a distance of 110 µm. The small total dose spread from repositioning the individual dose patterns demonstrated the high positioning accuracy achieved, avoiding any additional side effects from beam blurring.

The histological preparations were carried out according to section 3.6. For statistical analysis, Graphpad prism 8.1.1 was used. Statistical tests were chosen according to the normal distribution and variance homogeneity. Statistical analysis of the otitis score was conducted by the Kruskal-Wallis test and Dunn's post hoc test. Statistical analysis of the maximum ear thickness and FCT content was conducted by the 1-way analysis of variance Tukey post hoc test.

5.2 Results

The applied dose distributions were simulated for each proton minibeam pattern using a Gaussian approximation for the individual beam size of $\sigma = 222$ µm and an ideal reirradiation accuracy. The results for the obtained peak and valley doses are presented in Table 5.1.

	FS1		FS2		FS3	
	per fraction	total	per fraction	total	per fraction	total
peak dose [Gy]	314	1256	314	314	78.6	314
valley dose [Gy]	0.03	0.12	0.03	20.6	5.2	20.6
PVDR	~ 10000	~ 10000	~ 10000	15.2	15.2	15.2

Table 5.1: *The values are calculated assuming a Gaussian beam profile. The valley doses of FS1 and the fractional dose of FS2 was estimated according to the study by Zlobinskaya et al. 2013 [29], where valley doses of ∼0.01 % of the mean dose were measured at the same irradiation setup.*

The mean dose per fraction of 30 Gy was kept constant between the groups. In total, a mean dose of 120 Gy was applied to each irradiated mouse ear. The dose distributions for the fractions of day 1 and the total dose modulations after four fractions are depicted in Fig. 5.1.

Figs. 5.2 and 5.3 illustrate the skin response score and ear thickening after sham irradiation and the three different temporal fractionation regimes.

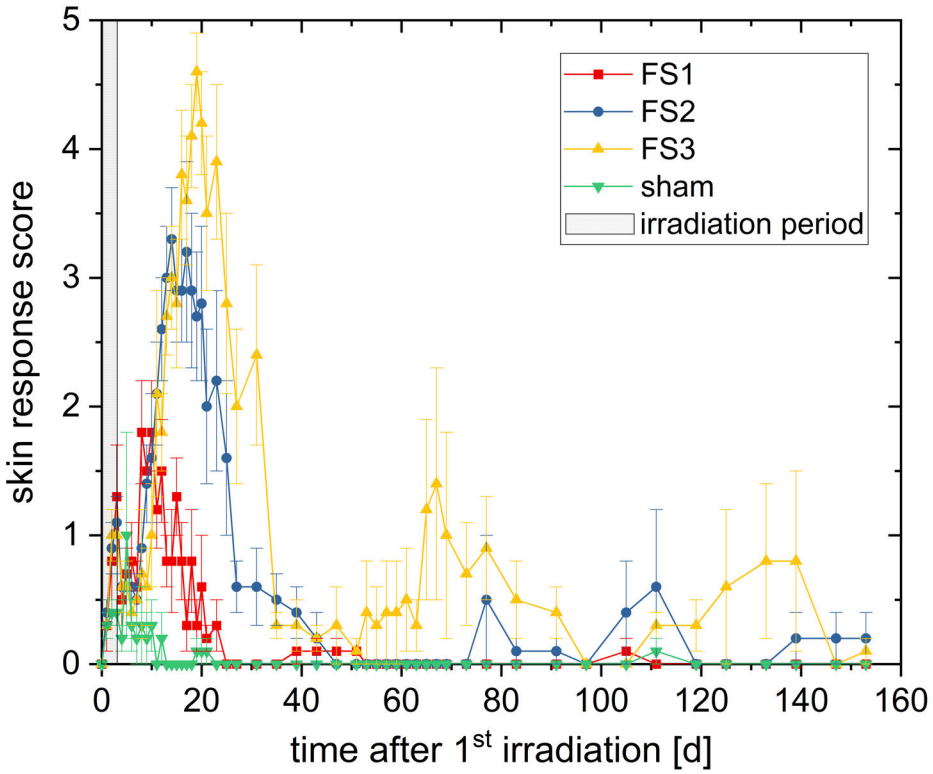

Figure 5.2: *Skin response score over time of the irradiated mouse ears for sham irradiation (green) and 3 different fractionation schemes (FS) of temporally fractionated proton pencil minibeams (FS1 - red, FS2 - blue, FS3 - yellow). Mean ± standard error of the mean is depicted. The skin response score is the sum of erythema score and desquamation score as defined in section 3.6. Day 0 was taken as the first day of irradiation.*

The resulting skin reactions depended on the applied dose pattern. All irradiated ears showed thickening and increased erythema and desquamation in comparison to sham ears. The skin reaction increased gradually from FS1 to FS3.

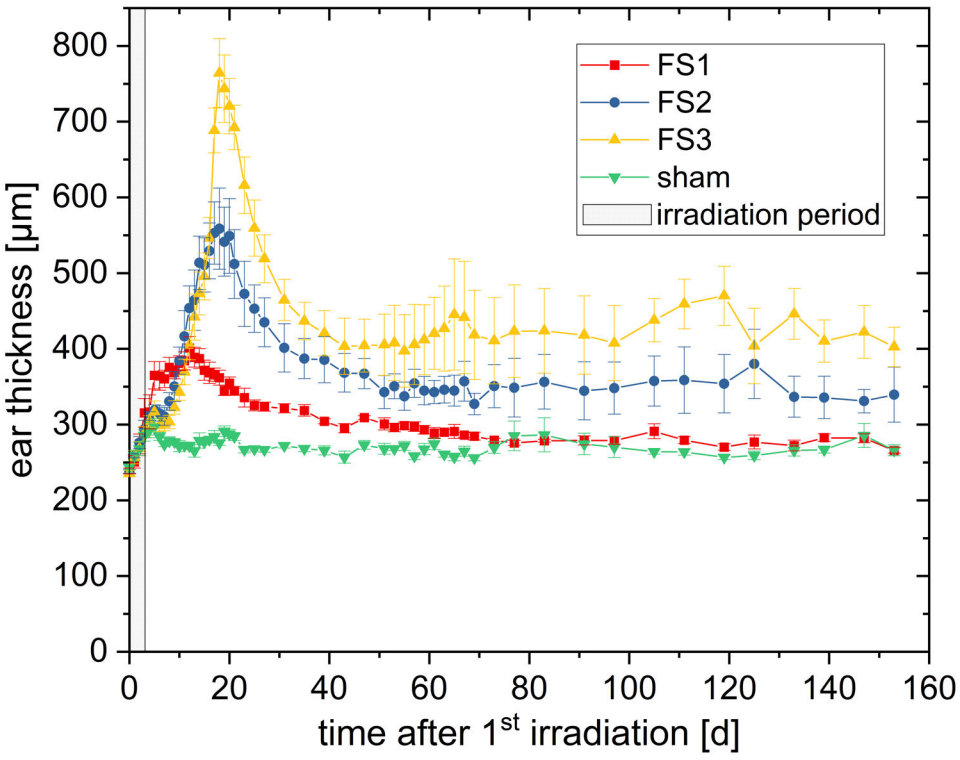

Figure 5.3: *Ear thickenss over time of the irradiated mouse ears for sham irradiation (green) and 3 different fractionation schemes (FS) of temporally fractionated proton pencil minibeams (FS1 - red, FS2 - blue, FS3 - yellow). Mean ± standard error of the mean is depicted. Day 0 was taken as the first day of irradiation.*

With respect to the skin response score (Fig. 5.2), the very first peak at day 4 was also observable in the sham group. This increase was caused by tissue stress of the clamping procedure. Afterwards, score increases were only visible for FS1 to FS3 and were attributed to irradiation-induced reactions. A peak in the score was observed for the FS1 ears on day 9 with a score of 1.8 ± 0.4, for FS2 on day 14 with a score of 3.3 ± 0.4, and for FS3 on day 19 with a score of 4.6 ± 0.3.

Fig. 5.3 shows the ear thickness during the monitoring period. Errors are given as the standard error of the mean. FS3 ears thickened significantly more ((784 ± 51) µm on day 18) than FS1 and FS2 ears. FS1 ears peaked at (401 ± 15) µm on day 12 ($P < 0.0001$), and FS2 ears peaked at (558 ± 54) µm on day 18 ($P < 0.01$), showing a slightly delayed maximum than the skin response score. From day 100 on, a nearly constant ear thickness was found in each group. The mean thickness of FS1 ears

((278 ± 9) µm) resembled sham ears ((266 ± 9) µm, $P > 0.05$). The final ear thickness on day 153 was significantly greater in FS2 ((349 ± 15) µm, $P < 0.0001$) and FS3 ((432 ± 18) µm, $P < 0.0001$) compared with FS1, indicating long-term toxicities. The ear thickness over time of each mouse is depicted per group in the Appendix B.

Fig. 5.4 depicts the representative histological sections of day 153 after the first fraction with H&E staining. A highly significant increase was found in the otitis score (Fig. 5.4), with an increased frequency and severity of inflammation (grade 0 - 2) in FS2 and FS3 on day 153. Moreover, there was a loss of hair follicles (arrows in Fig. 5.4) and increased epidermal thickening in FS2 and FS3 ears, whereas none of these reactions were found in FS1. Fig. 5.5 shows the total Fibrous Connective Tissue (FCT) content in mouse ears on day 153. The total FCT content of control, sham, and FS1 pinnae was not significantly different, whereas FS3 pinnae displayed significantly increased total FCT content compared with control ($P < 0.001$), sham, and FS1 pinnae ($P < 0.01$, Fig. 5.5). Thus, FS1 did not show any increase in the FCT content. FCT was less pronounced in FS2 than in FS3, but did not differ significantly.

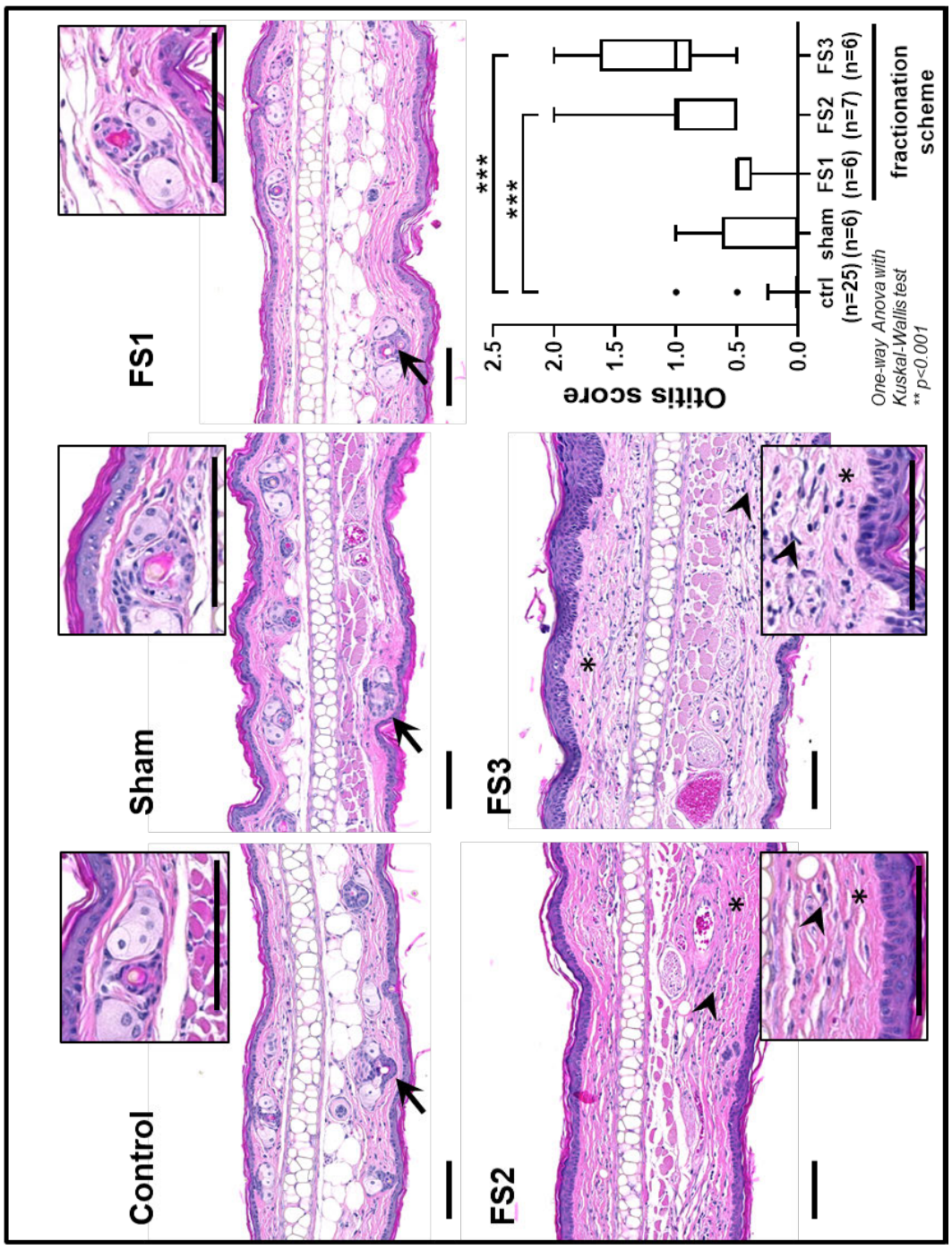

Figure 5.4: *Semiquantitative analysis of otitis score in hematoxylin and eosin in paraffin sections 153 days after fraction one of four proton pencil minibeam fractions. Representative H&E sections and otitis score showing medians and minimum/maximum values of each group. Ear sections of FS2 and FS3 mice display markedly increased fibrotic tissue in the dermis (asterisks), loss of hair follicles and adnexae (arrows), and moderate inflammatory cell infiltration (arrowheads). Scale bars = 100 µm.*

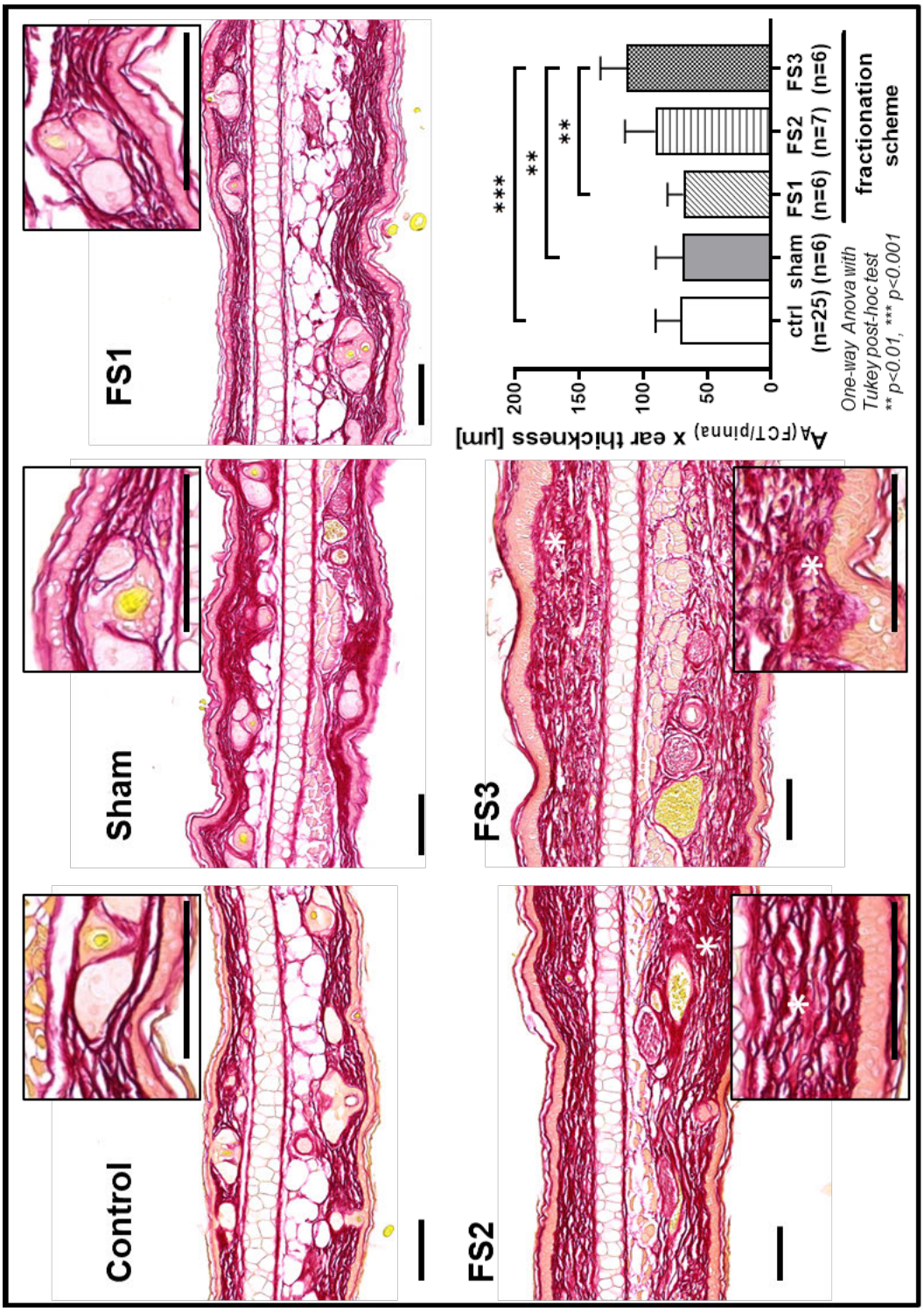

Figure 5.5: *Dermal extent of Fibrous Connective Tissue (FCT) 153 days after fraction one of four proton pencil minibeam fractions. Representative histology sections of the pinnae after Sirius red staining and FCT content. Given are the means ± standard deviations per group. FS2 and FS3 ears display markedly increased FCT content (asterisks). Scale bars = 100 µm.*

5.3 Discussion

The normal tissue response depended largely on the precision of reirradiation and the daily and total dose modulation of proton minibeams. Comparing FS1 and FS2, lower toxicity effects were found for FS1, which aimed for accurate reirradiation. The highly dose-modulated minibeams of each fraction were sustained in the total dose distribution with negligible blurring due to accurate reirradiation to the same tissue spots. Thus, the damage was confined to a small area over the complete treatment time. Despite the integrated mean dose of 120 Gy, inter-beam cells received a negligible dose (0.12 Gy). The undamaged valley cells are assumed to efficiently contribute to the repair of heavily irradiated tissue. This efficient repair may have a basis similar to that of Dilmanian's hypothesis about progenitor glial cells in the brain: Damaged tissue is repaired by proliferation and migration of intact inter-beam cells [135]. For FS2, the number of undamaged valley cells is reduced with every fraction, resulting in stronger side effects.

FS2 and FS3 resulted in the same total dose distribution, which was much less modulated than that of FS1 (see third column in Fig. 5.1). The valley dose, which was expected to be of most significance concerning tissue repair, was 20.6 Gy in total for both fractionation schemes. As a result, the tissue reaction was much stronger for FS2 and FS3 than for FS1. However, the normal tissue responses (i.e. ear thickness and skin response score) differed significantly between FS2 and FS3, indicating that the detailed timing of dosages for the spatially fractionated dose distributions was critical for the severity of skin toxicities. The daily minibeam array in FS2 ($PVDR \sim 10{,}000$) led to intermediate ear thickening, whereas the daily minibeam array in FS3 ($PVDR = 15.2$) produced the greatest increase in ear thickness in this experiment. A possible explanation is that the negligible valley dose of a single fraction in FS2 (0.03 Gy) keeps valley tissue unharmed in that fraction. Some valleys remained at a low dose even up to the third fraction but received the valley dose of 20.6 Gy with the last fraction. Cells from the spared valleys of the previous fractions are able to migrate or proliferate and replace strongly affected cells of neighboring in-beam tissue. As a consequence, cells escape areas that are affected in a later fraction. Thus, the fraction of surviving cells remained larger in FS2 than in FS3, where such replacement mechanisms were hampered by the high valley doses of 5.2 Gy in each fraction.

Regarding late effects, our results showed markedly thicker ears in FS3 on day 153 and intermediate swelling FS2 ears; FS1 ears, in contrast, returned to the same thickness as sham ears. The ear thickness measurement (Fig. 5.3) correlated well with the skin response scoring (Fig. 5.2), supporting the finding that inflammation and fibrosis were the main contributors to chronic ear thickening [125]. Acute ear thickening re-

sulted from the highly pronounced erythema in FS3 ears, a cardinal symptom of acute inflammatory reactions [117]. With respect to late side effects, there was no difference in total FCT in the pinnae of control, sham, and FS1 ears on day 153. The total FCT content was significantly increased in FS3 ears (Fig. 5.5), contributing to the measured increase in ear thickness. In addition, the severity of inflammation (i.e. number of extravascular neutrophils and mononuclear infiltrating cells), and edema was still significantly increased after 153 days for FS2 and FS3 compared with control, sham, and FS1, indicating chronic inflammation.

The high peak doses of the spatially fractionated irradiation schemes seem to play only a minor role in tissue reactions. In the beam size study in chapter 4, high peak doses did not influence the overall skin responses adversely, but were mentioned to potentially influence the temporal dynamics of the reactions [118]. A similar observation was found in the data of fractionated minibeams. The reaction for FS1 started earlier supporting the observation of the beam size study that the higher the applied peak dose the earlier the radiation response. There was only a trend of an earlier time shift for FS2 in comparison to FS3, which might be caused by the differing daily dose distribution with a higher peak dose for FS2 than for FS3. The higher peak doses might cause differences in the induced cell death pathways, which potentially did affect the temporal dynamics of the overall reaction. Further investigations need to be elaborated accordingly to enable a solid clarification. Besides the temporal shift, a high dose modulation reduced the radiation response because a low valley dose is the major determinant for tissue-sparing. In the present study, the lowest peak dose of 78.6 Gy per fraction and the highest valley dose of 5.2 Gy were in FS3, which showed the strongest reactions in both acute and late skin toxicities. The highest peak dose of 314 Gy and the negligibly low valley dose in FS1 and FS2 resulted in lower side effects compared with FS3. Altogether, the normal tissue responses seemed to be more dependent on the dose coverage of the whole irradiated tissue rather than the peak dose, supporting our focus on dose modulation and the corresponding minimum doses in the valley.

The comparison of FS1, FS2, and FS3 showed that a high dose modulation in each fraction (FS1 and FS2) is preferred to a low dose modulation in each fraction (FS3), even if the different fractions do not hit the same positions, such as in FS2. Although the best tissue-sparing capabilities were attributed to a high total dose modulation as in FS1, side effects were still strongly reduced even if the daily fractions of high-dose modulations were shifted to obtain the lowest possible total dose modulation. In a realistic temporal fractionation of a minibeam treatment without accurate repositioning between fractions, the positions may be randomly distributed. Thus, a tissue response

between FS1 and FS2, which both result in reduced side effects compared with low dose-modulated daily irradiation (FS3) and most likely compared with conventional broad-beam irradiation, is expected. Radiation response is reduced because valleys remain at a low dose by chance throughout the whole dose application. The probability that large areas remain at a low dose, which is important for efficient tissue repair, increases for lower σ/ctc ratios and fewer temporal fractions. Hypofractionation may be favored with regard to an optimized use of spatial fractionation by pMBRT.

5.4 Conclusion

Our study demonstrated for the first time the impact of daily and total dose modulations in radiotherapeutic regimes combining spatial and temporal fractionation. The best tissue-sparing was achieved after delivering a highly dose-modulated minibeam array to the same tissue spot in every fraction, maintaining a low valley dose. Using a daily minibeam pattern with high $PVDR$ and very low valley dose was more advantageous, even if shifted between fractions, than daily accurate delivery of a minibeam array with lower $PVDR$ and higher valley doses. In summary, the best tissue-sparing in fractionated proton minibeams was achieved when the tissue was accurately repositioned and proton minibeams with high $PVDR$ and very low valley dose were used. However, randomly applied proton minibeam fields with a small number of temporal fractions led to a considerable reduction of side effects.

Chapter 6

Proton minibeam therapy with interlacing and heterogeneous tumor dose

The content in this chapter has already been published. Several sections, which are adapted and minorly corrected for this thesis, are mainly reprinted with permission from:
Sammer, M. *et al.* Optimizing proton minibeam radiotherapy by interlacing and heterogeneous tumor dose on the basis of calculated clonogenic cell survival.
Scientific Reports, **11.1** (2021) 1-16.

The beam size study presented in chapter 4 showed clear evidence for tissue-sparing in proton minibeam radiotherapy. However, the results also depicted that with increasing depth and increasing σ/ctc, the sparing potential is reduced. This is particularly problematic at the tumor vicinity, since the dose modulations are already close to a homogeneous dose distribution such as in the conventional irradiation. A first theoretical study concerning unidirectional (1-dir) proton minibeams (see Fig. 6.1a and 6.1c) assessed dose distributions on the basis of a calculated clonogenic cell survival [99] and confirmed the observed results of chapter 4.

A 5 cm thick tumor with its proximal edge at 10 cm depth was chosen as a model to be irradiated with protons in either broadbeam configuration or with spatially fractionated minibeams of various shapes. The tumor dose in the former study was kept homogeneous according to the ICRU reports [97, 98]. Large sparing of healthy tissue due to strongly enhanced mean cell survival compared to homogeneous irradiation was achieved in the first centimeters below the skin. However, relative tissue-sparing decreased with depth due to the small-angle scattering of the minibeams. After about

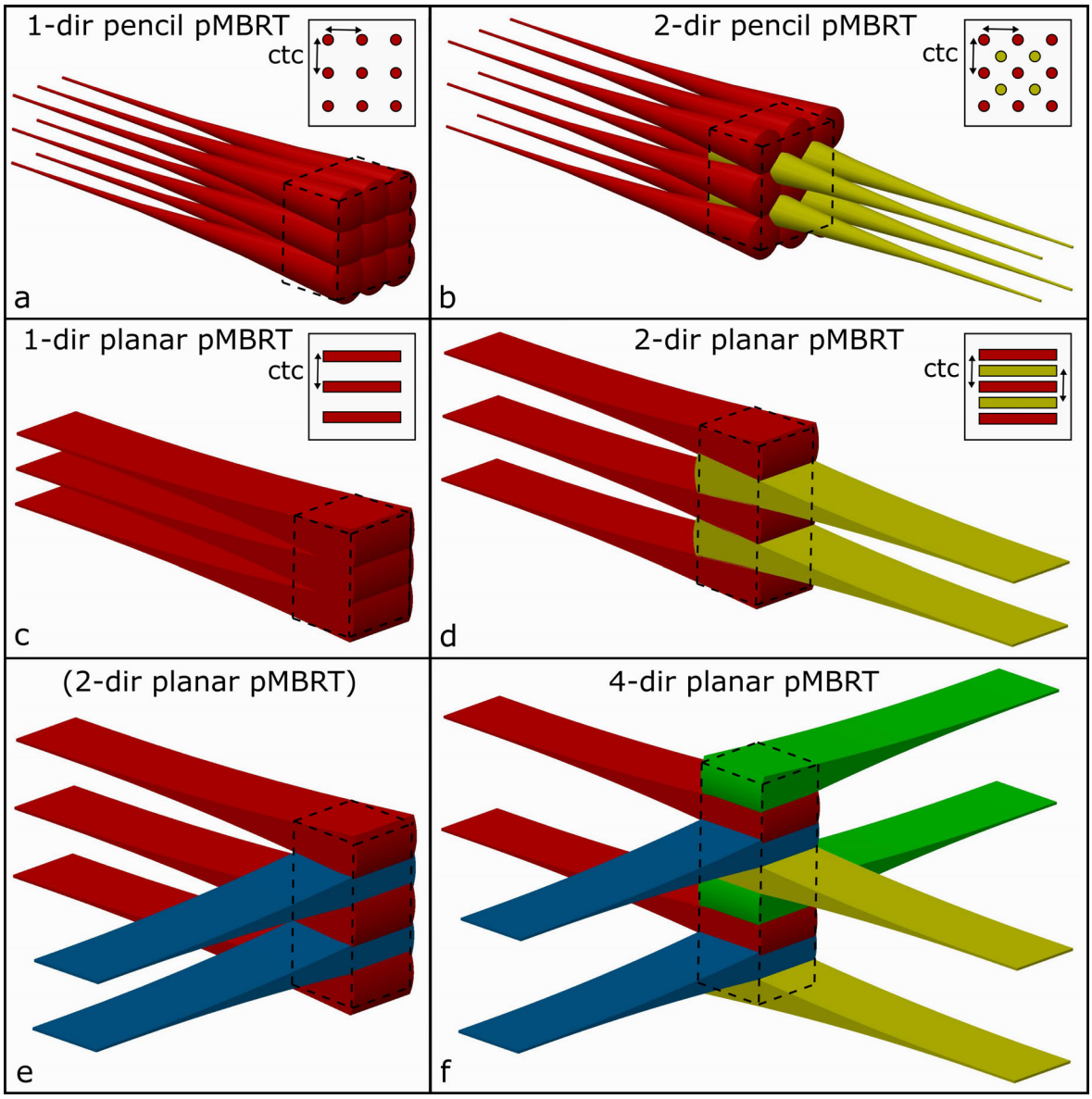

Figure 6.1: *Schematic representation of unidirectional proton minibeams and interlaced minibeams from multiple directions. Unidirectional minibeams can be applied with pencil (a) or planar (c) minibeams. Pencil minibeams are interlaced from two opposite directions (b) with the two grids shifted by (ctc/2, ctc/2). Planar minibeams are interlaced from two opposing (d) and two orthogonal (e) directions with the two grids shifted by (ctc/2). Planar minibeams are also interlaced from four directions (f; 90° between all neighboring directions, grids shifted by ctc/4 between neighboring directions). Figures are created using the Creo 2.0 software. Credit: Peter Hartung.*

7 cm of depth, cell survival was not substantially enhanced for proton minibeams compared to conventional proton irradiation. Hence, the close vicinity of the tumor did not benefit from spatial fractionation by 1-dir proton minibeam irradiation when a homogeneous tumor dose was considered. Besides, tissues in the close tumor surrounding are particularly critical since they receive similarly high doses as the tumor.

In order to improve tissue-sparing towards the close surroundings of the tumor, σ/ctc ratios need to be decreased by reducing beam sizes or increasing ctc distances. Beam diameters depend on initial beam size and depth in tissue and are thus not easily changed for a given tumor scenario. In this in-silico study, the options for increasing ctc distances by interlacing (also interleaving, cross-firing) beams from two or more directions were studied. The minibeam arrays of several directions were adjusted such that the dose maxima of the minibeams from one direction are positioned in the dose minima of the minibeams from the other direction [27, 136, 137]. Pencil and planar minibeams were interlaced from two opposing directions (2-dir, Figs. 6.1b, 6.1d), leading to substantial tissue-sparing only for particles due to their finite range, which is not the case for photons. As an additional possibility, planar beams were interlaced from four directions (4-dir, here with 90° angles between neighboring directions) (Fig. 6.1f). The neighboring directions are not necessarily orthogonal but angles $< 90°$ lead to overlap in the healthy tissue in front of the tumor. This is the first time a real interlacing from four directions is presented, where every fourth minibeam within the tumor comes from one side. Suggestions to interlace from four directions have already been described by Dilmanian et al. [27] or Henry et al. [136, 138], but both approaches superpose two (perpendicular) directions and only interlace the opposing two directions reducing the interlacing potential to that of two-directional interlacing (shown for comparison in section 6.5 Figs. 6.9 and 6.9). For the sake of completeness, the interlacing of two orthogonal directions is also presented (Fig. 6.1e) but was not considered in the actual dose calculation because of its similarity to the interlacing of two opposing directions.

For all cases, heterogeneous tumor irradiations were compared to homogeneous tumor doses to show their potential for enhanced sparing of the healthy tissue at the tumor edge by spatial fractionation. The upper dose constraint for prescribed doses as given by the ICRU reports [97, 98] was waived, but the low dose limit within the tumor [139] was kept for sufficient treatment dose covering the whole tumor. All dose calculations were assessed by a calculated mean clonogenic cell survival in view of sparing normal tissue from side effects as in the mentioned study of Sammer et al. [99].

Interlaced proton minibeam irradiations require much larger technical effort to adjust the minibeams from different directions with the necessary precision in terms

of positioning and beam directions relative to their dose modulations in the tissue. Moving organs (tumors) are also an issue for interlaced proton minibeam irradiations. Dependent on tumor size, depth inside the body, and robustness of the dose planning against variations, submillimeter to even 0.1 mm beam adjustments may be required within the tumor. This technical effort will only be considered when a clear advantage of interlaced compared to unidirectional proton minibeam irradiation modes is obvious. The presented study intended to show whether and under which conditions a substantial increase in tissue-sparing potential is achieved from interlaced proton minibeams applied to an idealistic tumor. Technical solutions to obtain all beam requirements for interlaced proton minibeam irradiations may be established from the results presented here.

6.1 Material and Methods

The dose distributions of proton minibeams were approximated by Gaussian distributions resulting from the lateral spread through small-angle Multiple Coulomb Scattering (MCS) of the protons. Data for the lateral spread of protons in water were taken from the database LAP-CERR [140, 141], which is based on Monte-Carlo simulated dose distributions that were fitted by either a single Gaussian distribution or a sum of two Gaussian distributions. Minibeams were assumed to be produced by focusing through an ion lens excluding the generation of secondary particles from collimation. Divergence of the proton beams was also assumed to be less than the spread through MCS of the beam within the body and was neglected for the dose simulations.

Planar minibeams and quadratically arranged round pencil minibeams were considered. For the planar case, 17 minibeams were calculated while 16×16 minibeams were calculated for the pencil beam arrangements. The resulting unit cell at the center of the pattern delivered the representative dose distribution for each pattern. The numerical accuracy of the centered unit cell was $< 8 \times 10^{-6}\, D_{mean}$, where D_{mean} is the mean dose. The broadbeam scenario was assumed as laterally homogeneous. The binning for the dose calculations was $0.01\,\text{mm} \times 0.01\,\text{mm}$ for each pixel.

The considered scenario was a tumor with its proximal edge located in 10 cm depth and a thickness of 5 cm as used in [99]. For irradiation from several directions, the 5 cm thick tumor was located at the center of a symmetrical 25 cm thick phantom, i.e. at 10 cm depth from each direction.

A spread-out Bragg peak (SOBP) was assumed to homogeneously cover the tumor in the longitudinal direction. The required fractions of protons of different energies were taken from the study of Sammer et al. [99] obtaining a dose fluctuation of

$|D_{SOBP}/D_0| < 1.0\,\%$ within the target volume. The same fractions of particle energies, but laterally rearranged, were used for the minibeam calculations. Hence, the SOBP curve was the depth dose distribution for the broadbeam irradiation and delivered the mean dose of the minibeam irradiation at each depth.

Lateral dose distributions approximated by a single Gaussian were taken from the database LAP-CERR [140, 141] for depths between 10 and 157 mm. To get a better representation of the lateral dose distribution in particular in the valleys between the minibeams close to the tumor edges, a two-Gaussian representation was chosen and also taken from the LAP-CERR database. The two-Gaussian representation for lateral dose distributions of protons delivered more appropriate data than the one-Gaussian model at depths larger 4 cm, where large-angle scattering contributions start to increase [142]. The initial beam size at the patient was assumed as a pure Gaussian with $\sigma_0 = 0.2\,\text{mm}$ (standard deviation). The *ctc* distances were optimized dependent on minibeam shape, number of beam directions, and dose heterogeneity in the tumor volume. The scattering outside the restricted tumor volume (5 cm) was neglected for the one-Gaussian approximation since it only has a minor influence on the overall dose distribution, but was integrated for the two-Gaussian approximation.

Every calculated dose map $D(x, y)$ was converted into a calculated clonogenic cell survival (hereafter referred to only as cell survival for simplified reading) $S(x, y)$ by the Linear-Quadratic model [143] given as

$$S(x, y) = \exp(-\alpha D(x, y) - \beta D^2(x, y)). \tag{6.1}$$

The α and β values are $\alpha = 0.425\,\text{Gy}^{-1}$ and $\beta = 0.048\,\text{Gy}{-2}$, i.e. $\alpha/\beta = 8.9\,\text{Gy}$ being a mean value of the PIDE database [68, 99] for human cells, including both tumor and healthy tissue cells. The Linear-Quadratic model (LQ-model) has limitations for high doses (i.e. $> 10\,\text{Gy}$). Experimental data shows a rather constant decrease in the logarithmic displayed cell survival curves for high doses, whereas the LQ-model curve bends with increasing dose, overestimating the cell killing. The linear continuation is included in a number of different cell survival models such as the Kavanagh-Newman [144], Two components [145], Linear-Quadratic-Linear model (LQL-model) [146] and others [147–152]. The linear continuation for high doses can, however, not be generalized since the exact cell survival curve and also the appropriateness of a model depends on the cell type [153]. In addition, most advanced survival models include a further parameter, which is often unavailable in a database like PIDE. In spatial fractionation, where dose modulations need to be translated into a cell survival, an advanced model like the LQL-model may be slightly more accurate when describing the absolute clonogenic cell survival, but e.g. the maximum differences between the LQ-model and the LQL-model and their mean cell survival was found to be of < 0.04 percentage points in our previ-

ous minibeam study [99]. These small differences are based on the overall small cell survival results (for most cells $\ll 1\,\%$) found for doses higher than 10 Gy. The peak doses in proton minibeam therapy can be up to several hundred Gy resulting in a minor contribution to cell survival independent on the used model. Calculating the mean cell survival within a unit cell on a percentage scale is therefore independent of the accuracy of the model within the high dose regions. Increased clonogenic cell survival results mainly from the low doses (< 10 Gy) in the valleys where the cell survival is high on a percentage scale and accurately described by the LQ-model as also proposed by Guardiola et al. [154]. It needs to be mentioned, that the calculated clonogenic cell survival based on the LQ-model was used as a simple biologically weighted measure for spatially fractionated dose distributions, but precise biological consequences cannot be withdrawn from the data (more details are found in the discussion).

Non-targeted effects were not included in the calculations since they are diversely discussed [155–157] and commonly accepted models to describe changes of cell survival due to lateral dose modulations are missing. In addition, they were attributed to "play a negligible role for low-LET particles" [156, 157].

Dose-dependent and energy-dependent *RBE* of protons was not included in our calculations. *RBE* enhancements were reported to occur in dose valleys for collimated beams [158]. Similar enhancements, however, were not yet reported for focused beams where a much lower portion of protons is stopped in front of the Bragg peak. Thus, lateral changes in the *RBE* were not included in the calculations presented here.

The clonogenic cell survival for 2, 10, and 35 Gy homogeneous tumor dose was calculated for each irradiation scenario. In the case of heterogeneous dose distributions in the tumor, the same doses as assumed in the homogeneous case were set as minimum doses to be at least obtained at each location in the tumor. It should be noted that although high doses were assumed within the tumor, no absolute tumor control probabilities were modeled and all conclusions drawn for tumor control were only based on relative assessments.

6.2 Results

6.2.1 Irradiation with homogeneous tumor dose

Longitudinal cross-sections of dose distributions are plotted in Fig. 6.2a as an example for planar minibeams that are interlaced from two opposite directions (cf. Fig. 6.1d). The *ctc* distance between the minibeams was maximized under the constraint of homogeneous tumor dose: any location within the tumor phantom received at least 97.5 %

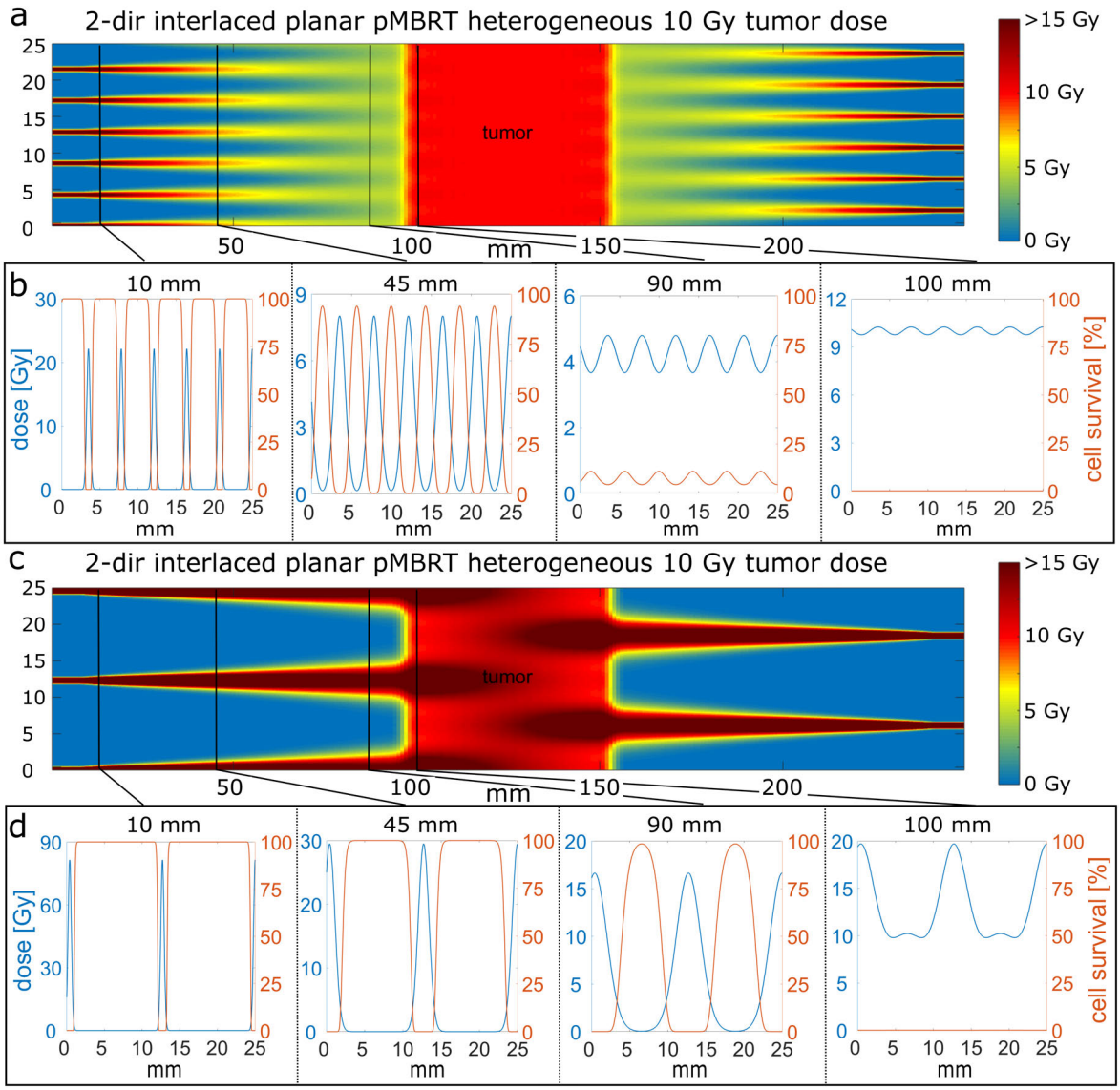

Figure 6.2: *Dose maps of 2-dir interlaced planar minibeams (cf. Fig. 6.1c) with homogeneous (a) and heterogeneous (c) tumor dose. The dose is color-coded with saturation at 15 Gy. The cross-section of dose and the local clonogenic cell survival at 10, 45, 90, and 100 mm depth are shown for homogeneous (b) and heterogeneous (d) tumor irradiation with 10 Gy mean or minimum tumor dose, respectively. Heterogeneous tumor irradiation is described in section 6.2.2.*

but less than 103.5 % of the prescribed tumor dose. These values were taken as a save range to fulfill the dosage criterion of the ICRU ($95\,\% < D_t < 107\,\%$) even under small uncertainties of dose calculations or applications. Fig. 6.2a represents the dose profiles for a prescribed tumor dose of 10 Gy but can be linearly scaled to any other tumor dose.

One-dimensional cross-sections of the dose profiles (blue lines) and the corresponding local clonogenic cell survival (red lines) are plotted in Fig. 6.2b at depths marked in Fig. 6.2a. Close to the skin at 10 mm depth, the cell survival within the minibeams was negligible while in between, a plateau of nearly 100 % cell survival was reached. The modulation of cell survival steadily decreased until a low oscillation and low overall cell survival was obtained close to the tumor.

A major factor for the integrity and repair capacity of irradiated normal tissue is the mean cell survival within that tissue. The depth-dependent, clonogenic mean cell survival was calculated for comparison of the different prescribed homogeneous tumor doses (2, 10, and 35 Gy) for the various irradiation schemes of the 2-dir and 4-dir interlacing geometries in Fig. 6.3 (full lines). Due to symmetry, the cell survival curves along only one irradiated direction are plotted up to the proximal tumor edge. For comparison, mean cell survival for superposed 1-dir minibeam irradiations (dotted lines "sp", Fig. 6.3) and broadbeam irradiations (black lines) were calculated. Superposed 1-dir minibeam irradiations led independently to the homogeneous irradiation of the tumor for each of the opposing or orthogonal directions (cf. Fig. 6.1a or c), with half or a quarter of the prescribed dose delivered from each direction for 2-dir or 4-dir, respectively. Summed up, the prescribed tumor doses were achieved as for the interlaced minibeam cases.

The cell survival curves for all minibeam irradiation cases showed very high cell survival in the superficial layers. The interlaced pencil beams from two opposing directions (full red lines in Fig. 6.3) resulted in the highest cell survival of above 80 % at 1 cm below the skin (9 cm in front of the tumor). Caused by the pure geometrical sparing, the cell survival in the entrance barely changed with the prescribed tumor dose. Even for a tumor dose of 35 Gy a mean cell survival greater 80 % was obtained. With increasing depth, the cell survival curves of the minibeam irradiations approached the broadbeam survival levels (black lines in Fig. 6.3) until they eventually merged at 2 cm tumor distance. Hence, interlacing minibeams from multiple directions (full lines in Fig. 6.3) offered only a slight advantage compared to non-interlaced, superposed 1-dir minibeams (dotted line in Fig. 6.3), which are much easier to implement technically. The main cause is that the beams scatter within the tumor volume and the dose modulation decreased to the end of the irradiation range. At each tumor edge, the incoming beam had a high dose modulation, whereas the beam from the opposite direction that already passed the tumor had a lower dose modulation. The beam with lower dose modulation could hardly compensate for the high dose modulation of the beam entering the tumor. In combination with the strong homogeneity requirements within the tumor, *ctc* distances could not substantially be increased compared to the

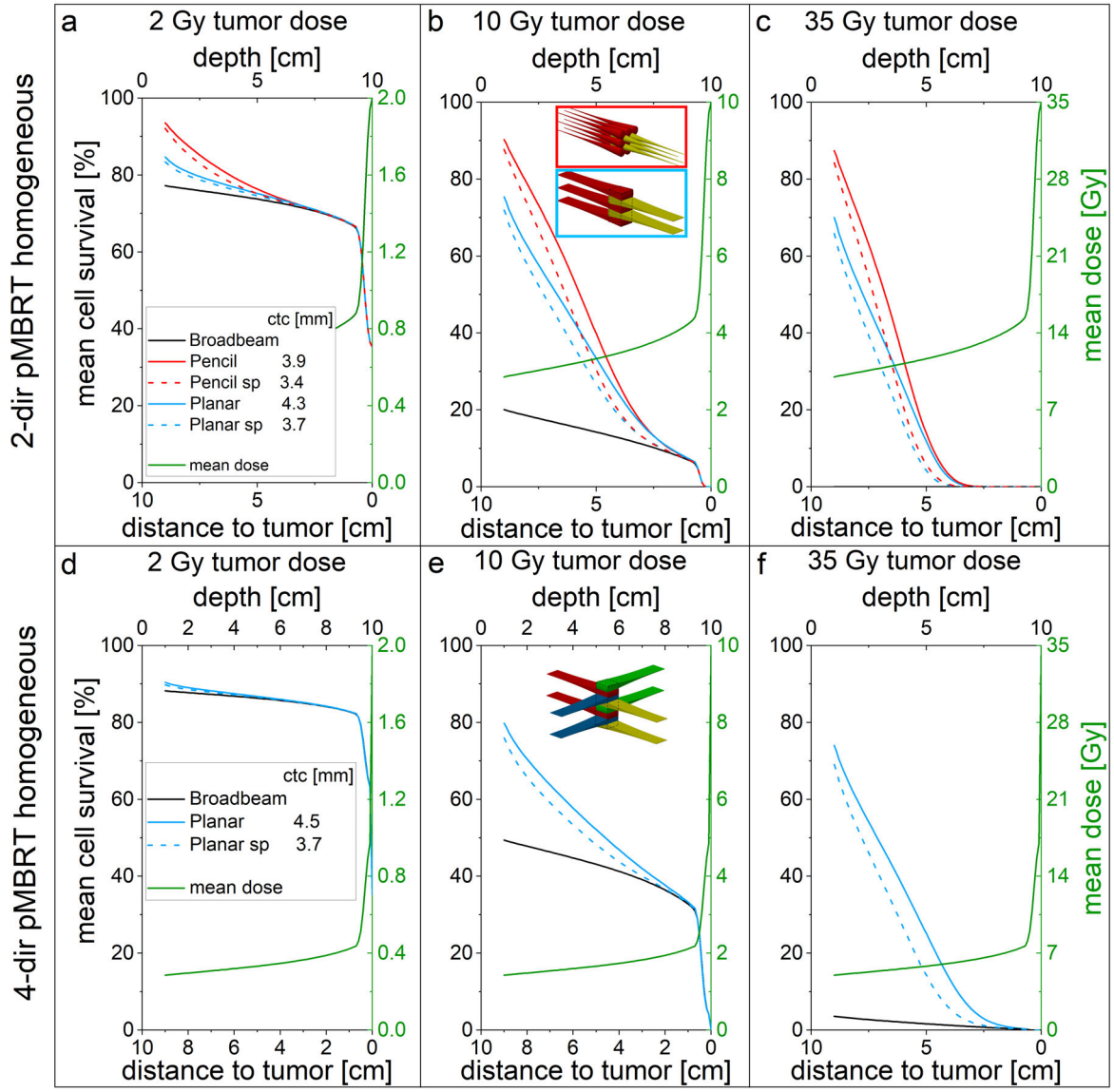

Figure 6.3: *Mean cell survival for homogeneous tumor irradiation from two opposing directions (a - c) and four orthogonal directions (d - f). The tumor dose was set to 2 (a, d), 10 (b, e) or 35 Gy (c, f). "sp" is short for superposed and labels the irradiation by minibeams delivering a homogeneous tumor dose from each direction with half (2-dir) or quarter (4-dir) of the tumor dose delivered from each direction summing up to the prescribed tumor dose. The mean dose D_{mean}, which is the same for all irradiation modalities for homogeneous tumor irradiation, is added to each figure in green and corresponds to the y-axis on the right.*

unidirectional case. Interlaced irradiations in a thinner tumor scenario did compensate the dose modulations within the tumor volume better, but could also not offer a substantial sparing at the close tumor surrounding. More detailed information is offered in section 6.5.3.

The 2 Gy irradiations barely benefited from spatial fractionation since low doses reach also high survival even for a broadbeam irradiation. For higher doses, the difference between the survival curves was more pronounced caused by the pure geometrical sparing from minibeam irradiation.

6.2.2 Irradiation with heterogeneous tumor dose

To evaluate the tissue-sparing potential by minibeam irradiation modes inducing a heterogeneous tumor irradiation, dose maps were calculated and the sparing potential was evaluated by the depth-dependent mean cell survival. An example of an optimized dose map for heterogeneous tumor irradiation by interlaced proton minibeams from two opposing directions is shown in Fig. 6.2c. The minimum dose within the tumor was set to 10 Gy, as it was the prescribed dose in the homogeneous case of Fig. 6.2a, but a dose modulation to larger doses was accepted. Thus, for heterogeneous dose profiles, the mean dose covering the tumor was increased by a factor $f_D > 1$ compared to the homogeneous case ($f_D = 1$) to obtain the same minimum dose as required. In Fig. 6.2c, the mean tumor dose was increased to 12.9 Gy, being a factor $f_D = 1.29$ higher than the 10 Gy homogeneous dose of Fig. 6.2a. It resulted in dose maxima of 20 Gy when the *ctc* distance of the minibeams was maximized under these conditions to $ctc = 12.3$ mm. Thus, the *ctc* is 2.9 times larger than the *ctc* for the homogeneous case ($ctc = 4.3$ mm). The large *ctc* distances resulted in low dose levels within the dose valleys at all distances up to the close tumor surrounding. Thus, high local cell survival was maintained up to 10 mm in front of the tumor (Fig. 6.2d) with a high potential of reduced side effects.

The depth-dependent peak-to-valley dose ratio $PVDR$ and the mean dose D_{mean} was calculated for the various proton minibeam irradiation modes and is plotted in Fig. 6.4. The mean doses are given relative to a prescribed minimum tumor dose.

The large $PVDR > 100$ at superficial layers (large distances to the tumor) was given by the assumed small initial beam size ($\sigma_0 = 0.2$ mm) that will depend, however, on the technical conditions of a future proton minibeam irradiation facility. In any case, beam sizes and beam divergences were small at the superficial layers, beam sizes deeper in the body were mainly determined by the physical processes of small-angle multiple scattering as it is represented by the calculated $PVDR$ in Fig. 6.4. The $PVDR$ ratios only depended on the depth inside the body and the *ctc* distances. The *ctc* values

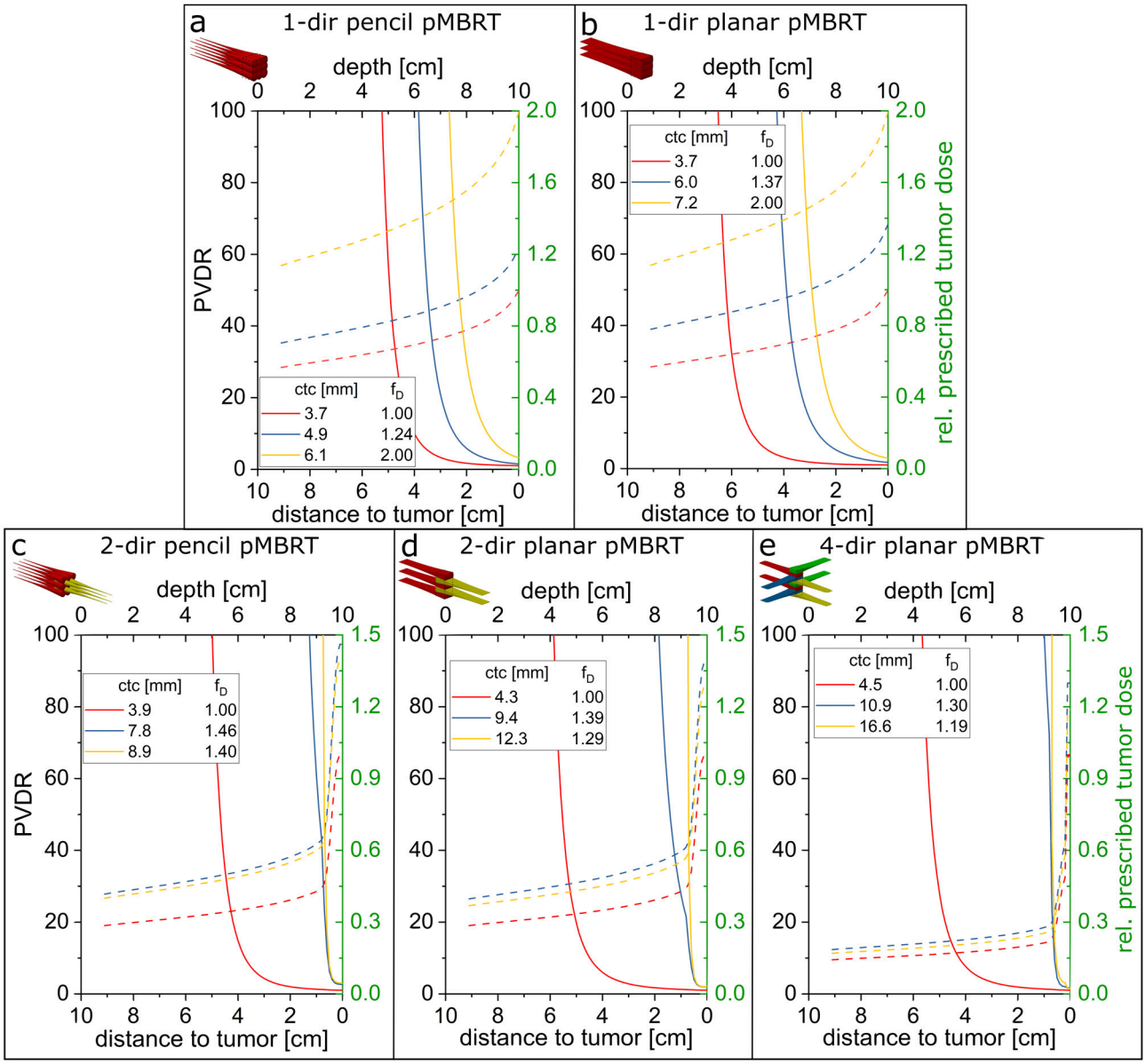

Figure 6.4: *PVDR (full lines, left y-axis) and mean dose (dashed lines, right y-axis) for the heterogeneous (blue and yellow) vs. homogeneous (red) irradiation with planar (a) or pencil (b) unidirectional, two opposite (2-dir, c and d), and four-directional (4-dir, e) minibeams. The mean dose varies due to the dose modulation differences to fulfill the minimum dose constraint within the tumor. The required f_D for different ctc are plotted in Fig. 6.7 as an example for 2-dir planar minibeams.*

could be adjusted to obtain large $PVDR$ in particular at the close tumor vicinity but mean dose levels had to be raised by the factor f_D in order to fulfill the minimum dose criterion within the tumor.

For biological assessment, the depth-dependent mean cell survival is plotted in Fig. 6.5 for various irradiation scenarios of heterogeneous dose distributions in the 5 cm thick tumor and a minimum tumor dose constraint of 10 Gy. The mean cell survival of 1-dir pencil and planar proton minibeam irradiations is shown in Fig. 6.5a and Fig. 6.5b, respectively. The mean dose D_{mean} in the tumor was set to $D_{mean} = f_D \cdot 10\,\mathrm{Gy}$ as marked in the figures. Mean cell survival was larger for heterogeneous tumor irradiation of larger *ctc* distances but larger mean tumor doses ($f_D > 1$) compared to homogeneous irradiation ($f_D = 1$) already for the 1-dir case. Pencil minibeams resulted in larger mean cell survival than planar beams. However, cell survival strongly decreased with depth for the 1-dir cases and merges with a broadbeam irradiation scenario (black line in Fig. 6.5a, b) some centimeters before the tumor edge.

A strong increase in cell survival close to the tumor edge was achieved when 2-dir or 4-dir interlaced minibeams were applied with heterogeneous tumor irradiation. Mean cell survival for 2-dir, interlaced pencil and planar minibeam scenarios was presented for a 10 Gy minimum tumor dose in Figs. 6.5c and d. 4-dir interlaced (orthogonal) minibeam irradiation cases are plotted in Fig. 6.5e. Mean cell survival of the homogeneous cases ($f_D = 1$, red lines in Fig. 6.5) merge with the broadbeam irradiations (black lines in Fig. 6.5) 2 – 3 cm before the tumor edges. The heterogeneous cases showed high levels of mean cell survival up to the close tumor vicinity. The steep slopes of the cell survival resulted from the distal sides of the SOBP arriving from the opposite direction at that tumor edge. Although the pencil minibeam arrangements led to higher mean cell survival rates for homogeneous tumor irradiation in the 2-dir case, the interlaced minibeams with heterogeneous tumor dose showed higher mean cell survival close to the tumor edge for planar minibeams. Altogether, heterogeneous dose distributions in the tumor are favored due to high mean cell survival within the healthy tissue in particular close to the tumor.

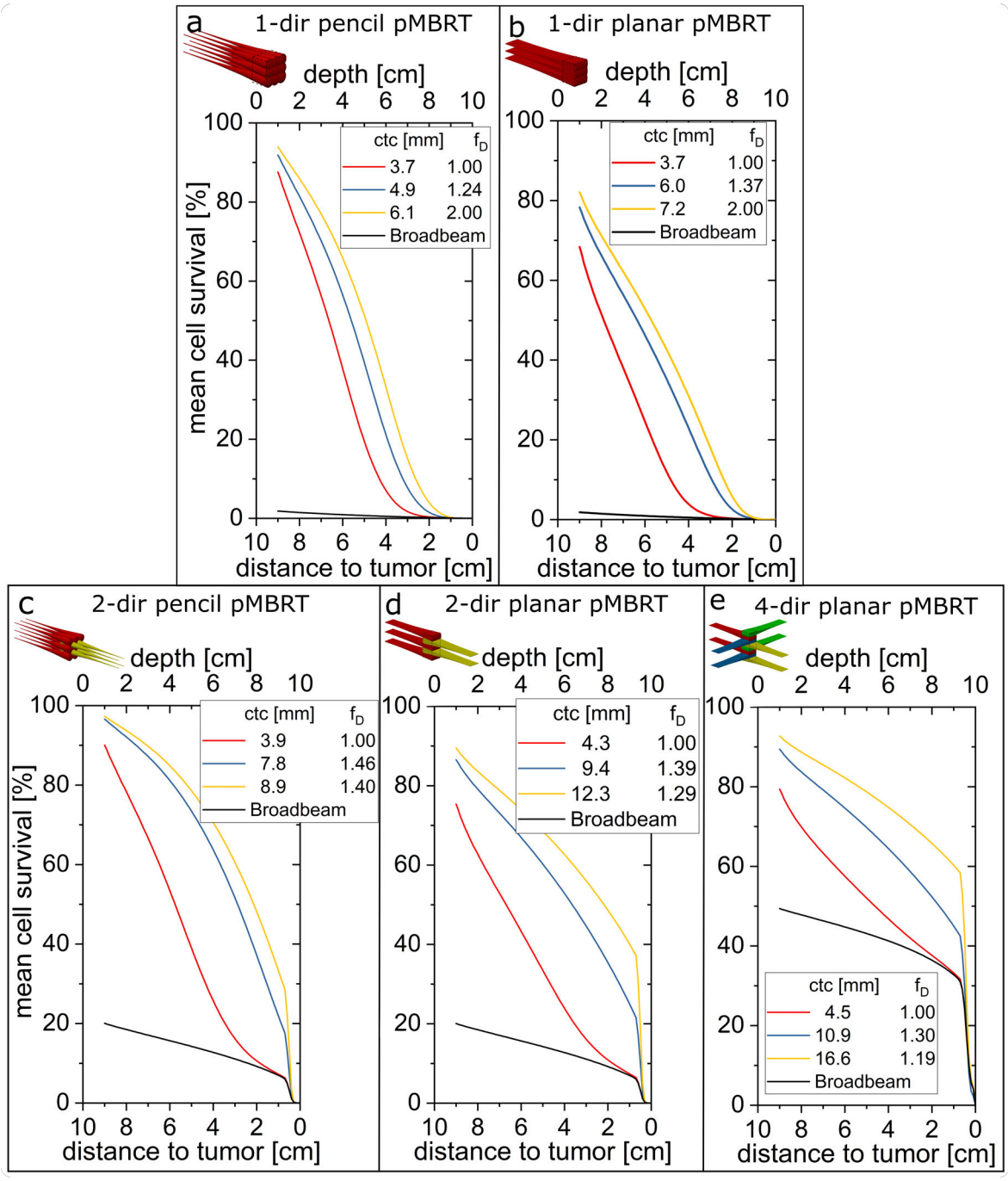

Figure 6.5: *Mean cell survival results for the heterogeneous vs. homogeneous irradiation with planar (a) or pencil (b) minibeams from one direction, two opposite (2-dir, c and d) and four directions (4-dir, e). A minimum dose of 10 Gy within the tumor was applied.*

The simulations were extended using a more detailed representation of the lateral spread approximated by a two-Gaussian lateral dose distribution of the proton minibeams. It resulted in more reliable cell survival data for the dose valleys close to the tumor. The *ctc* and the respective enhancement factors f_D were optimized for heterogeneous tumor irradiation modes and compared to broadbeam and homogeneous minibeam irradiation modes for 10 Gy and 35 Gy minimum tumor doses in Fig. 6.6. Optimized mean cell survival at the tumor edges were found from the calculated mean cell survival.

The resulting optimum *ctc* distances and mean cell survival levels are reported in Table 6.1. An optimum distance of $ctc = 15$ mm with $f_D = 1.5$ was obtained for 2-dir interlaced planar minibeams. A $ctc = 20.4$ mm with $f_D = 1.21$ was the optimum in the case of the four-directional proton minibeam irradiations. The high minimum tumor dose of $D_{min} = 35$ Gy led to a drop in cell survival compared to the $D_{min} = 10$ Gy minimum tumor dose. However, there was still a substantial mean cell survival even at a high single dose fraction of 35 Gy.

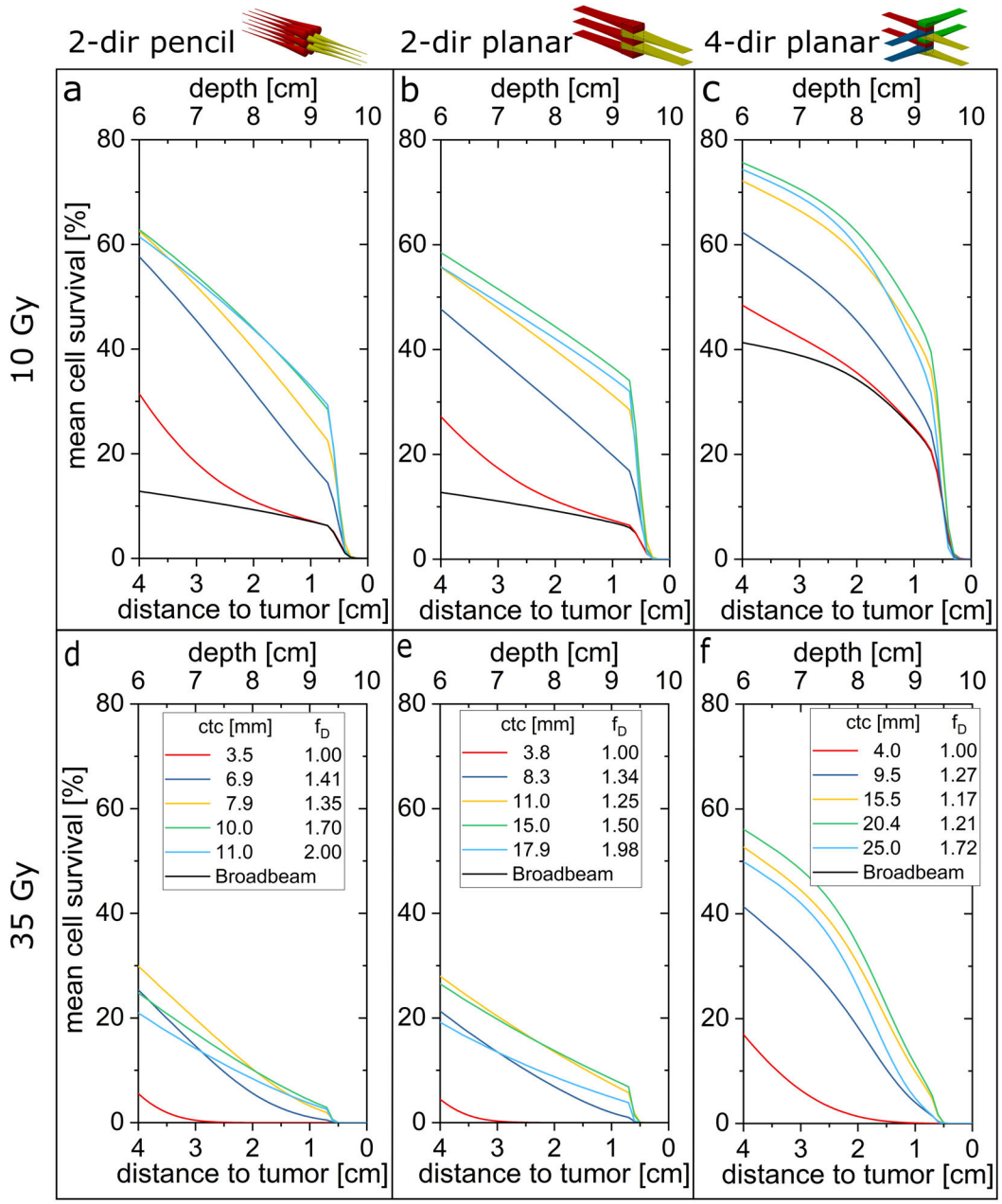

Figure 6.6: *Mean cell survival results for the heterogeneous vs. homogeneous irradiation with 2-dir pencil (a,d) or planar (b,e) minibeams as well as 4-dir planar minibeams (c,f) at the close vicinity of the tumor using the two-Gaussian model from LAP-CERR [140, 141]. The high doses of 10 Gy and 35 Gy minimum dose are presented in the upper row (a - c) and lower row (d - f), respectively. The cell survival for 35 Gy broadbeam irradiation is equal to 0 for all depths.*

Minibeam mode	*ctc* [mm]	f_D	$D_{min} = 10\,\mathrm{Gy}$						$D_{min} = 35\,\mathrm{Gy}$				
			1 cm			9 cm			1 cm			9 cm	
			S [%]	$d_{eff,10\,\%}$ [mm]	$d_{eff,50\,\%}$ [mm]	S [%]	$d_{eff,10\,\%}$ [mm]	$d_{eff,50\,\%}$ [mm]	S [%]	$d_{eff,10\,\%}$ [mm]	$d_{eff,50\,\%}$ [mm]	S [%]	$d_{eff,10\,\%}$ [mm]
2-dir Broadbeam	-	1.00	20	-	-	7	-	-	∼0	-	-	∼0	-
4-dir Broadbeam	-	1.00	50	-	-	25	-	-	4	-	-	∼0	-
2-dir pencil hom	3.5	1.00	87	1.1	1.3	7	-	-	84	1.3	1.5	∼0	-
2-dir planar hom	3.8	1.00	73	0.7	0.9	7	-	-	67	0.9	1.1	∼0	-
4-dir planar hom	4.0	1.00	78	0.7	0.9	25	-	-	71	0.9	1.1	∼0	-
2-dir pencil hetero (opt)	10.0	1.70	98	1.4	1.5	32	6.7	8.6	97	1.6	1.7	4	9.8
2-dir planar hetero (opt)	15.0	1.50	91	1.0	1.1	37	5.7	7.7	90	1.3	1.4	8	8.5
4-dir planar hetero (opt)	20.4	1.21	94	0.9	1.1	47	4.7	7.1	93	1.1	1.3	11	8.1

Table 6.1: *Comparison of different interlacing minibeam modes with two-Gaussian approximation. For each minibeam mode, the homogeneous tumor irradiation and the optimum heterogeneous tumor irradiation is presented. The mean cell survival (S) and biologically effective beam size (d_{eff}) for $D_{min} = 10\,Gy$ and $D_{min} = 35\,Gy$ (minimum) tumor dose are given for 1 cm and 9 cm depth. The survival fractions of 10 % or 50 % are taken for determination of the effective beam sizes $d_{eff,10\,\%}$ and $d_{eff,50\,\%}$. Values marked by a dash (-) cannot be determined.*

The minimum dose of the heterogeneous irradiation was set equal to the mean dose of conventional irradiation approaches since it mainly qualifies the tumor control [159]. This led indispensably to an increase of the mean dose of heterogeneous irradiations by a factor f_D compared to the homogeneous irradiation. The dose enhancement factor f_D increased not monotonically with *ctc* distances. For 2-dir interlaced planar minibeams and two-Gaussian approximation, it had a local maximum at $ctc = 8.3\,\text{mm}$ ($f_D = 1.34$) and a local minimum at $ctc = 11\,\text{mm}$ ($f_D = 1.25$) as shown in Fig. 6.7.

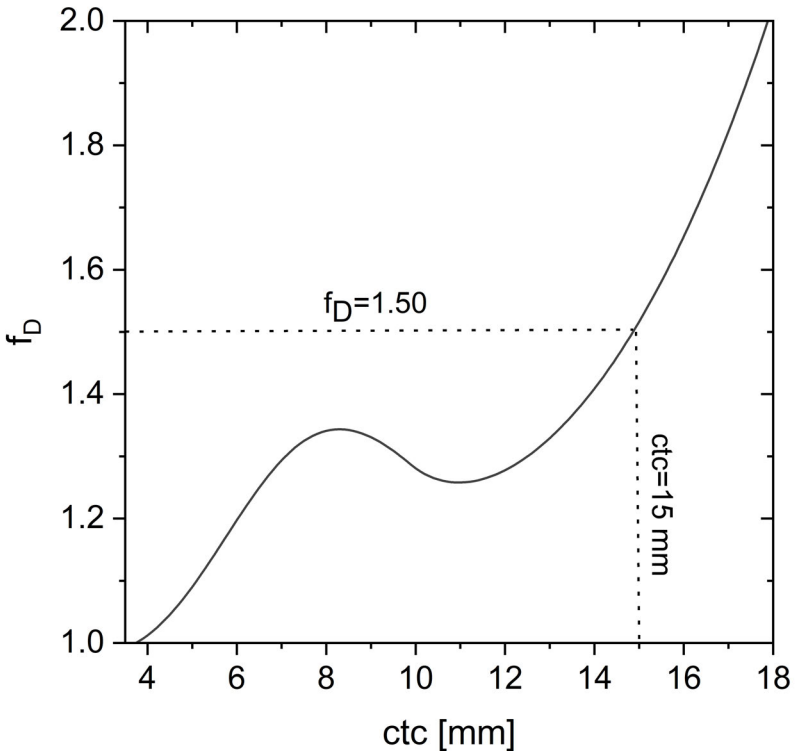

Figure 6.7: *Multiplication factor f_D over ctc required to fulfill the minimum criterion $D_min/D_t = 0.975$ for 2-dir interlaced planar minibeams. The beam shape was approximated with two Gaussians. The dotted lines mark the optimum found according to the calculated cell survival curves at the close tumor surrounding.*

Although the mean cell survival slightly increased further beyond the minimum, a *ctc* close to the minimum seems to be a good option for a robust proton minibeam irradiation. The local minimum is the compromise between large *ctc* for tissue-sparing but also a high minimum dose without an immense increase in the f_D factor. The *ctc* distances close to that minimum allow the robust tumor irradiation where minor variations of the *ctc* would barely change the dose coverage of the tumor.

6.2.3 Biologically effective minibeam sizes

When irradiating deep-lying tumors, initially small minibeams suffer from lateral spread through small-angle scattering. The minimum beam size given by the standard deviation σ of the minibeam dose profile depends on the type of ions (e.g. protons, helium or carbon ions), the beam energy and the depth within the tissue. The lateral dose profile as obtained at 9 cm depth applying 2-dir planar proton minibeams with 15 mm *ctc* and $f_D = 1.5$ to the considered tumor model is shown in Fig. 6.8. The calcu-

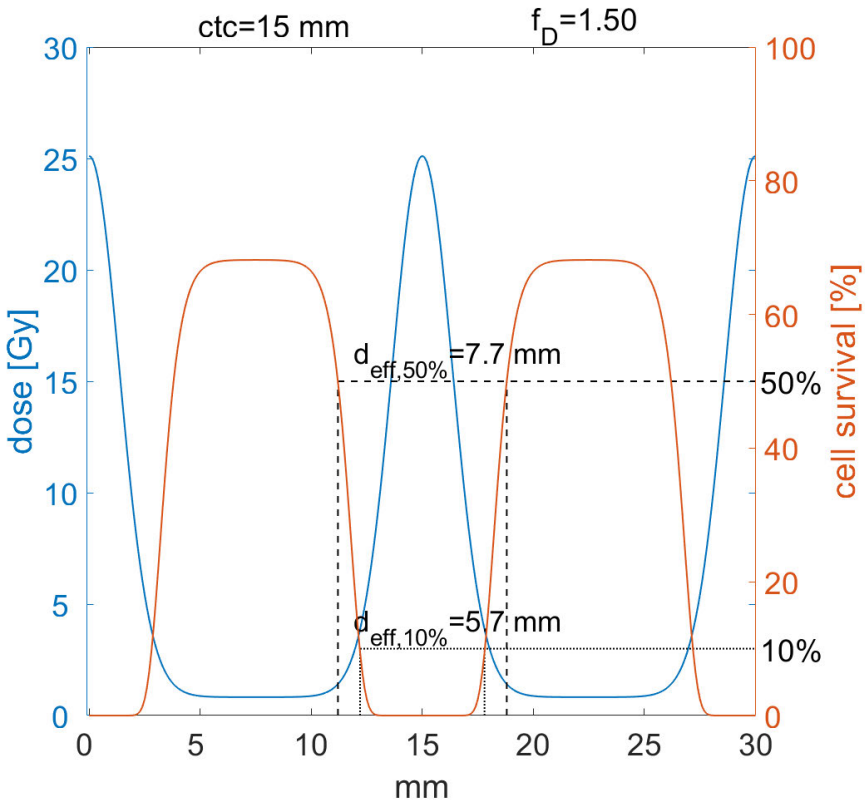

Figure 6.8: *Dose profile (blue) and cell survival profile (orange) for 2-dir planar minibeams with ctc = 15 mm at 9 cm depth (two-Gaussian approximation). The dotted lines mark the biologically effective beam size with a 10 % survival threshold ($d_{eff,10\,\%}$). The dashed lines mark the biologically effective beam size with a 50 % survival threshold ($d_{eff,50\,\%}$). A ctc of 15 mm was found to deliver an optimum mean cell survival even though the mean dose has to be increased by the factor $f_D = 1.50$.*

lation was performed using the two-Gaussian approach for the lateral dose profiles. To quantify the size of the minibeam, where most cells have radiation-induced damages, the biologically effective minibeam size d_{eff} was introduced. It depends on the lateral distribution of the absolute (physical) dose of an individual minibeam and, as the sim-

plest approach, on a threshold fraction S_{thres} of proliferating cells, i.e. all cells within a circle of diameter d_{eff} have a survival probability $\leq S_{thres}$. As two examples, the effective beam sizes are shown for a threshold cell survival of $S_{thres} = 50\,\%$ ($d_{eff,50\,\%}$) and $S_{thres} = 10\,\%$ ($d_{eff,10\,\%}$) in Fig. 6.8 and presented in Table 6.1 for the various minibeam irradiation modes of the tumor model. The effective beam sizes usually only increased slightly with tumor dose. While effective beam sizes were well below 2 mm in diameter for any irradiation modality and dose of the considered tumor model in the superficial layers (≤ 10 mm depth), up to 10 mm effective beam sizes were obtained close to the tumor at 90 mm depth. A general presentation of the biologically effective minibeam sizes in dependence of maximum dose of a Gaussian minibeam and for different assumed threshold fractions S_{thres} of proliferation are presented in section 6.5 in Fig. 6.15.

6.3 Discussion

Spatial fractionation can substantially reduce side effects when the dose is distributed into small planar or pencil channels within the healthy tissue. The clonogenic mean cell survival is taken as a first-order biological measure to compare different minibeam irradiation scenarios with regard to their tissue-sparing potential. The higher the mean cell survival the lower the expected side effects. In total, the mean cell survival is mainly determined by the σ/ctc ratio and to a minor extent to the mean dose of the minibeam irradiated area. This holds true as long as the $PVDR$ is not limited by beam halos. The utilized Linear-Quadratic model for calculating the clonogenic cell survival is inaccurate at high doses occurring in the minibeam peaks and could thus be replaced by more complicated cell survival models like the LQL model, as discussed in the Materials and Methods section. However, on the percentage scale of the calculated mean cell survival, the effect is negligible.

A second main ingredient, the effective beam size d_{eff}, influences the sparing potential in spatial fractionation as demonstrated in the mouse ear experiment of Sammer et al. [128]. It remains unclear how effective beam sizes influence tissue-sparing in minibeam irradiation in other organs and in human tissue and will be discussed more at the end of this chapter. Therefore, the optimization of minibeam irradiation modes is based on mean cell survival comparisons only.

It needs to be mentioned here, that the calculations made are neither conducted with regards to specific tissues nor to specified side effects. Within a whole organism, side effects are also affected by several other mechanisms like the integrity and function of cells that do not proliferate at all or do no longer proliferate after irradiation, immune responses, or bystander effects. The mean clonogenic cell survival served therefore only

as a measure that weighs dose distribution with a biological background but cannot forecast a whole radiation response. Different tissue types may not react according to a mean clonogenic cell survival if hot spots hit particularly sensitive tissues (e.g. serial tissues as the spinal cord). Similar mean cell survival for different tissues may also have a different severity in radiation response. For tumor tissues, it is not clear yet if a minimum dose is the only parameter of focus for tumor control. Hot spots as they appear from heterogeneous irradiation might be beneficial for tumor control by inducing immune responses [160]. Further investigations for healthy tissues and tumors need to be elaborated to gain a basic understanding of effects from valley, peak, and even mean doses. The development of more sophisticated tissue models might also be important to translate spatially fractionated dose distributions into normal tissue complication probabilities (NTCP) and tumor control probabilities (TCP).

In this approach, a beam preparation by ion beam focusing was assumed. This is an attractive method since lots of secondary radiation from collimation is prevented. However, it is technically more challenging even though there were already first attempts for pre-clinical designs [161] and even for a clinical accelerator [162]. Using a collimator for beam preparation, beam halos from additional scattering effects decrease peak-to-valley dose ratios compared to focused beams [162]. The halos depend on the details of collimator material, its geometry, the beam parameters, and the collimator-beam adjustment.

Additional *RBE* effects from the scattered particles [158, 163] also reduce the sparing within the dose valleys but probably play a less important role when a focused beam is chosen.

In the following discussion, it is often referred to as lower side effects and enhanced tissue-sparing based on the results from mean clonogenic cell survival calculations as a first-order approach since no other means are available, but the limitations of this approach need to be kept in mind.

6.3.1 Heterogeneous versus homogeneous tumor irradiation

In conventional external beam radiotherapy, the homogeneity dose criteria within a tumor are required by international standards [97, 98]. The principle of radiotherapy assumes that a tumor will be eliminated if any tumor stem cell is stopped from proliferation. Thus, a minimum dose is required at any position in the tumor. On the other hand, the normal tissue needs to be spared as much as possible such that no severe consequences for the patient occur. The upper dose limit as proposed e.g. by the ICRU report [97, 98] is mainly based on minimizing side effects in normal tissue rather than any adverse tumor control effects [164]. If the constraint on the upper dose

level counteracts healthy tissue-sparing it can be waived when larger dose fluctuations within the tumor can lead to lower side effects [139, 165].

The calculated mean clonogenic cell survival could be enhanced when proton minibeams were applied from two or more sides by interlacing the minibeam arrays (Figs. 6.3 and 6.6) and thus increasing the *ctc* distance. Interlacing implies that the dose maxima of the minibeams from one side are placed at the dose minima of the minibeams from the other side(s) (Fig. 6.1). However, since the widths of the minibeams from various directions differ in particular at the tumor edges, the *ctc* cannot be much enlarged when the homogeneity criteria of the ICRU report [97, 98] need to be fulfilled. Thus, tissue-sparing of interlaced minibeams was not much improved compared to superposed 1-dir minibeam applications where homogeneous dose distributions were obtained for each of the irradiation directions. In particular, mean cell survival and thus tissue-sparing effects close to the tumor edges remained low in both cases (Figs. 6.3 and 6.6, see also Table 6.1).

Mean clonogenic cell survival is enhanced in the healthy tissue even close to the tumor edges by interlacing proton minibeams when a heterogeneous dose distribution in the tumor is accepted. The only requirement is a minimum dose at any location in the tumor to achieve a tumor control at least as low as for the same homogeneous dose. For heterogeneous tumor irradiation with minimum dose D_{min} a higher mean dose is obtained, enlarged by a factor $f_D > 1$ compared to a homogeneous tumor irradiation with dose D_{min}. In the presented study, $D_{min} = 10\,\mathrm{Gy}$ was set to be compared with the same homogeneous dose in the tumor, but also $D_{min} = 2\,\mathrm{Gy}$ and $D_{min} = 35\,\mathrm{Gy}$ were considered. Mean clonogenic cell survival of heterogeneous proton minibeam irradiation modes was enhanced compared to that of the corresponding homogeneous irradiation modes in healthy tissue. The gain in cell survival in the dose valleys within the healthy tissue by enlarged *ctc* distances outnumbers its loss caused by the higher mean dose that has to be applied to the tumor to fulfill the minimum dose requirement. The resulting mean cell survival as obtained in superficial layers, as well as 1 cm in front of the tumor edge, is presented in Table 6.1. It demonstrates in detail the large enhancement in mean clonogenic cell survival compared to broadbeam, 1-dir minibeam, 2-dir, or 4-dir minibeam irradiations with homogeneous dose distributions in particular close to the tumor edges. Thus, lower side effects can be expected close to the tumor edges compared to any other proton irradiation mode with the same number of beam directions. Within the tumor, the higher mean tumor dose results in even enhanced tumor control in combination with the already advantageous heterogeneous tumor irradiations according to Prezado et al. [33]. The advantages of heterogeneous tumor irradiation could diminish the necessity of the same minimum dose as for homogeneous

tumor irradiation but need further experimental clarifications.

Comparing the 2-dir irradiations with interlaced pencil and planar minibeams, large differences in the applicable *ctc* distances could be noticed. While interlaced pencil minibeams of $ctc = 11\,\text{mm}$ required a doubling of the mean dose ($f_D = 2$), planar minibeams allowed for 17.9 mm *ctc* for the same increase of the mean dose. The larger possible *ctc* distances for the planar case diminished the geometrical advantages of the pencil beams in the entrance channel. While between 90 - 98 % mean clonogenic cell survival could be found for interlaced pencil minibeams in the superficial layers, the planar minibeams showed only 75 – 95 % ($D_{min} = 10\,\text{Gy}$). However, at the tumor edges, higher mean cell survival with up to 37 % could be found for planar minibeams in comparison to up to 32 % for pencil minibeams ($D_{min} = 10\,\text{Gy}$). Another advantage of planar minibeams is that beam production as well as beam delivery and positioning may be technically simpler than for pencil minibeams. The focusing strength of single magnetic quadrupole lenses to form a planar focus is much higher than the duplet arrangement of quadrupoles necessary for pencil minibeams. Besides, high precision to interlace planar beams is only required in one dimension. However, it remains to be investigated by radiobiological experiments whether spatial fractionation by pencil minibeams is more effective in tissue-sparing compared to planar minibeam arrangements even in cases where mean cell survival is somewhat smaller than in the planar case.

From a geometrical point of view, we found that for centered tumors the most favorable interlacing geometry is irradiation with planar minibeams from four directions due to the quartering of the dose and the large possible *ctc* distances from each direction. The optimum modeled case allowed for a *ctc* distance of $ctc = 20.4\,\text{mm}$ when the mean dose was $f_D = 1.21$ times larger within the tumor. The optimized mean cell survival of 46.9 % at 10 mm in front of the tumor was obtained with these parameters at a minimum tumor dose of $D_{min} = 10\,\text{Gy}$. Nevertheless, it needs to be elucidated in future studies whether a cell survival of 47 % from four directions is more beneficial than a 37 % cell survival from two directions meaning that only half the volume of healthy tissue is affected. Using a single-energy distal edge approach for 2-dir opposing irradiation schemes instead of a spread-out Bragg peak might become a technically simplified approach for interlaced minibeams with heterogeneous tumor dose.

6.3.2 Hypofractionated interlaced minibeam irradiation

Mean cell survival in the healthy tissue up to the tumor edge with the applied (heterogeneous) dose in the tumor could be held at significant levels (> 5 - 10 %) even for $D_{min} = 35\,\text{Gy}$ dose minima in the tumor and mean doses of up to 70 Gy. Nevertheless,

it will be important to translate and quantify cell survival into actual side effects as done in an early approach by Wheldon et al. [166]. Cell survival is not only dependent on dose but also on tissue type and will therefore cause clear effort in future quantification studies of tissue response to radiation.

The high cell survival up to the tumor edge allows for hypofractionation or even single fraction treatment. In addition, best tissue-sparing by overlaid temporal fractionation of minibeam irradiation modes would require a well-adjusted reproduction of the irradiation arrays from one fraction to the next to obtain the best overlap of the lateral dose profiles. It has been proven in a mouse ear model that a precise adjustment of four temporal daily fractions results in much better tissue-sparing than when each of the temporal fractions was shifted by half a *ctc* distance [167]. Submillimeter positioning of the minibeams from one irradiation to the next requires large technical effort and might be hindered by organ movement. Hence, a single fraction may be the best option to use spatial fractionation instead of temporal fractionation for tumor irradiation. Intrafractional organ movement may be reduced by applying flash irradiation protocols to avoid dose inaccuracies. An option for a few temporal fractions without requiring the interfractional sub-millimeter position accuracy would be e.g. pairwise applied interlaced minibeam fields from several directions within the three dimensions. This approach is similar to the one of Serduc et al. [137] for MRT but with the difference that a sufficient tumor coverage in interlaced MRT is achieved only after application of all MRT fractions or beam directions. The advantage of using ions is the pairwise interlacing that covers the whole tumor with a defined minimum dose in each fraction. The finite range of the ions allows several incident angles for pairwise interlacing. As a result, the irradiation directions between temporal fractions would only have a minor overlap in the healthy tissue.

6.3.3 Biologically effective minibeam sizes

The tissue-sparing potential by spatial fractionation depends on the kind of irradiated normal tissue, in particular, whether being parallel or serial. The survival and function of partially irradiated organs are described by the dose-volume effect [16, 17]. The injury of serial organs is dominated by the maximum appearing dose [69]. Hence, it will be important to be aware of the absolute positioning of the minibeams within these organs at risk. In contrary to organs at risk, the positioning of minibeams can also be used to efficiently target aggressive cancer cells within high-risk tumor subregions [168].

In parallel organs, small lesions within the organ will not lead to a disfunction as long as parts of the organ remain intact. Examples of this behavior are liver, lung, and in part skin tissue when the lesions are small. The sizes of destructed lesions that are

acceptable by the organs are in general not yet well known. As proven for skin tissue in a mouse ear model, the skin does not show much reaction when 0.18 mm channels are irradiated with high doses ($\sim 6000\,\mathrm{Gy}$) leaving skin areas between the channels at very low doses [31]. An additional experiment showed that reactions are barely visible for irradiations with a single pencil beam of $\leq 2\,\mathrm{mm}$ diameter while a gradual increase of inflammation reactions is detectable with the diameter of a single beam increasing beyond 3 mm [128]. The inflammation in the same ear model also gradually intensifies for a grid irradiation of 16 pencil minibeams when the ratio of beam size to center-to-center distance σ/ctc increases much above 0.1 [118]. Skin repair is associated with repopulation and migrating healthy, proliferating cells from low dosed areas to the heavily irradiated ones. Hence, the high dose regions will recover although the cells that were originally present in the high dose region will not proliferate any more with high probability. Characteristic migration lengths limit the size of damaged skin areas that are efficiently repaired.

As a consequence, radiation responses are not only influenced by mean cell survival but also by the effective minibeam sizes. It is necessary to evaluate the biological responses of various organs to spatial fractionation in dependence of the effective minibeam sizes. The study in the mouse ear model suggested a major reduction of side effects for effective beam sizes below 3 mm [128] although even larger beam sizes resulted in some reduction of radiation responses. The study was performed for pencil beams only. It remains to be clarified whether size limits differ between pencil and planar beams, which limits are given for different organs and how these limits change from small animals to human tissue.

In particular, it currently remains unclear which biologically effective beam sizes are acceptable between different species and tissues in order to profit most from spatial fractionation. For deep-lying tumors, the effective proton minibeam sizes can be well above 3 mm as demonstrated for the 5 cm thick tumor at a depth of 10 cm as considered here (Table 6.1). Beam sizes become even wider when tumors are situated deeper in the body. Heavier ion beams like helium or carbon beams experience much less lateral spread and can be used to form smaller minibeams deep in the body if needed [27]. The lateral spread of helium beams is about half of that of proton beams, that of carbon beams about a quarter [142, 169]. However, carbon ion therapy suffers from a considerable beam fragmentation tail at the distal end of the tumor. Thus, helium ions, that suffer much less from fragmentation, might be a good compromise for reduced effective beam sizes since they maintain low valley doses at the edges of deep-lying tumors for interlaced minibeam treatment even at high minimum tumor doses as required for hypofractionation [169].

Besides the fragmentation dose tail beyond the Bragg peak and the different *RBE* contributions for the heavier ions, interlaced minibeam geometries can be taken the same as for the proton case, but the *ctc* distances need to be decreased according to the reduced beamwidth σ keeping the σ/ctc ratio as in the proton case. Dose heterogeneity in the tumor and mean cell survival in the healthy tissue remains similar as calculated for protons but the lateral dimensions are smaller. Thus, spatial fractionation could profit from helium or carbon ions according to the reduced effective beam sizes in normal tissue.

6.4 Conclusion

Interlaced proton minibeams is a spatially fractionated radiation method that substantially spares healthy tissues in comparison to conventional broadbeam irradiation. Interlaced dose distributions from two and four directions were calculated and evaluated with respect to the sparing potential of healthy tissue by comparing mean clonogenic cell survival at a certain distance to the tumor edges. Interlaced minibeam irradiations revealed enhanced mean clonogenic cell survival compared to unidirectional minibeam irradiation. The mean clonogenic cell survival of interlaced proton minibeams profits most, in particular close to the tumor edge, by the application of a heterogeneous tumor dose, in particular taking beams from four directions. The geometrical sparing predominates the reduction of adverse side effects in spite of an increased mean dose, which is required to fill the cold spots within the tumor volume. Thus, side effects are reduced and even higher mean doses are applied to the tumor.

Proton minibeams were of significant advantage for high dose fractions ($\geq 10\,\mathrm{Gy}$), i.e. hypofractionation. Hence, single fraction tumor treatment at acceptable side effects even close to the tumor edges comes into reach when applying interlaced minibeams with heterogeneous tumor dose. High cost reductions are expected despite the higher effort to produce and adjust the interlaced minibeams.

One of the main obstacles in using proton minibeams for interlaced irradiation modes is the biologically effective beam size of single minibeams inside the healthy tissue. Especially at larger depths, the lateral spread through multiple small-angle scattering limits smaller beam sizes. If needed, smaller effective beam sizes can be achieved using heavy-ion minibeams, e.g. using helium or, with pros and cons, carbon ions.

The findings may pave the way for technical solutions in preclinical and clinical proton or heavy-ion minibeam therapy. Altogether, we recommend focusing on high-dose planar minibeams in future interlacing studies due to easier feasibility as well as higher

flexibility of irradiation modes. However, pencil minibeams have a two-dimensional repair geometry compared to the one-dimensional one of planar minibeams. Thus, their healthy tissue-sparing potential has to be compared at the same or even lower mean cell survival.

6.5 Further information and extended discussion

This section serves to describe and discuss in more detail the newly introduced concepts of this chapter, e.g., dose multiplication factor f_D or effective beam size d_{eff}. The new results shown here do not change the conclusions drawn in the main text, but provide a deeper insight that would go beyond the scope of the main text.

6.5.1 Interlacing from four directions: Comparison to previous studies

Dilmanian et al. [27] and Henry et al. [136, 138] had similar but in detail different approaches when it comes to interlacing from four directions. Their concepts are schematically presented in Fig. 6.9 to be compared with our interlacing approach presented in Fig. 6.1f.

Dilmanian et al. [27] suggested a superposed application of planar beams from opposite directions. That means that these beams are not interlaced but meet the same plane within the tumor. The orthogonal directions are interlaced only. This concept leads to smaller *ctc* spacings compared to the approach of Fig. 6.1f where the irradiated planes of all directions are interlaced. Thus, less tissue-sparing is expected using this approach compared to the actual 4-dir interlacing (Fig. 6.1f)

Henry et al. [136, 138] suggested the interlacing from opposite directions similar to the 2-dir case (Fig. 6.1d) and superposing the orthogonal directions setting the planes perpendicular to each other. In this case, too, the tissue-sparing does only profit from an interlacing approach from two directions but does not fully take the advantage when irradiating with minibeams from four directions.

Thus, both approaches basically interlace from two directions, but split the dose into four directions. The split of the dose as used in conventional radiotherapy plus the strong spatial fractionation leads to an enhanced dose tolerance of the traversed tissues but can keep the tumor dose homogeneous [97, 98]. A comparison between the interlacing methods of Dilmanian, Henry, and this study on the basis of cell survival are presented in Fig. 6.10a for homogeneous tumor irradiation. The differences are very

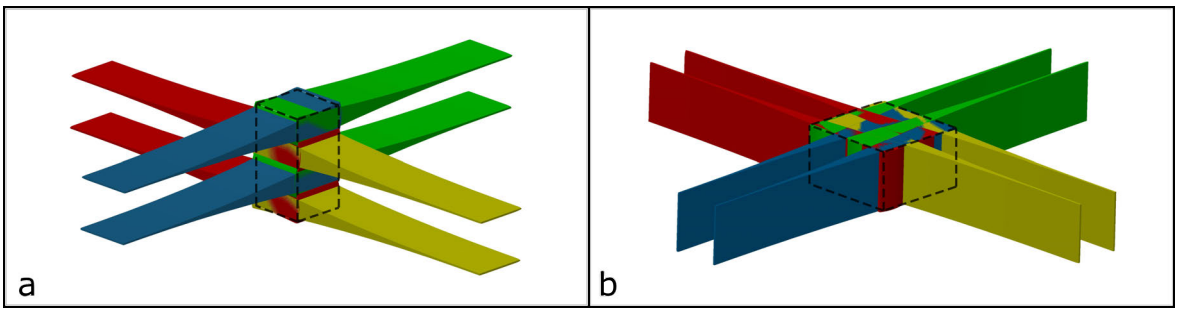

Figure 6.9: *Schematic illustration of 4-dir interlacing as suggested by Dilmanian et al. (a) and Henry et al. (b). Figures are created using the Creo 2.0 software. Credit: Peter Hartung.*

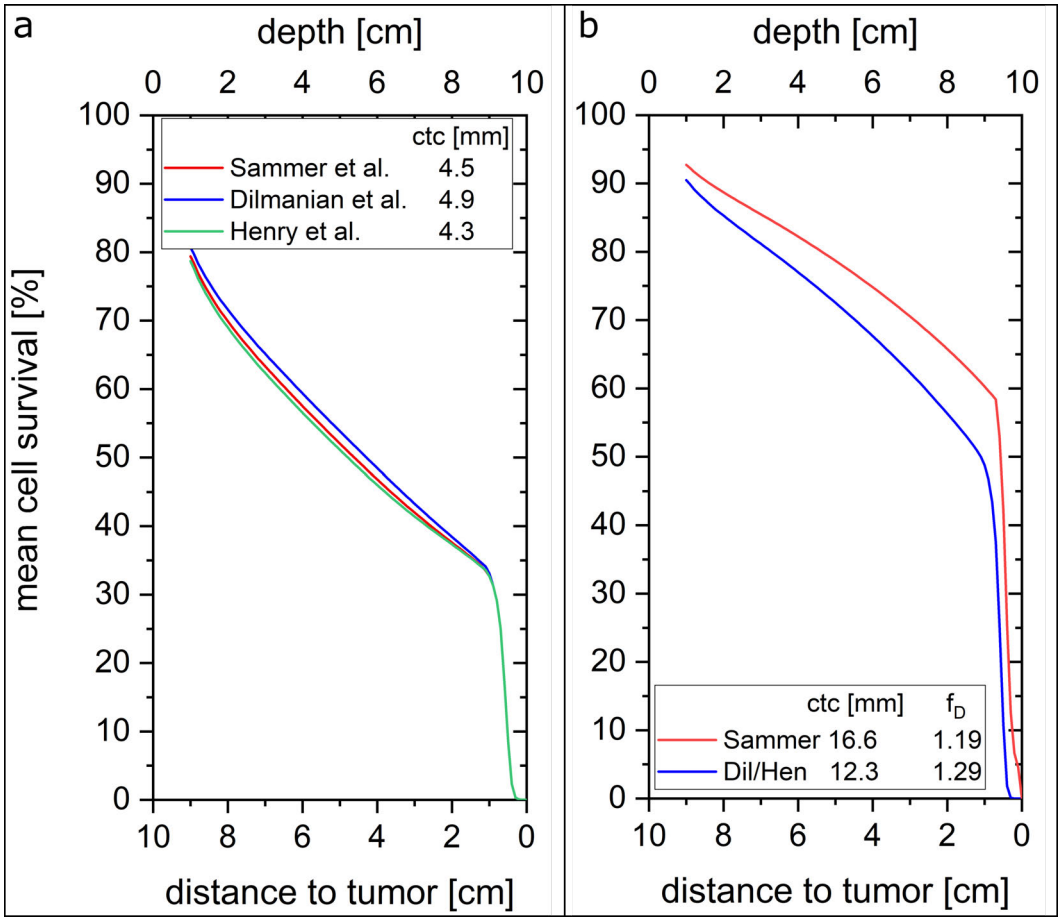

Figure 6.10: *Cell survival of different 4-dir interlacing methods of this study (red line), Dilmanian et al. (blue line) and Henry et al. (green line) for a 10 Gy homogeneous tumor irradiation (a) and optimized heterogeneous irradiation with 10 Gy minimum tumor dose (b). The tumor is located in 10 – 15 cm depth.*

small between the three arrangements for homogeneous tumor irradiation. The scattering within the tumor led to a slightly enhanced uniformity of Dilmanian's concept leading to a *ctc* of 4.9 mm. The interlacing of Henry et al. only allowed the same *ctc* distances as a standard 2-dir interlacing. There was no significant difference between the three methods.

When it comes to heterogeneous irradiation, both approaches of Dilmanian and Henry were similar to 2-dir interlacing with planar beams. The main advantage is based on the dose split. Comparisons between the 4-dir irradiation concepts of Dilmanian et al. and Henry et al. (Fig. 6.9) as well as the presented approach (Fig. 6.1f) with heterogeneous tumor dose (10 Gy minimum) are depicted in Fig. 6.10b. Cell survival was larger for the concept of four interlaced planar beams as suggested in the presented study in comparison to the superposed 2-dir concepts of Henry et al. and Dilmanian et al.. This enhanced cell survival was already obtained at a lower dose enhancement factor. However, the main advantage was found in the dose enhancement (see section 6.5.2), which needed to be only increased by a factor of $f_D = 1.19$ rather than $f_D = 1.29$ in the optimum case (local minimum). Therefore, larger *ctc* were enabled at lower dose enhancement factors and dose fluctuations in the tumor leading to higher tissue-sparing capabilities of healthy tissues.

6.5.2 Mean dose multiplication factor f_D

In normal tissue, the stronger the dose modulation, the more sparing can be achieved [99, 118]. However, if every cell within the tumor volume should be irradiated with a minimum amount of dose, the mean dose needs to be increased for heterogeneous dose distributions to fulfill this minimum criterion. The stronger the dose heterogeneity the higher the mean dose has to be set to lift the minimal dose D_{min}. A schematic illustration of the different dose modulations is shown in Fig. 6.11b/c. Fig. 6.11d displays the same dose modulation as in Fig. 6.11c but with the mean dose increased by a factor f_D of $f_D = 1.5$, leading to a lifted minimum dose to approach the required prescribed dose D_t. The multiplication factor f_D in dependence of the *ctc* distance is displayed in Fig. 6.12a for the 2-dir planar pMBRT irradiation using the 1-Gaussian approach as it is sufficient for the description of the tumor dose modulation. In most of the displayed *ctc* range, f_D increases with *ctc*, but there is a local minimum due to geometrical effects that occur in interlacing scenarios from two or more directions where in and outgoing beams are of different size ($\sigma_{prox} = 1.88$ mm and $\sigma_{dist} = 3.17$ mm). For a *ctc* of 7 mm, the distal beam showed almost no dose modulation (red line, Fig. 6.12b) and the overall dose modulation (yellow line) is only determined by the incoming beam (blue line).

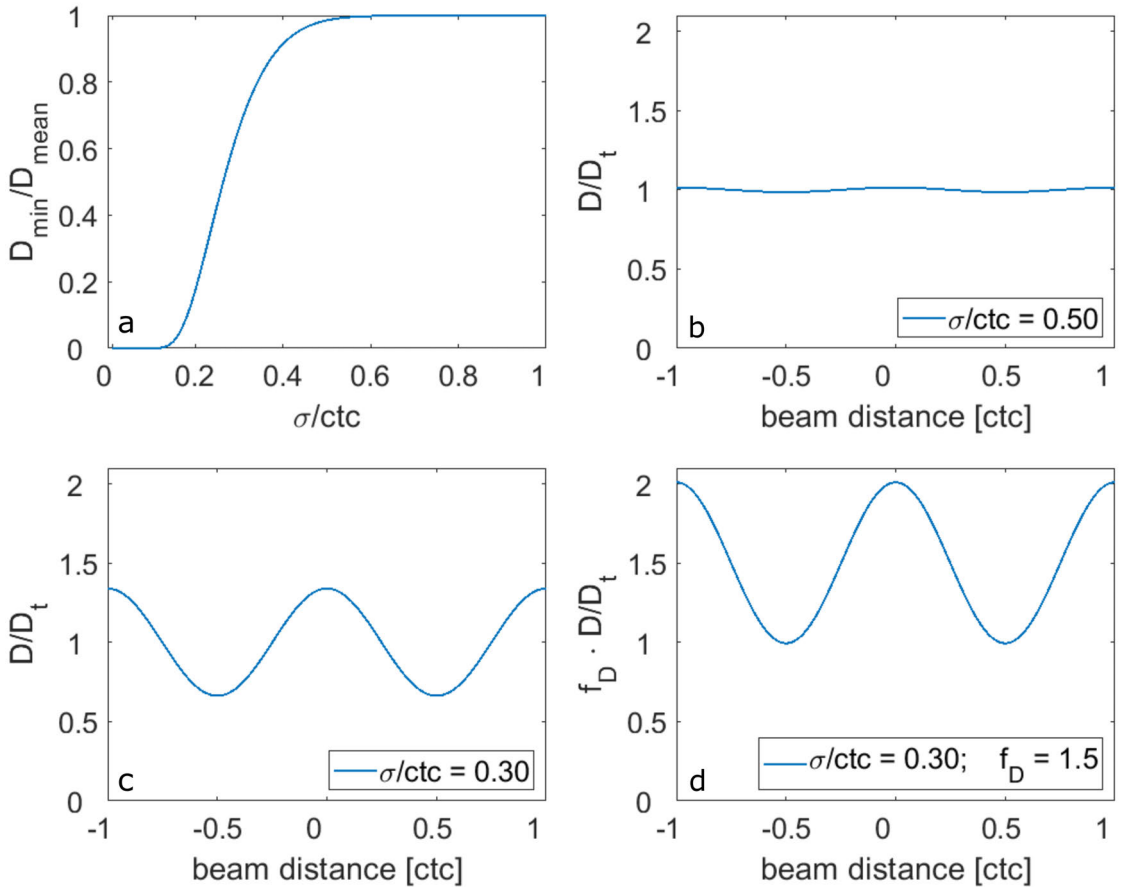

Figure 6.11: *Representative plots for the minimum dose dependency on σ/ctc (a), different dose modulations of $\sigma/ctc = 0.5$ (b) and $\sigma/ctc = 0.3$ (c) as well as a high dose modulation $\sigma/ctc = 0.3$ with increased mean dose by $f_D = 1.5$ (d).*

The proximal dose modulation caused an increase of the mean dose by $f_D = 1.24$ to fulfill the minimum criterion. In the case of $ctc = 9.4\,\text{mm}$ (Fig. 6.12c), the valley dose of the incoming beam (blue line) dropped more than the maximum of the outgoing beam increased because of the beam size differences. This asymmetric behavior caused the necessity of a local f_D maximum at $ctc = 9.4\,\text{mm}$ to lift the minimum dose of the dose sums (yellow line) to $0.975 \cdot D_t$. Increasing the ctc to even 12.3 mm (Fig. 6.12d) delivered the, from a dose point of view, ideal situation, where the dose valley of the incoming beam (blue line) and the dose peak of the outgoing beam (red line) compensated each other. The integral dose valley in the yellow line was here the broadest. Increasing the ctc distance even further to $ctc = 18.8\,\text{mm}$ resulted in the formation of two local minima. The outgoing beam (red line) was too small to cover the full valley of the incoming beam (blue line), which resulted in the two minima of the steep slopes of neighboring Gaussians. Therefore, the minima decreased exponentially which was

observed in the exponential increase of f_D for $ctc > 12.3\,\text{mm}$ in Fig. 6.12a. The behavior of f_D in dependence of ctc depended on irradiation modality (pencil vs. planar and also 2-dir vs. 4-dir) and especially on the in- and outgoing beam sizes which vary with tumor size and location.

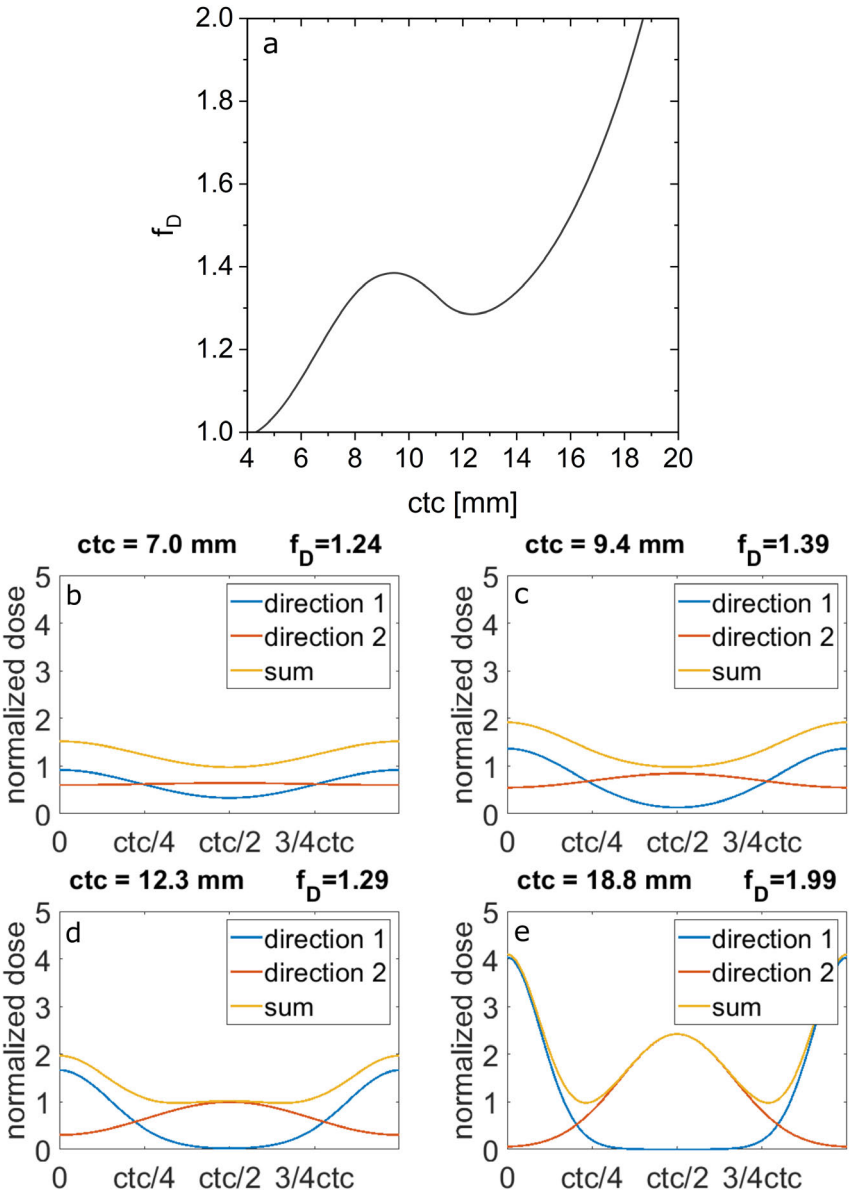

Figure 6.12: *Multiplication factor f_D of the mean dose as a function of the ctc distance required to fulfill the minimum criterion $D_{min}/D_t = 0.975$ (a). The local dose distributions for different ctc at the proximal tumor depth of 10 cm for different ctc are shown in the subfigures b - e. The shown curves are only valid for the 2-dir planar pMBRT irradiation with the 1-Gaussian approximation.*

6.5.3 Interlacing in thinner tumor models

Thick tumors as described in section 6.1 and considered in the dose calculations of Figs. 6.2 and 6.5 showed a strong difference in the dose modulation of beams from two opposing directions ("in- and outgoing" beams). For thin tumors, the difference between in and outgoing beams is reduced by the lower tumor thickness that contributes to the scattering of the particles within the tumor volume. Two tumor scenarios with a thin tumor were also considered and calculated to gain further insight into the application and advantages of interlaced minibeams under the restriction of a homogeneous irradiation. One thin tumor (T2) was located at 12 – 13 cm depth from each side and its proximal and distal beam sizes were $\sigma_{prox} = 2.58$ mm and $\sigma_{dist} = 2.69$ mm (compared to $\sigma_{prox} = 1.88$ mm and $\sigma_{dist} = 3.17$ mm for the 5 cm thick tumor in the same phantom (T1)). The larger incoming beam size was due to the differences in entrance length (12 cm for T2 and 10 cm for T1), which led to the calculation of an additional thin tumor, T3, in 10 – 11 cm depth from each side. For T3, the phantom length reduces to only 21 cm. The beam sizes for T3 were $\sigma_{prox} = 2.15$ mm and $\sigma_{dist} = 2.33$ mm. The incoming beam size was also larger than for T1 due to the lower maximum particle energy (less penetration depth required), which delivered the main dose fraction. The scattering of the particle beam, however, increased for lower energies. Because of the beam sizes, the *ctc* distances for T2 could be increased by the factors ~ 1.51 and ~ 1.49 (1.71 for four directions) for the planar and the pencil minibeam case, respectively, in comparison to similar irradiations for T1 and a homogeneous tumor irradiation. Due to the smaller beam size for T3 compared to T2, the factors decreased to ~ 1.23 (1.27 for four directions) for both, planar and pencil minibeam case in comparison to the *ctc* for homogeneous T1 irradiation.

The cell survival curves for homogeneous tumor irradiation for 10 and 35 Gy mean tumor dose are shown in Figs. 6.13 and 6.14. The cell survival curves for the 1 cm thick tumors (T2 and T3) followed the same principles as for the 5 cm tumor (T1). The pencil minibeams from two opposite directions resulted in the highest cell survival, especially in the superficial layers with up to 98 % cell survival. The difference between pencil and planar minibeams vanished at around 3 cm before the tumor. The geometrical arrangement of minibeams had therefore no influence on the cell survival of the close surroundings of a tumor. The merge between the minibeams and the broadbeam irradiation was at about 2 cm tumor distance. Hence, the close vicinity of the tumor suffered from similar cell death as for the broadbeam irradiation and minibeam irradiation did also not lead to a significant enhancement in thin tumors. Only the

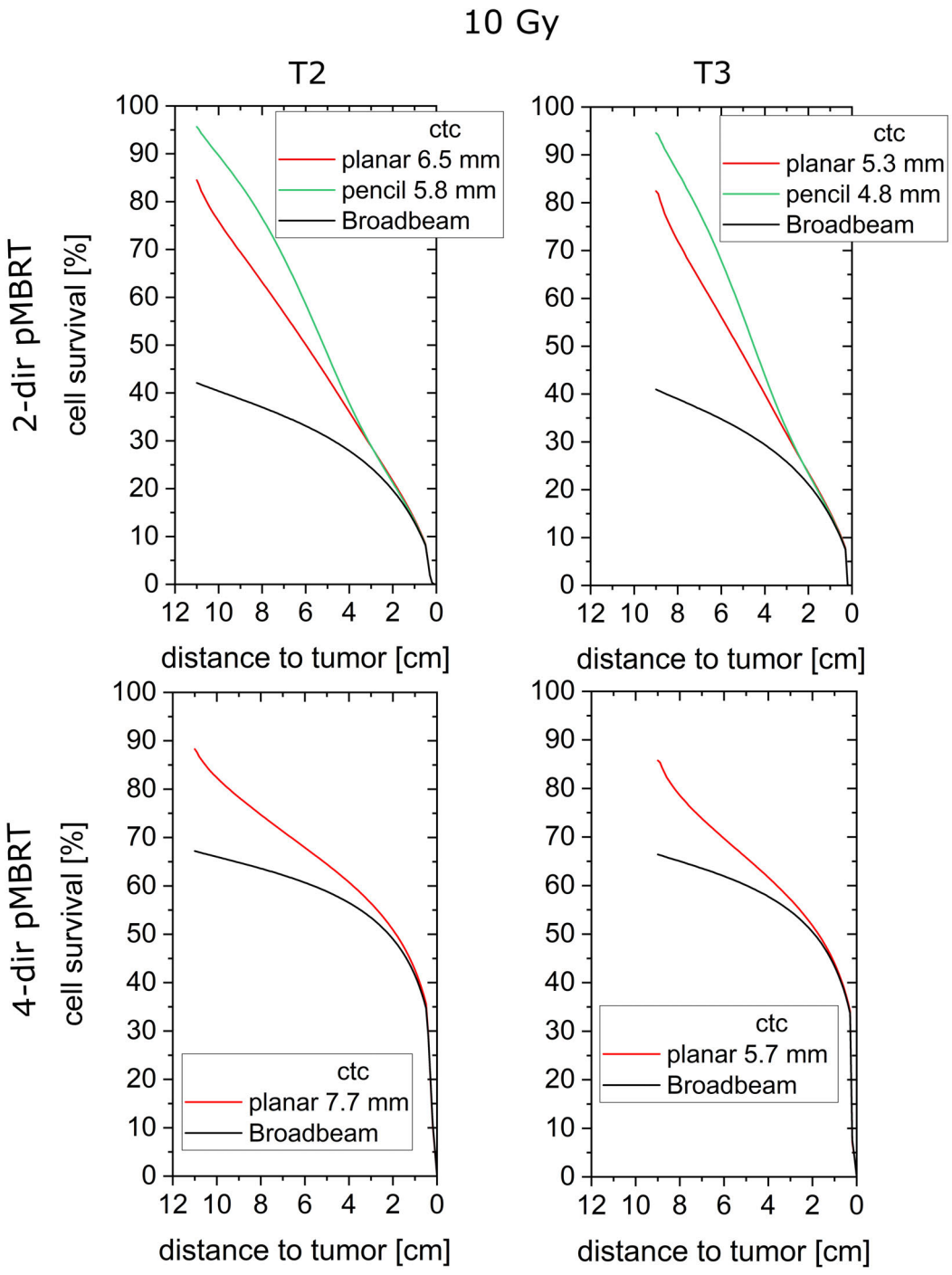

Figure 6.13: *Mean cell survival results for the interlaced homogeneous irradiation of two thinner tumor models, T2 and T3, from two opposite directions (two upper images) and four directions (two lower images). The tumor dose is 10 Gy.*

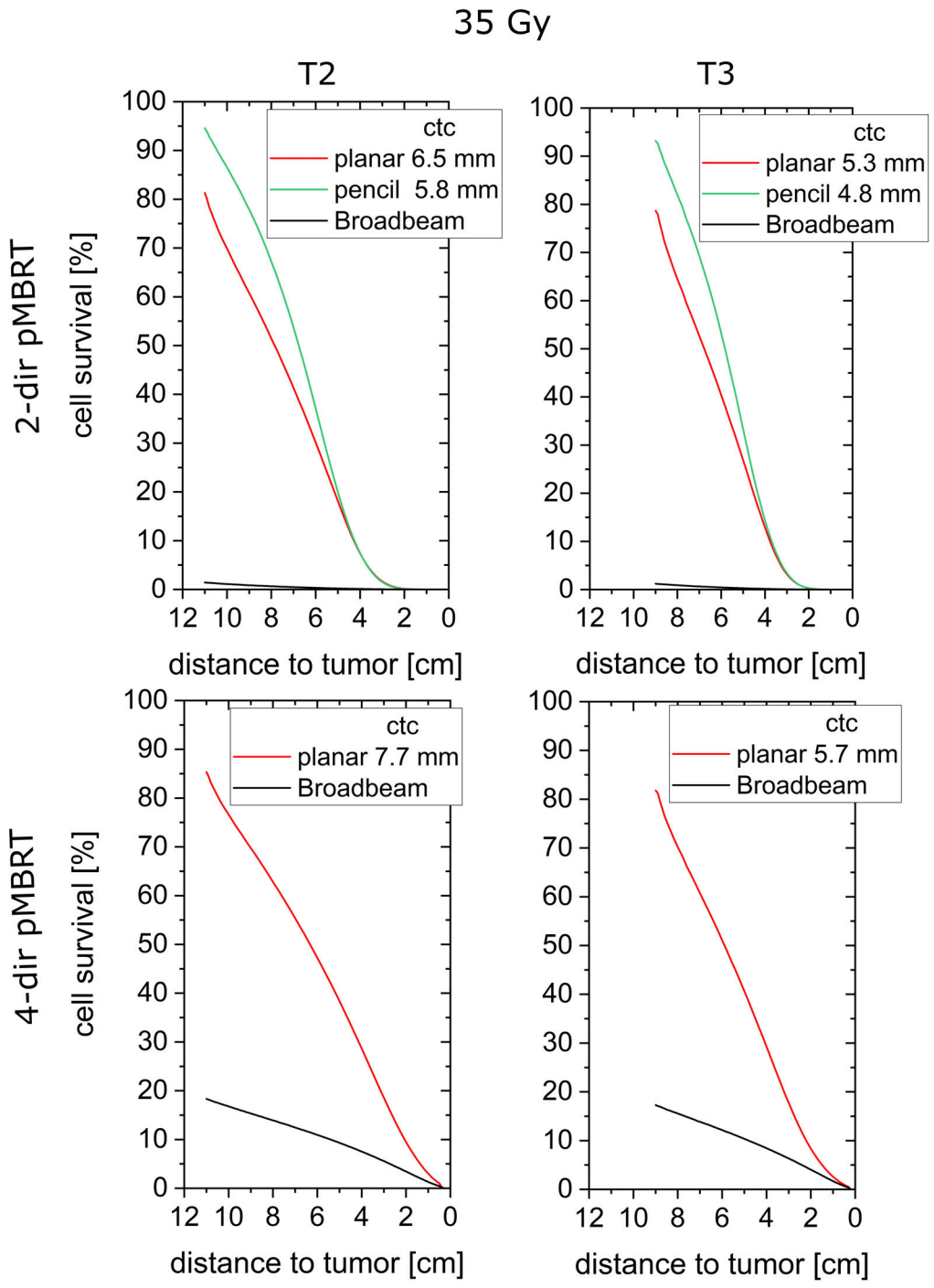

Figure 6.14: *Mean cell survival results for the interlaced homogeneous irradiation of two thinner tumor models, T2 and T3, from two opposite directions (two upper images) and four directions (two lower images). The tumor dose is 35 Gy.*

irradiation from four directions had a slightly increased cell survival up to 1 cm tumor distance. However, the generally higher cell survival of the four directions was mainly caused by the dose split.

Barely any differences could be observed comparing T2 and T3. The shorter entrance channel of 10 cm for T3 led to a slightly steeper decrease with depth in cell survival. The smaller *ctc* distances due to the smaller beam sizes showed no disadvantage in cell survival.

In general, the thin tumors cannot be treated any better than the thick tumor in case of homogeneous tumor irradiation, even though the dose modulations and beam sizes of in and outgoing beams barely differ. The main cause is the strong homogeneity requirement that prohibits dose modulations. Although some compensation of incoming and outgoing beam modulations is possible, the effect is too small and the close tumor surroundings suffer from high doses.

6.5.4 Effective beam size

The effective beam diameter d_{eff} as a function of the maximum dose D_{max} of the Gaussian is displayed in Fig. 6.15 for 1, 10, 50, 90 and 99 % cell survival. It can analytically be solved by the equation

$$D_{max} \cdot \exp\left(-\frac{r^2}{2\sigma^2}\right) \stackrel{!}{=} D, \tag{6.2}$$

where σ is the standard deviation of the Gaussian and D is the dose that induces the cell surival fraction S. The dose D is substituted using the LQ-model by

$$D = \frac{1}{2\beta}\left(-\alpha + \sqrt{\alpha^2 - 4\beta \ln S}\right), \tag{6.3}$$

with the parameter of the LQ-model α and β, and the survival fraction S $(0 < S < 1)$ In total, the analytical derivation of the effective beam size d_{eff} can be described by the equation

$$d_{eff}(\sigma) = \frac{2r}{\sigma} = \sqrt{8 \ln\left(\frac{2\beta D_{max}}{-\alpha + \sqrt{\alpha^2 - 4\beta \ln S}}\right)}. \tag{6.4}$$

The effective beam size is particularly sensitive for changes in the low dose range ($\sim 0-10$ Gy) due to the sensitivity of the Linear-Quadratic model and flattens for high peak doses. Therefore, high peak doses as they appear in the superficial layers of pMBRT cause only a minor increase in the effective beam size, especially considering the small physical beam sizes of only a few 100 µm. For instance, an increase of the

maximum dose from 100 Gy to 1000 Gy only increases the effective beam diameter by 1 - 1.5 standard deviations, depending on the cell survival rate. However, at the close tumor surroundings where physical beam sizes are already in the mm range, an increase of the effective beam size of only one standard deviation could decrease the sparing effect of spatial fractionation. The beam sizes where no reaction occurred was determined in a mouse ear model and found to be in the low mm range. A translation into human tissue is necessary, but expectations are of similar dimensions. As already written in the main discussion, this could be reduced by considering heavier ions as He or C to reduce the lateral scattering of single beams and therefore the absolute value of the effective beam size.

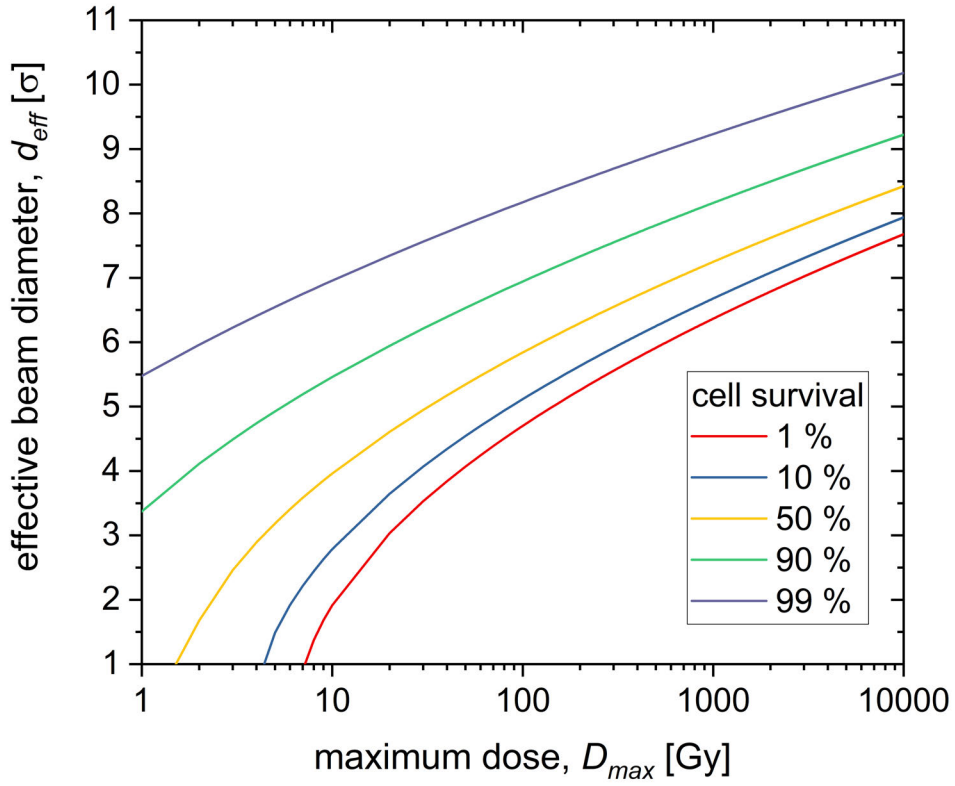

Figure 6.15: *Effective beam size (beam diameter in number of standard deviations σ) as a function of the maximum dose of a Gaussian dose distribution for five different cell survival values. The α and β values are the utilized α and β values α = 0.425 Gy^{-1} and β = 0.048 Gy^{-2} as in all simulations. Note that the maximum dose D_{max} axis is displayed on a logarithmic scale.*

Chapter 7

Conclusion and Outlook

7.1 Conclusion

Proton Minibeam Radiotherapy (pMBRT) is a novel approach in radiotherapy to enhance the therapeutic window. It is a spatially fractionated irradiation method that was introduced by Zlobinskaya et al. [29] and Prezado et al. [30] to spare healthy tissue. The sparing potential of spatial fractionation is based on the dose-volume effect [16, 17] and allows to irradiate small volumes with large doses. In case of proton minibeams, sub-millimeter sized beams are spaced in *ctc* distances of several mm to irradiate a patient. The beam size increases with depth due to small-angle scattering and allows, by adapting the *ctc* distances to the irradiation scenario [99], to cover the full tumor with a homogeneous dose according to the ICRU constraints [97, 98]. The spatially fractionated irradiation in the healthy tissue leads to reduced side effects [31, 32, 113], while the dose coverage of the tumor is expected to lead to the same tumor control probability as in conventional proton radiotherapy.

The first proof-of-principle in-vivo experiments concerning tissue-sparing potential with proton minibeams demonstrated strong tissue-sparing in a mouse ear model [31] and a rat brain model [32]. In this work, a follow-up study to investigate the sparing potential in dependence of the applied dose distribution was carried out. The established mouse ear model [31, 109] using the right ear of BALB/c mice was used. Different dose distributions of minibeams as they appear in different depths (between $\sigma/ctc = 0.09$ - 0.5) were applied to the ear model with a mean dose of 60 Gy. The direct comparison of the side effects allows for a resolution of the sparing potential depending on dose distribution and thus also on depth in tissue. While the strongest dose modulations did barely evoke side effects, the maximum tissue reactions increased linearly with increasing σ/ctc. Strong visible skin reactions such as desquamation and erythema were found for the dose modulations $\sigma/ctc \geq 0.23$. Also ear swelling was measured with up

to 3-fold the ear thickness of sham irradiated ears for homogeneously irradiated ears. In general, it was found that the closer the dose modulation was to that of a homogeneous irradiation ($\sim \sigma/ctc = 0.5$), the stronger the tissue toxicities. The findings prove that the tissue-sparing potential of proton minibeams decreases with depth until the reactions are similar to those of a homogeneous irradiation as suggested in theoretical calculations [99]. However, they also prove that minibeam irradiations are superior to conventional irradiations in context of side effects even at large depths of the entrance channel.

All proton minibeam experiments concerning tissue-sparing have so far been conducted in a single-shot experiment [29, 31, 32, 113]. In conventional radiotherapy, the standard method to treat a tumor and spare healthy tissue is temporal fractionation. Decades of medical experience in treating tumors with radiation is therefore based on treatment with temporal fractions. The combination of temporal and spatial fractionation causes new questions to be answered in particular with respect to reirradiation accuracies. In the second animal trial presented in this thesis, the BALB/c ear model was irradiated with four daily fractions of 30 Gy mean dose of 16 proton minibeams ($\sigma = 220$ µm; $ctc = 1.8$ mm) with either a highly accurate reirradiation (FS1) or a maximum spatial shift between the temporal fractions (FS2). The third irradiation group (FS3) accurately reirradiated 64 proton minibeams ($\sigma = 222$ µm; $ctc = 0.9$ mm) with 30 Gy mean dose per fraction. FS3 was designed to increase the valley dose per fraction but resulting in the same integral dose distribution as FS2 after the treatment, allowing to study the influence of different daily dose distributions. Only a 1.6-fold ear swelling was found for the accurate reirradiation of the strong daily dose modulation of FS1. The maximally shifted minibeams resulted in a 2.4-fold increase of ear thickness compared to sham irradiation. The strongest radiation response was observed for the reirradiation of the 64 minibeams of FS3 with a 3-fold ear swelling. After the observational period of 160 days, FS2 and FS3 still showed increased ear thickness of ~ 1.4-fold and ~ 1.7-fold, respectively. The histological analysis confirmed that the long-term ear swelling is caused by fibrotic tissue. The findings suggest that temporally fractionated minibeams yield the most tissue-sparing for an accurate reirradiation and strong daily dose modulations. Nevertheless, even a maximally shifted proton minibeam pattern is beneficial if the daily dose modulation is strong compared to an accurate reirradiation with weaker daily dose modulations. Therefore, the combination of spatial and temporal fractionation with protons is likely to be advantageous compared to conventional radiotherapy, even if an accurate reirradiation is not guaranteed.

Both conducted animal experiments state that proton minibeams spare tissue the most when the dose modulation is large. Since the dose modulation decreases with

depth due to small-angle scattering, the sparing of tissues also decreases. The last few centimeters within an proton minibeam entrance channel is already covered with a close to homogeneous dose distribution and side effects are indistinguishable from a conventional approach [99].

To also spare healthy tissues in deeper layers, the σ/ctc ratio needs to be decreased. This can only be achieved by increasing the *ctc* distances since the beam size σ is determined and limited by particle scattering. There are two options to increase the *ctc* distances. At first, the spatial fractionation allows for interlaced irradiation, where a beam pattern is applied from two or more directions and the peaks and valleys from different sides balance each other out within the tumor volume. The second option is the abandoning of the dose criteria for homogeneous irradiation and allowing for dose modulations within the tumor volume. To ensure or even enhance tumor control, the minimum tumor dose criterion was retained, whereas the maximum dose criterion was abandoned. The heterogeneous tumor irradiation allowed for enlarged *ctc* distances, therefore more sparing within the healthy tissues. Both methods can also be combined to further increase the tissue-sparing.

In a theoretical study, interlaced and/or heterogeneous tumor irradiations using proton minibeams are calculated and evaluated on the basis of clonogenic cell survival. While the pure interlacing as well as the pure heterogeneous tumor irradiation only yielded minor advantages, the combination of both methods could increase the calculated cell survival significantly. At 1 cm depth before the tumor, up to 47 % cell survival could be achieved for a minimum tumor dose of 10 Gy. Only 25 % cell survival is found at the same location with broadbeam irradiation. This significant increase of cell survival within the healthy tissue in combination with an at least as low cell survival within the tumor volume as in a uniform irradiation suggests a lower Normal Tissue Complication Probability (NTCP) at the at least same Tumor Control Probability (TCP), increasing the therapeutic window and offering more flexibility to clinicians. However, there are a few points that were not covered by the cell survival calculations, limiting the interpretation for a full radiation response. In particular, the biological effective beam sizes of single beams have been found in an animal trial [128] to be at few mm beam diameters. The scattering of protons can lead to several mm beam sizes in depth, which possibly diminishes the sparing potential of a minibeam pattern. This effect can be reduced using heavier ions, e.g. He or C, for minibeam therapy with the advantage of less scattering but the disadvantage of more technical effort to produce the beam energies and the heavy-ion minibeams itself.

7.2 Outlook

Both in-vivo studies as well as the in-silico study have presented a clear evidence for the strong sparing effect of proton minibeams in comparison to a conventional broadbeam irradiation. It is therefore a great new approach that enhances radiotherapy and should be considered for clinical implementation, although there are remaining questions to be answered.

All in-vivo proton minibeam experiments have either been conducted in the mouse ear [31, 113, 118, 167], the brain of rats [32–35] or the brain of mice [170]. Proton Minibeam Radiotherapy is, however, a concept that is adaptable to any tumor sort or location and will also affect other tissues (parallel or serial) than skin or the brain. It will be of high importance to investigate into the sparing potential of pMBRT within different tissue types. Besides, it will be necessary to understand the fundamental biological causes of the sparing potential of spatial fractionation including e.g. the dose-volume effect, bystander effects or the immune responses to benefit the most from proton minibeam therapy.

If the sparing potential as calculated within the theoretical study chapter 6 will be confirmed by biological experiments, it would challenge the conventional radiotherapy in several ways. Very high or even curative doses could be applied within one or few fractions leading to more time- and cost-efficient treatments. Additionally, the patient would benefit from lower side effects. But it is still unclear what doses (minimum doses and modulation), number of fractions and its temporal division is ideal for curative radiotherapy, especially as there is a great likelihood of tumor sort dependence. Two studies have demonstrated the efficacy of proton minibeams for tumor control in gliomas with at least the same tumor control, even with different tumor dose heterogeneity, as a conventional proton irradiation [33, 35]. Further experimental validation of the sparing effects, in particular for different tissues, and eventually the optimal tumor treatment is of importance before implementing pMBRT in the clinic.

There is also remaining work to be done when it comes to the technical realization. The collimation of a therapy beam can easily be implemented at any therapy center, but creates additional secondary particles that can decrease the dose modulation of the minibeam pattern [162], reducing its sparing potential. Collimators would also need an individual patient adaptation, increasing the work flow effort. Ideally, a proton minibeam would be designed using an ion lense for ion focusing. This allows to irradiate patients with individual minibeam pattern without suffering from unnecessary secondary radiation, similar to the commonly used pencil beam scanning. Although first theoretical studies have demonstrated the adaptation of an ion lense within a beam nozzle of a therapy center [162, 171], the technical limits are being reached with

only providing the minimum requirements for beam sizes. Therefore, new accelerator technologies might be necessary to optimize the minibeam production and to exploit pMBRT at its fullest.

All aspects considered, pMBRT will also reach its limits due to the strong lateral scattering of protons. Although the scattering is the basic ingredient for reaching tissue-sparing in combination with tumor dose coverage in spatial fractionation, the single beam size of proton minibeams in radiotherapy-relevant tissue depths might be limiting for tissue-sparing as discussed in chapter 6.3.3. The scattering can be reduced with heavier ions such as C or He, but is still strong enough to maintain tumor dose coverage by adjusting the *ctc* distance. Considering the physical properties of heavier ions, Helium is likely to be the ion of choice due to the minor impact of its fragmentation tail. All presented results within this thesis are adaptable and expected to deliver similar or better results using Helium ions. Apart from an economic discussion, technical innovations for accelerators in combination with minibeam radiotherapy should therefore include He-ion minibeams to improve radiotherapy for cancer patients as far as possible.

Appendix A

Ear thickness data of the in-vivo mouse ear study of chapter 4

The ear thickness of each individual mouse of the study presented in chapter 4 is presented for the monitoring period of 90 days. Each data point presents the mean value of a triplicate measurement. The mean thickness per time-point is the representative value for each group and used for evaluation in section 4.2.3.

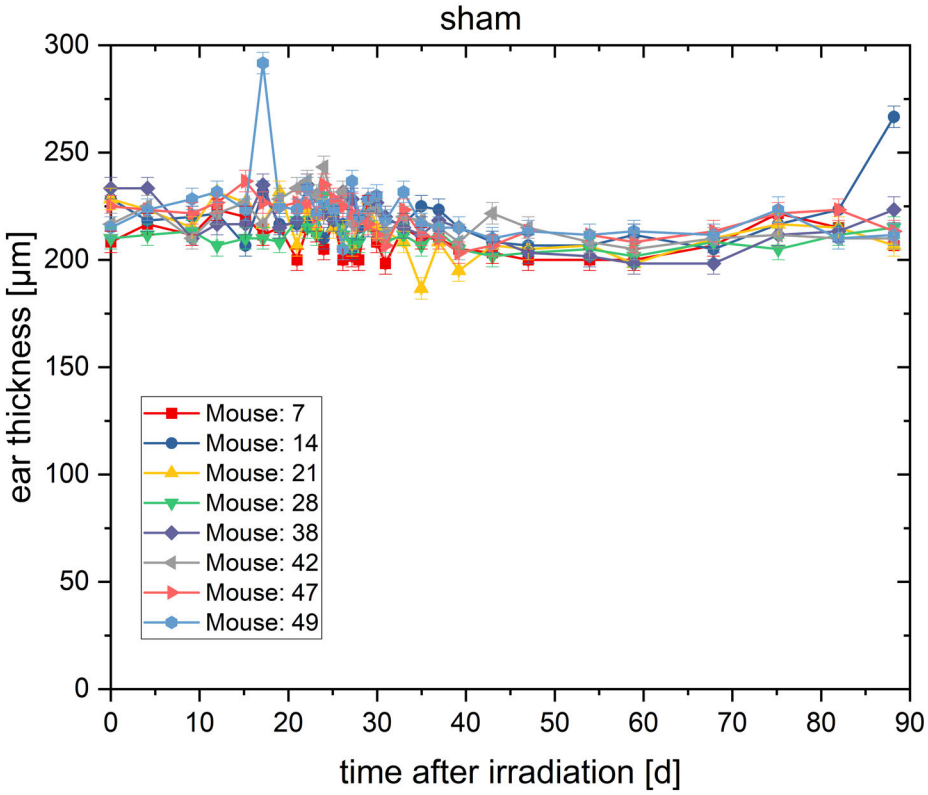

Figure A.1: *Ear thickness (± SEM) over the monitoring period of 90 days of each mouse for the sham-irradiated ear (0 Gy; control group).*

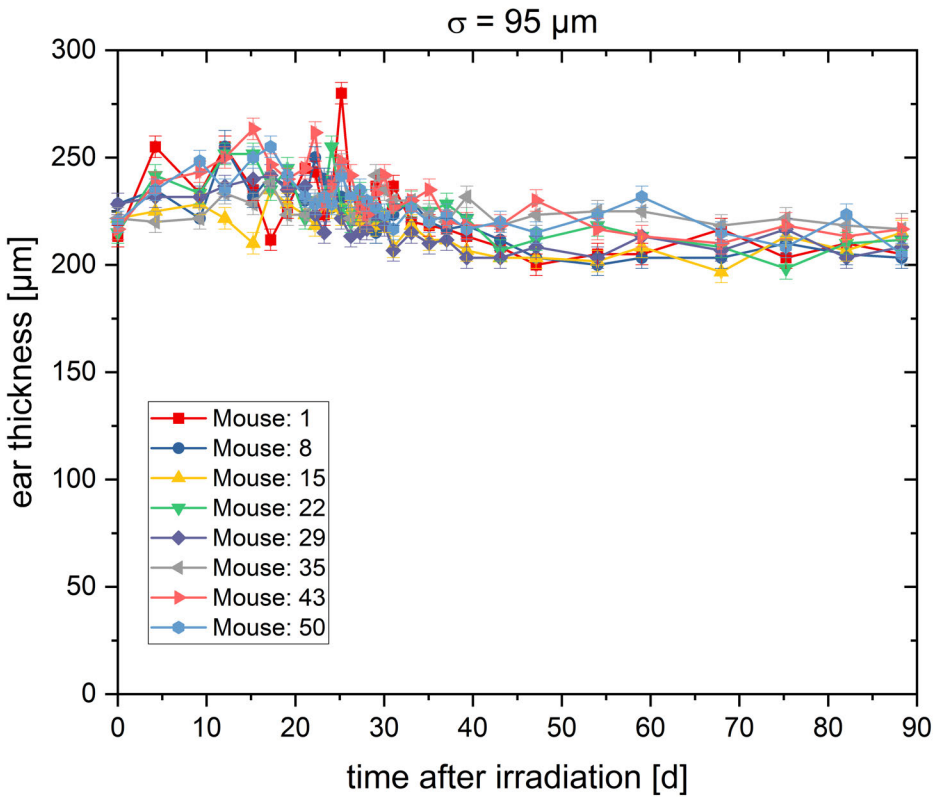

Figure A.2: *Ear thickness (± SEM) over the monitoring period of 90 days of each mouse irradiated with the minibeam size $\sigma = 95\,\mu m$.*

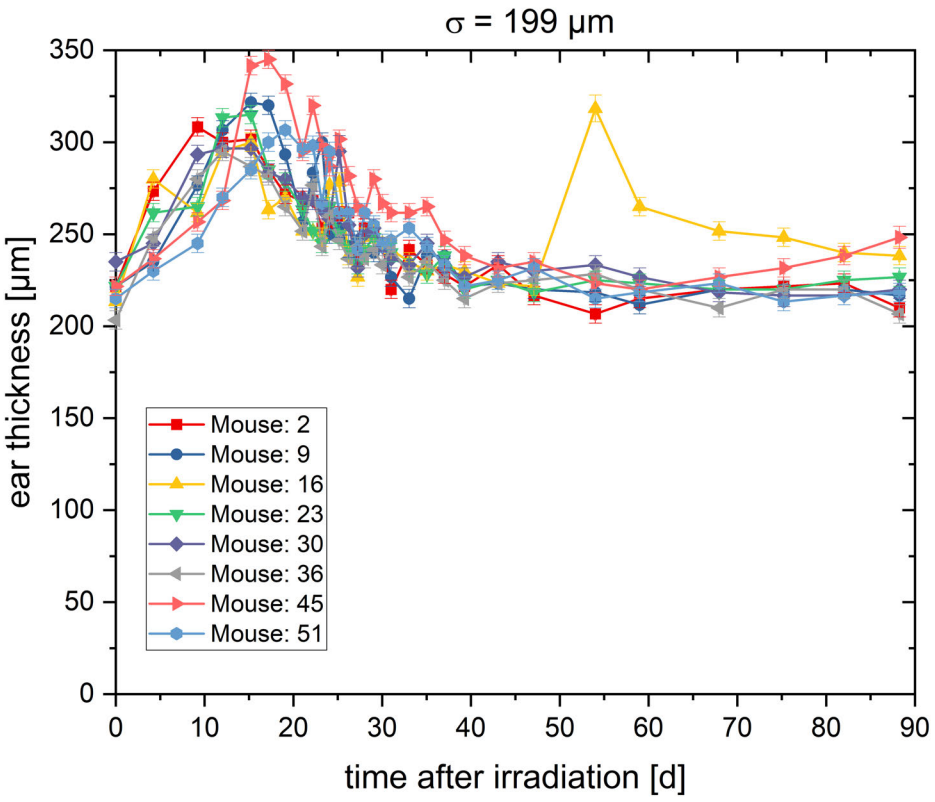

Figure A.3: *Ear thickness (± SEM) over the monitoring period of 90 days of each mouse irradiated with the minibeam size $\sigma = 199\,\mu m$.*

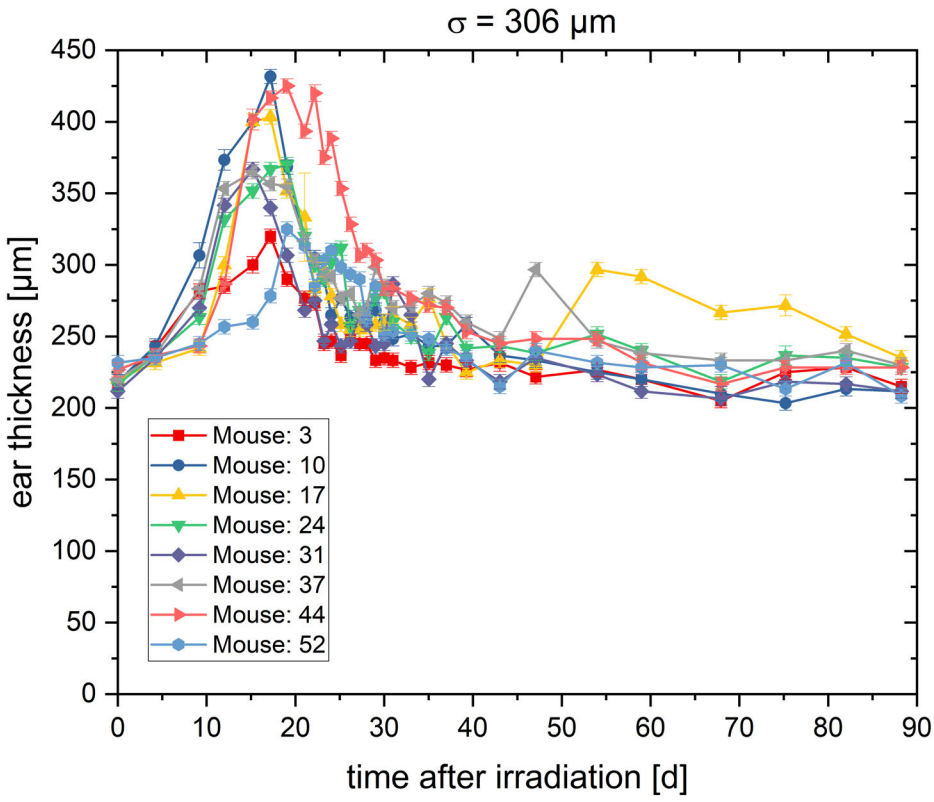

Figure A.4: *Ear thickness (± SEM) over the monitoring period of 90 days of each mouse irradiated with the minibeam size $\sigma = 306\,\mu m$.*

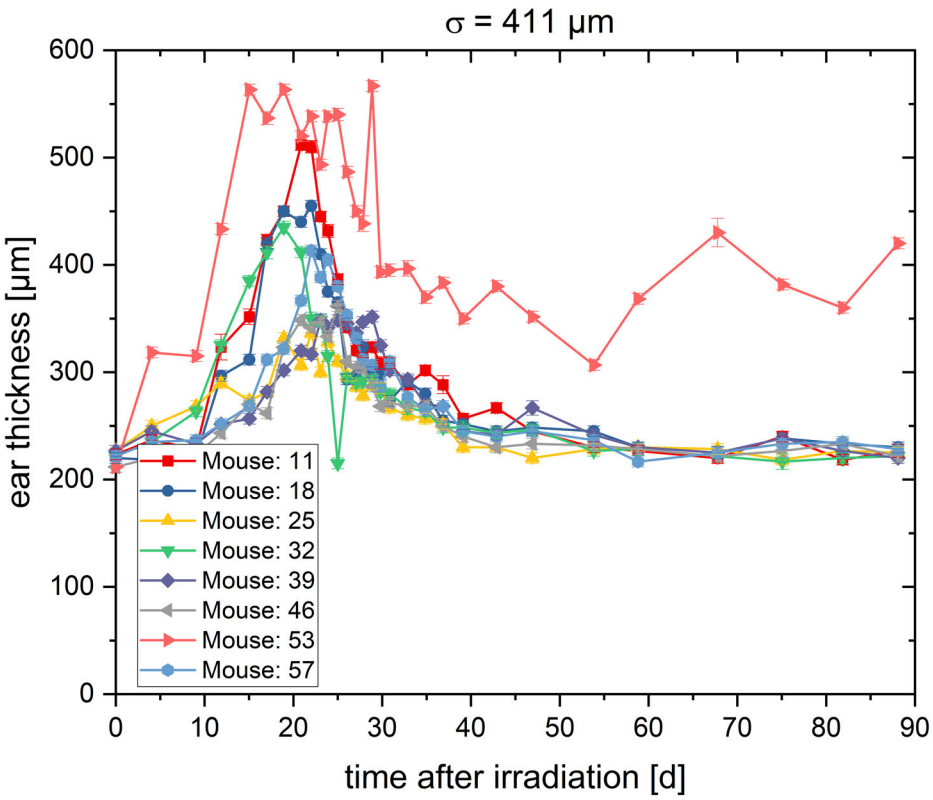

Figure A.5: *Ear thickness (± SEM) over the monitoring period of 90 days of each mouse irradiated with the minibeam size $\sigma = 411\,\mu m$.*

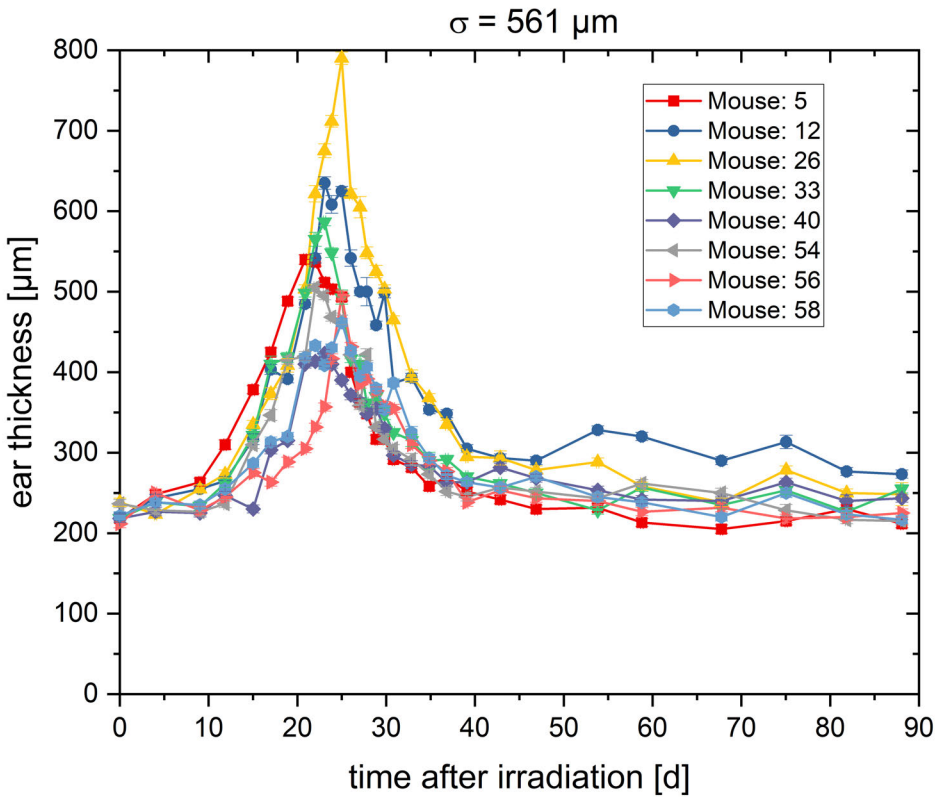

Figure A.6: *Ear thickness (± SEM) over the monitoring period of 90 days of each mouse irradiated with the minibeam size $\sigma = 561\,\mu m$.*

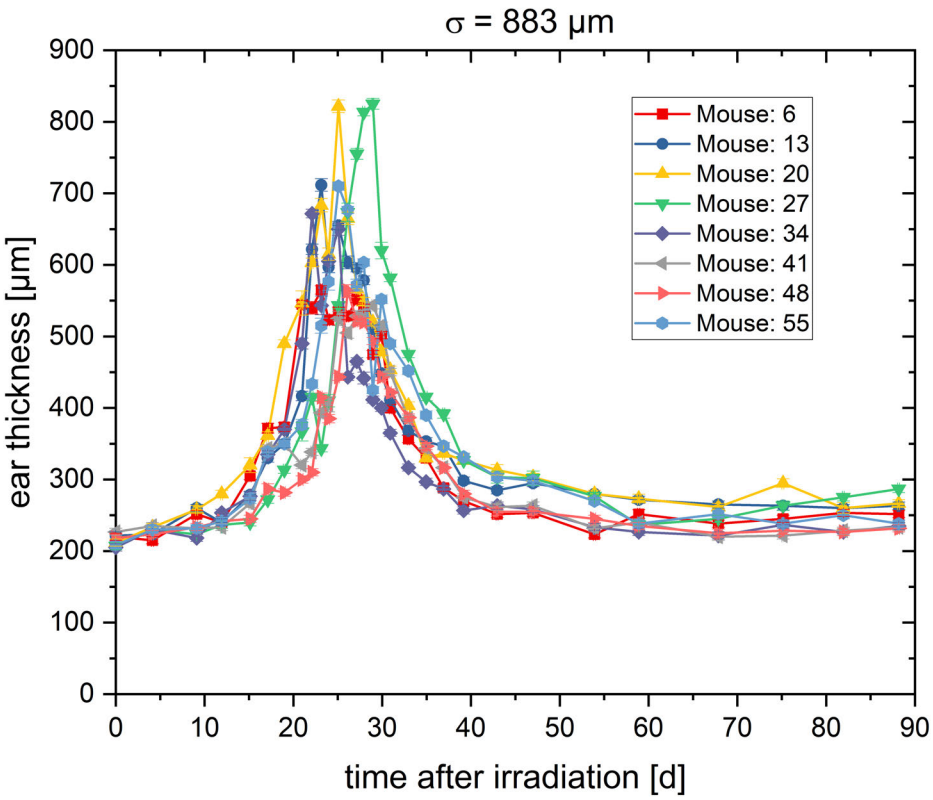

Figure A.7: *Ear thickness (± SEM) over the monitoring period of 90 days of each mouse irradiated with the minibeam size $\sigma = 883\,\mu m$.*

Appendix B

Ear thickness data of the in-vivo mouse ear study of chapter 5

The ear thickness of each individual mouse of the study presented in chapter 5 is presented for the monitoring period of 160 days. Each data point presents the mean value of a triplicate measurement. The mean thickness per time-point is the representative value for each group and used for evaluation in section 5.2.

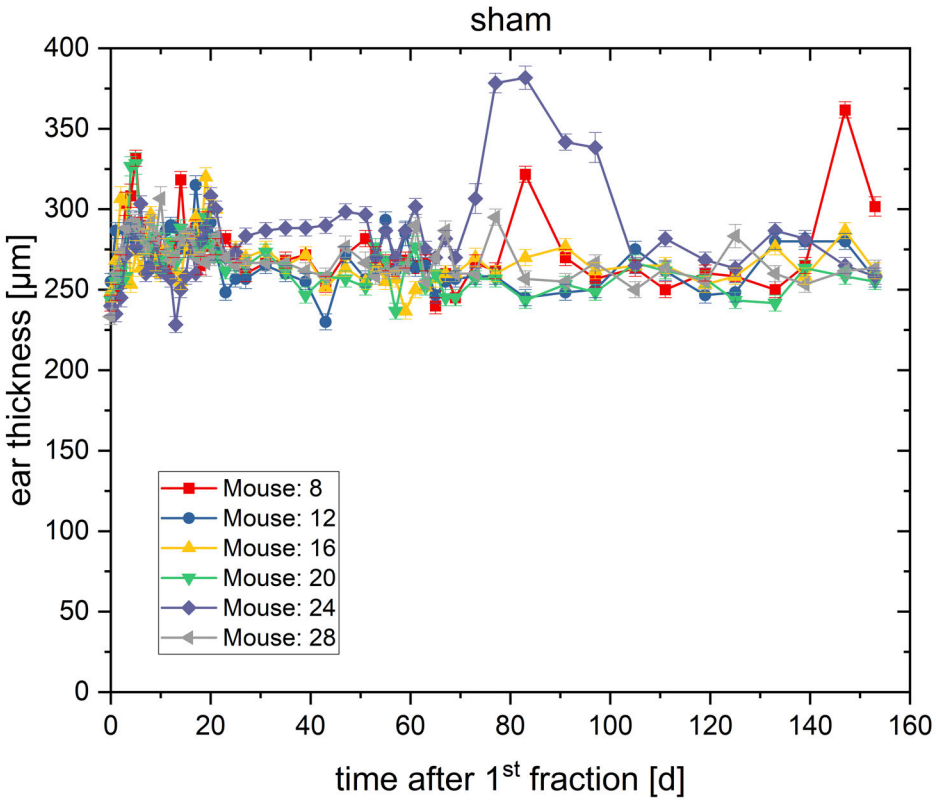

Figure B.1: *Ear thickness (± SEM) over the monitoring period of 160 days of each mouse for the sham-irradiated ear (0 Gy; control group).*

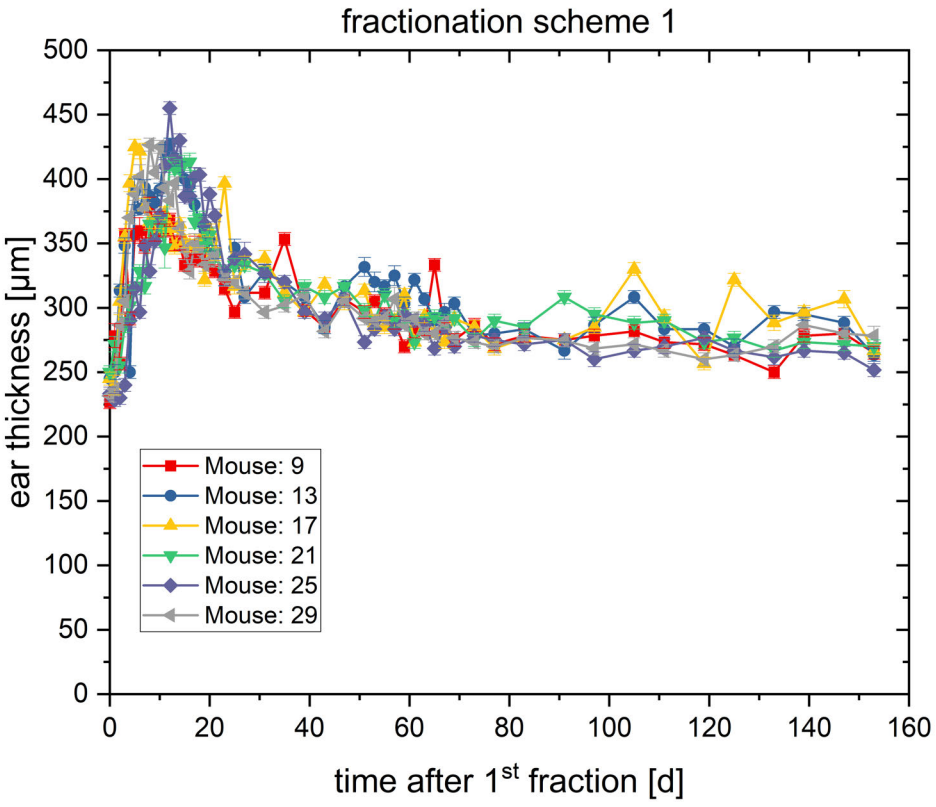

Figure B.2: *Ear thickness (± SEM) over the monitoring period of 160 days of each mouse irradiated with fractionation scheme 1.*

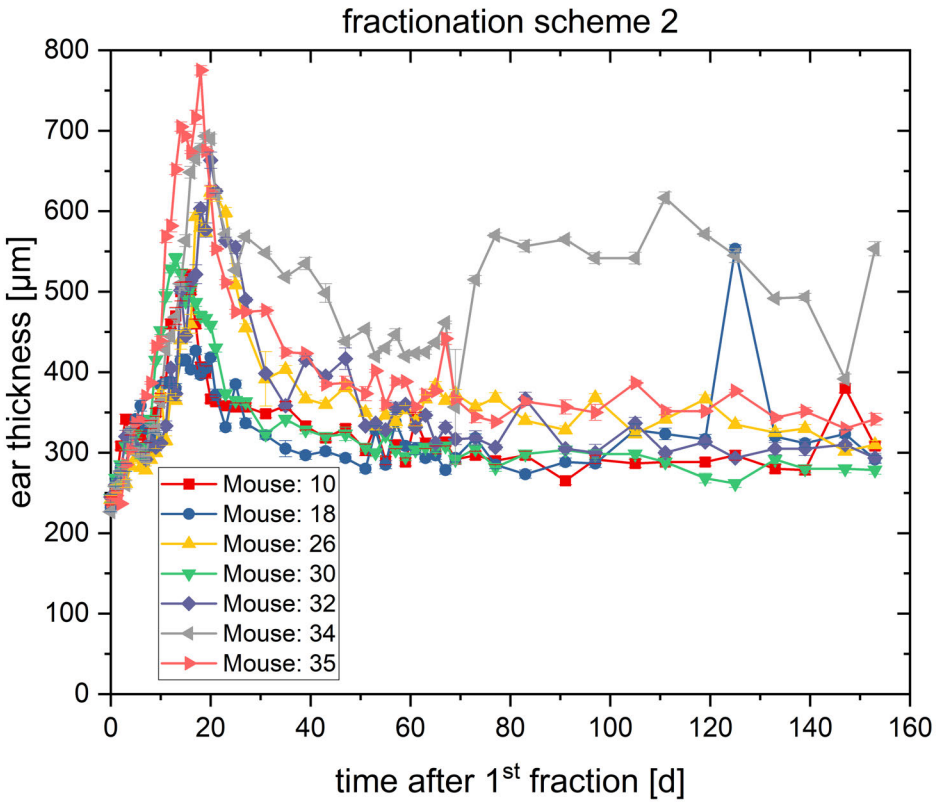

Figure B.3: *Ear thickness (± SEM) over the monitoring period of 160 days of each mouse irradiated with fractionation scheme 2.*

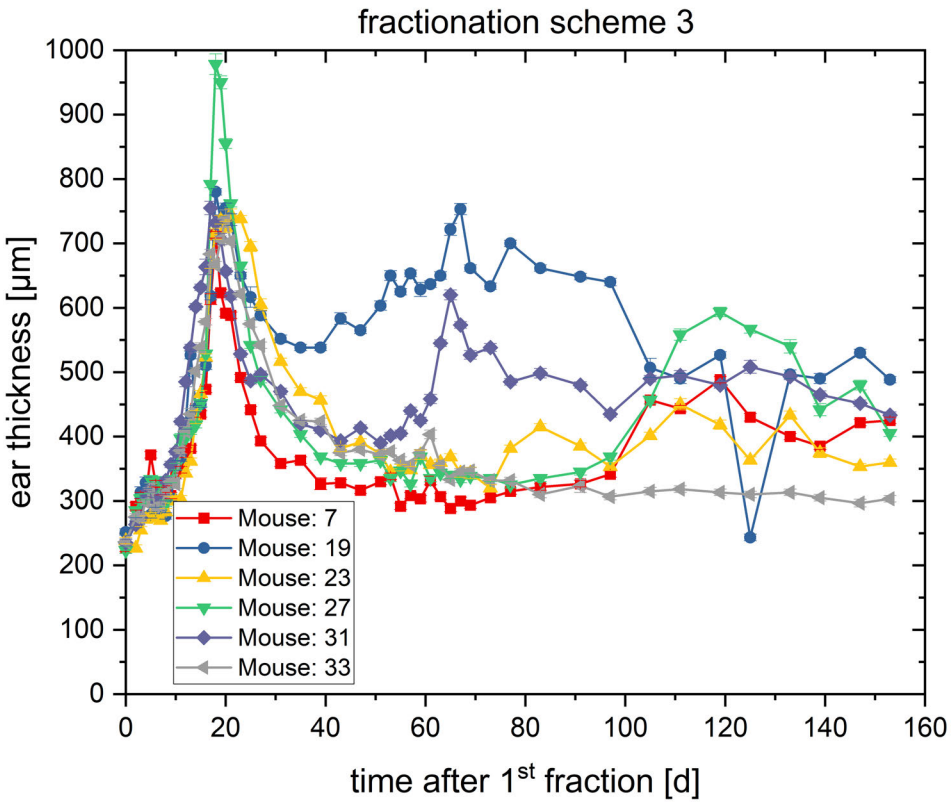

Figure B.4: *Ear thickness (± SEM) over the monitoring period of 160 days of each mouse irradiated with fractionation scheme 3.*

Bibliography

[1] F. Bray, J. Ferlay, I. Soerjomataram et al., *Global cancer statistics 2018: GLOBOCAN estimates of incidence and mortality worldwide for 36 cancers in 185 countries*, CA: a cancer journal for clinicians **68** (2018) 394–424.

[2] G. Delaney, S. Jacob, C. Featherstone et al., *The role of radiotherapy in cancer treatment: estimating optimal utilization from a review of evidence-based clinical guidelines*, Cancer: Interdisciplinary International Journal of the American Cancer Society **104** (2005) 1129–1137.

[3] P. Dirix, S. Nuyts, *Evidence-based organ-sparing radiotherapy in head and neck cancer*, The Lancet Oncology **11** (2010) 85–91.

[4] A. Tran, J. Zhang, K. Woods et al., *Treatment planning comparison of IMPT, VMAT and 4π radiotherapy for prostate cases*, Radiation Oncology **12** (2017) 1–9.

[5] *Particle Therapy Co-Operative Group*, URL http://www.ptcog.ch, 2021.

[6] B. Jones, D.AL. Morgan, *4 Radiotherapy fractionation*, in *Radiobiological Modelling in Radiation Oncology*, pp. 51–78, The British Institute of Radiology, 2007.

[7] E.B. Podgorsak et al., *Radiation oncology physics: a handbook for teachers and students*, International Atomic Energy Agency, 2005.

[8] E.J. Hall, *2 Review of essential and topical radiobiology*, in *Radiobiological Modelling in Radiation Oncology*, pp. 12–34, The British Institute of Radiology, 2007.

[9] A. Köhler, *Theorie einer Methode, bisher unmöglich unanwendbar hohe Dosen Röntgenstrahlen in der Tiefe des Gewebes zur therapeutischen Wirksamkeit zu bringen ohne schwere Schädigung des Patienten, zugleich eine Methode des Schutzes gegen Röntgenverbrennung überhaupt*, Fortschritte auf dem Gebiet der Röntgenstrahlen **14** (1909) 27–29.

[10] A. Köhler, *Röntgentiefentherapie mit Metallnetzschutz*, Strahlentherapie **1** (1912) 1.

[11] H. Marks, *Clinical experience with irradiation through a grid*, Radiology **58** (1952) 338–342.

[12] B. Jolles, *Radiotherapy of accessible malignant tumours by alternating chessboard method*, The Lancet **254** (1949) 603–606.

[13] B. Jolles, *The study of connective-tissue reaction to radiation. The sieve or chess method*, British Journal of Cancer **3** (1949) 27.

[14] W. Harris, *Recent clinical experience with the grid in the x-ray treatment of advanced cancer: preliminary report*, Radiology **58** (1952) 343–350.

[15] M. Mohiuddin, D.L. Curtis, W.T. Grizos et al., *Palliative treatment of advanced cancer using multiple nonconfluent pencil beam radiation: a pilot study*, Cancer **66** (1990) 114–118.

[16] H.R. Withers, J.M.G. Taylor, B. Maciejewski, *Treatment volume and tissue tolerance*, International Journal of Radiation Oncology* Biology* Physics **14** (1988) 751–759.

[17] J.W. Hopewell, K.R. Trott, *Volume effects in radiobiology as applied to radiotherapy*, Radiotherapy and Oncology **56** (2000) 283–288.

[18] W. Zeman, H.J. Curtis, C.P. Baker, *Histopathologic effect of high-energy-particle microbeams on the visual cortex of the mouse brain*, Radiation research **15** (1961) 496–514.

[19] H.J. Curtis, *The effect of a deuteron microbeam on graying of hair*, Radiation research **18** (1963) 510–515.

[20] H. Blattmann, W. Burkard, V. Djonov et al., *Microbeam irradiation of the chorio-allantoic membrane (CAM) of chicken embryo*, **178** (2002) 118–118.

[21] R. Serduc, P. Vérant, J.-C. Vial et al., *In vivo two-photon microscopy study of short-term effects of microbeam irradiation on normal mouse brain microvasculature*, International Journal of Radiation Oncology* Biology* Physics **64** (2006) 1519–1527.

[22] D.N. Slatkin, F.A. Dilmanian, P.O. Spanne, *Method for microbeam radiation therapy*, 1994, US Patent 5,339,347.

[23] E. Bräuer-Krisch, H. Requardt, P. Regnard et al., *New irradiation geometry for microbeam radiation therapy*, Physics in medicine and biology **50** (2005) 3103.

[24] J.A. Laissue, G. Geiser, P.O. Spanne et al., *Neuropathology of ablation of rat gliosarcomas and contiguous brain tissues using a microplanar beam of synchrotron-wiggler-generated X rays*, International Journal of Cancer **78** (1998) 654–660.

[25] D.J. Anschel, A. Bravin, P. Romanelli, *Microbeam radiosurgery using synchrotron-generated submillimetric beams: a new tool for the treatment of brain disorders*, Neurosurgical Review **34** (2011) 133–142.

[26] F.A. Dilmanian, A.G. Meek, *Heavy ion therapy with microbeams*, 2012, US Patent 8,269,198.

[27] F.A. Dilmanian, A. Rusek, G.R. Fois et al., *Interleaved carbon minibeams: An experimental radiosurgery method with clinical potential*, International Journal of Radiation Oncology* Biology* Physics **84** (2012) 514–519.

[28] P. Peschke, C.P. Karger, M. Scholz et al., *Relative biological effectiveness of carbon ions for local tumor control of a radioresistant prostate carcinoma in the rat*, International Journal of Radiation Oncology* Biology* Physics **79** (2011) 239–246.

[29] O. Zlobinskaya, S. Girst, C. Greubel et al., *Reduced side effects by proton microchannel radiotherapy: study in a human skin model*, Radiation and Environmental Biophysics **52** (2013) 123–133.

[30] Y. Prezado, G.R. Fois, *Proton-minibeam radiation therapy: A proof of concept*, Medical Physics **40** (2013) 031712.

[31] S. Girst, C. Greubel, J. Reindl et al., *Proton minibeam radiation therapy reduces side effects in an in vivo mouse ear model*, International Journal of Radiation Oncology* Biology* Physics **95** (2016) 234–241.

[32] Y. Prezado, G. Jouvion, D. Hardy et al., *Proton minibeam radiation therapy spares normal rat brain: Long-Term Clinical, Radiological and Histopathological Analysis*, Scientific Reports **7** (2017) 1–7.

[33] Y. Prezado, G. Jouvion, A. Patriarca et al., *Proton minibeam radiation therapy widens the therapeutic index for high-grade gliomas*, Scientific Reports **8** (2018) 1–10.

[34] Y. Prezado, G. Jouvion, C. Guardiola et al., *Tumor control in RG2 glioma-bearing rats: a comparison between proton minibeam therapy and standard proton therapy*, International Journal of Radiation Oncology* Biology* Physics **104** (2019) 266–271.

[35] C. Lamirault, E. Brisebard, A. Patriarca et al., *Spatially Modulated Proton Minibeams Results in the Same Increase of Lifespan as a Uniform Target Dose Coverage in F98-Glioma-Bearing Rats*, **194** (2020) 715–723.

[36] C. Greubel, *Einfluss der zeitlichen und räumlichen Fokussierung auf die strahlenbiologische Wirksamkeit von Protonen*, PhD thesis, Universität der Bundeswehr München, 2013.

[37] H.H. Rossi, *The role of microdosimetry in radiobiology*, Radiation and Environmental Biophysics **17** (1979) 29–40.

[38] A. Lechner, *CERN: Particle interactions with matter*, CERN Yellow Reports School Proceedings **5** (2018) 47.

[39] Aafke Christine Kraan, *Range verification methods in particle therapy: underlying physics and Monte Carlo modeling*, Frontiers in Oncology **5** (2015) 150.

[40] J.F. Ziegler, *Stopping of energetic light ions in elemental matter*, Journal of Applied Physics **85** (1999) 1249–1272.

[41] P. Sigmund, *Particle penetration and radiation effects volume 2*, in *Springer*, Vol. 179, Springer, 2014.

[42] W.T. Chu, B.A. Ludewigt, T.R. Renner, *Instrumentation for treatment of cancer using proton and light-ion beams*, Review of Scientific Instruments **64** (1993) 2055–2122.

[43] T. Bortfeld, *An analytical approximation of the Bragg curve for therapeutic proton beams*, Medical Physics **24** (1997) 2024–2033.

[44] B. Glimelius, U. Isacsson, E. Blomquist et al., *Potential gains using high-energy protons for therapy of malignant tumours*, Acta Oncologica **38** (1999) 137–145.

[45] H. Suit, S. Goldberg, A. Niemierko et al., *Proton beams to replace photon beams in radical dose treatments*, Acta Oncologica **42** (2003) 800–808.

[46] M.J. Berger, J.S. Coursey, M.A. Zucker et al., *Stopping-power and range tables for electrons, protons, and helium ions*, NIST Physics Laboratory Gaithersburg, MD, 1998.

[47] A. Chatterjee, H.J. Schaefer, *Microdosimetric structure of heavy ion tracks in tissue*, Radiation and Environmental Biophysics **13** (1976) 215–227.

[48] A. Chatterjee, W.R. Holley, *Energy deposition mechanisms and biochemical aspects of DNA strand breaks by ionizing radiation*, International Journal of Quantum Chemistry **39** (1991) 709–727.

[49] J.L. Gervasoni, S. Cruz-Jiménez, *Bohr's adiabatic criterion and effective charge of heavy ions*, Radiation Physics and Chemistry **48** (1996) 433–436.

[50] E. Rutherford, *The scattering of α and β particles by matter and the structure of the atom*, The London, Edinburgh, and Dublin Philosophical Magazine and Journal of Science **21** (1911) 669–688.

[51] W.D. Newhauser, R. Zhang, *The physics of proton therapy*, Physics in Medicine & Biology **60** (2015) R155.

[52] G. Moliere, *Theorie der Streuung schneller geladener Teilchen II Mehrfach-und Vielfachstreuung*, Zeitschrift für Naturforschung **3** (1948) 78–97.

[53] W.T. Scott, *Mean-value calculations for projected multiple scattering*, Physical Review **85** (1952) 245.

[54] H.A. Bethe, *Moliere's theory of multiple scattering*, Physical Review **89** (1953) 1256.

[55] G.R. Lynch, O.I. Dahl, *Approximations to multiple Coulomb scattering*, Nuclear Instruments and Methods in Physics Research Section B: Beam Interactions with Materials and Atoms **58** (1991) 6–10.

[56] G. Shen, C. Ankenbrandt, M. Atac et al., *Measurement of multiple scattering at 50 to 200 GeV/c*, Physical Review **20** (1979) 1584.

[57] B. Gottschalk, A.M. Koehler, R.J. Schneider et al., *Multiple Coulomb scattering of 160 MeV protons*, Nuclear Instruments and Methods in Physics Research Section B: Beam Interactions with Materials and Atoms **74** (1993) 467–490.

[58] V.L. Highland, *Some practical remarks on multiple scattering*, Nuclear Instruments and Methods **129** (1975) 497–499.

[59] S. Nill, *Development and application of a multi-modality inverse treatment planning system*, PhD thesis, University of Heidelberg, 2001.

[60] F. Kamp, *Comparison of the Lateral Dose Fall-Off for Proton and Ion Beams in Radiation Therapy*, diploma thesis, TU München, 2011.

[61] E. Pedroni, S. Scheib, T. Böhringer et al., *Experimental characterization and physical modelling of the dose distribution of scanned proton pencil beams*, Physics in Medicine & Biology **50** (2005) 541.

[62] H. Lodish, A. Berk, C.A. Kaiser et al., *Molecular cell biology*, Macmillan, 2008.

[63] A. Hauptner, W. Friedland, S. Dietzel et al., *Spatial distribution of DNA double-strand breaks from ion tracks*, The Royal Danish Academy of Sciences and Letters **52** (2006) 59–85.

[64] G.P. van der Schans, J.F. Bleichrodt, J. Blok, *Contribution of various types of damage to inactivation of a biologically-active double-stranded circular DNA by gamma-radiation*, International Journal of Radiation Biology **23** (1973) 133–150.

[65] K.K. Khanna, S.P. Jackson, *DNA double-strand breaks: signaling, repair and the cancer connection*, Nature genetics **27** (2001) 247–254.

[66] H. Nikjoo, P. O'Neill, M. Terrissol et al., *Quantitative modelling of DNA damage using Monte Carlo track structure method*, Radiation and Environmental Biophysics **38** (1999) 31–38.

[67] N.AP. Franken, H.M. Rodermond, J. Stap et al., *Clonogenic assay of cells in vitro*, Nature Protocols **1** (2006) 2315–2319.

[68] T. Friedrich, U. Scholz, T. Elsässer et al., *Systematic analysis of RBE and related quantities using a database of cell survival experiments with ion beam irradiation*, Journal of Radiation Research **54** (2013) 494–514.

[69] D.S. Chang, F.D. Lasley, I.J. Das et al., *Basic Radiotherapy Physics and Biology*, Springer, 2014.

[70] Stephen Joseph McMahon, *The linear quadratic model: usage, interpretation and challenges*, Physics in Medicine & Biology **64** (2018) 01TR01.

[71] L.M. Garcia, D.E. Wilkins, G.P. Raaphorst, *α/β ratio: a dose range dependence study*, International Journal of Radiation Oncology* Biology* Physics **67** (2007) 587–593.

[72] J.P. Kirkpatrick, J.J. Meyer, L.B. Marks, *The linear-quadratic model is inappropriate to model high dose per fraction effects in radiosurgery*, Seminars in Radiation Oncology **18** (2008) 240–243.

[73] M. Astrahan, *Some implications of linear-quadratic-linear radiation dose-response with regard to hypofractionation*, Medical Physics **35** (2008) 4161–4172.

[74] T. Elsässer, M. Krämer, M. Scholz, *Accuracy of the local effect model for the prediction of biologic effects of carbon ion beams in vitro and in vivo*, International Journal of Radiation Oncology* Biology* Physics **71** (2008) 866–872.

[75] H. Paganetti, A. Niemierko, M. Ancukiewicz et al., *Relative biological effectiveness (RBE) values for proton beam therapy*, International Journal of Radiation Oncology* Biology* Physics **53** (2002) 407–421.

[76] M.C. Joiner, A. Van der Kogel, *Basic clinical radiobiology fourth edition*, CRC press, 2009.

[77] S. Li, M. Kennedy, S. Payne et al., *Model of tumor dormancy/recurrence after short-term chemotherapy*, PLoS ONE **9** (2014) e98021.

[78] E.J. Hall, A.J. Giaccia et al., *Radiobiology for the Radiologist*, Vol. 6, Lippincott Williams & Wilkins, 2006.

[79] P.C. Feyer, E. Maranzano, A. Molassiotis et al., *Radiotherapy-induced nausea and vomiting (RINV): MASCC/ESMO guideline for antiemetics in radiotherapy: update 2009*, Supportive Care in Cancer **19** (2011) 5–14.

[80] J. Johansen, S.M. Bentzen, J. Overgaard et al., *Relationship between the in vitro radiosensitivity of skin fibroblasts and the expression of subcutaneous fibrosis, telangiectasia, and skin erythema after radiotherapy*, Radiotherapy and Oncology **40** (1996) 101–109.

[81] S. Gollins, C. Gaffney, S. Slade et al., *RCT on gentian violet versus a hydrogel dressing for radiotherapy-induced moist skin desquamation*, Journal of Wound Care **17** (2008) 268–275.

[82] R. Henriksson, L. Franzen, B. Littbrand, *Effects of sucralfate on acute and late bowel discomfort following radiotherapy of pelvic cancer.*, Journal of Clinical Oncology **10** (1992) 969–975.

[83] O. Al-Mefty, J.E. Kersh, A. Routh et al., *The long-term side effects of radiation therapy for benign brain tumors in adults*, Journal of Neurosurgery **73** (1990) 502–512.

[84] A.G. Meek, *Breast radiotherapy and lymphedema*, Cancer: Interdisciplinary International Journal of the American Cancer Society **83** (1998) 2788–2797.

[85] C.W. Taylor, A. Nisbet, P. McGale et al., *Cardiac exposures in breast cancer radiotherapy: 1950s–1990s*, International Journal of Radiation Oncology* Biology* Physics **69** (2007) 1484–1495.

[86] K. Bruheim, M.G. Guren, E. Skovlund et al., *Late side effects and quality of life after radiotherapy for rectal cancer*, International Journal of Radiation Oncology* Biology* Physics **76** (2010) 1005–1011.

[87] Y.B. Pan, Y. Maeda, A. Wilson et al., *Late gastrointestinal toxicity after radiotherapy for anal cancer: a systematic literature review*, Acta Oncologica **57** (2018) 1427–1437.

[88] J.M. Straub, J. New, C.D. Hamilton et al., *Radiation-induced fibrosis: mechanisms and implications for therapy*, Journal of Cancer Research and Clinical Oncology **141** (2015) 1985–1994.

[89] A. Dasu, I. Toma-Dasu, *Models for the risk of secondary cancers from radiation therapy*, Physica Medica **42** (2017) 232–238.

[90] E.J. Hall, C.-S. Wuu, *Radiation-induced second cancers: the impact of 3D-CRT and IMRT*, International Journal of Radiation Oncology* Biology* Physics **56** (2003) 83–88.

[91] D.A. Bush, J.D. Slater, B.B. Shin et al., *Hypofractionated proton beam radiotherapy for stage I lung cancer*, Chest **126** (2004) 1198–1203.

[92] I. Shuryak, D.J. Carlson, J.M. Brown et al., *High-dose and fractionation effects in stereotactic radiation therapy: Analysis of tumor control data from 2965 patients*, Radiotherapy and Oncology **115** (2015) 327–334.

[93] S.M. McBride, D.S. Wong, J.J. Dombrowski et al., *Hypofractionated stereotactic body radiotherapy in low-risk prostate adenocarcinoma: Preliminary results of a multi-institutional phase 1 feasibility trial*, Cancer **118** (2012) 3681–3690.

[94] W.E. Straile, H.B. Chase, *The use of elongate microbeams of x-rays for simulating the effects of cosmic rays on tissues: a study of wound healing and hair follicle regeneration*, Radiation research **18** (1963) 65–75.

[95] F. Liberson, *The value of a multi-perforated screen in deep X-ray therapy: A preliminary report on a new method of delivering multiple erythema doses without permanent injury to the skin*, Radiology **20** (1933) 186–195.

[96] R.J. Griffin, N.A. Koonce, R.P.M. Dings et al., *Microbeam radiation therapy alters vascular architecture and tumor oxygenation and is enhanced by a galectin-1 targeted anti-angiogenic peptide*, Radiation Research **177** (2012) 804–812.

[97] S.L. Morgan-Fletcher, *Prescribing, recording and reporting photon beam therapy (Supplement to ICRU Report 50)*, 2001.

[98] International Commission on Radiation Units, *Prescribing, recording, and reporting photon beam therapy*, Vol. 50, International Commission on Radiation, 1993.

[99] M. Sammer, C. Greubel, S. Girst et al., *Optimization of beam arrangements in proton minibeam radiotherapy by cell survival simulations*, Medical Physics **44** (2017) 6096–6104.

[100] G. Datzmann, *Aufbau und Charakterisierung des Hochenergie Rasterionen-mikroskops SNAKE*, PhD thesis, TU München, 2002.

[101] P. Reichart, G. Datzmann, A. Hauptner et al., *Three-dimensional hydrogen microscopy in diamond*, Science **306** (2004) 1537–1540.

[102] G. Datzmann, G. Dollinger, G. Hinderer et al., *A Superconducting Multipole Lense for Focusing High Energy Ions*, Nuclear Instruments and Methods in Physics Research Section B: Beam Interactions with Materials and Atoms **158** (1999) 74–80.

[103] G. Hinderer, G. Dollinger, G. Datzmann, H.J. Körner, *Design of the new superconducting microprobe system in Munich*, Nuclear Instruments and Methods in Physics Research Section B: Beam Interactions with Materials and Atoms **130** (1997) 51–56.

[104] A. Hauptner, *Mikroskopisch genaue Zellbestrahlung mit hochenergetischen Ionen*, PhD thesis, TU München, 2006.

[105] V. Hable, *Echtzeitbeobachtung schneller Reaktionskinetiken in lebenden Zellen nach Ionenmikrobestrahlung*, PhD thesis, Universität der Bundeswehr München, 2011.

[106] C. Siebenwirth, C. Greubel, G.A. Drexler et al., *Local inhibition of rRNA transcription without nucleolar segregation after targeted ion irradiation of the nucleolus*, Journal of Cell Science **132** (2019) jcs232181.

[107] T. Friedrich, K. Ilicic, C. Greubel et al., *DNA damage interactions on both nanometer and micrometer scale determine overall cellular damage*, Scientific Reports **8** (2018) 1–10.

[108] T. Friedrich, K. Ilicic, C. Greubel et al., *Author Correction: DNA damage interactions on both nanometer and micrometer scale determine overall cellular damage*, Scientific Reports **10** (2020) 1–2.

[109] S. Girst, *Proton minibeam radiotherapy*, PhD thesis, Universität der Bundeswehr München, 2016.

[110] W. Assmann, J. De Boer, U. Meyer-Berkhout et al., *The munich mp tandem*, Nuclear Instruments and Methods **122** (1974) 191–203.

[111] G. Dollinger, *Kohlenstoffolien als Stripper für schwere Ionen*, PhD thesis, TU München, 1990.

[112] V. Hable, C. Greubel, A. Bergmaier et al., *The live cell irradiation and observation setup at SNAKE*, Nuclear Instruments and Methods in Physics Research Section B: Beam Interactions with Materials and Atoms **267** (2009) 2090–2097.

[113] S. Girst, C. Greubel, J. Reindl et al., *The influence of the channel size on the reduction of side effects in microchannel proton therapy*, Radiation and Environmental Biophysics **54** (2015) 335–342.

[114] *MATLAB*, URL http://www.mathworks.com/.

[115] P.TC. So, H. Kim, I.E. Kochevar, *Two-photon deep tissue ex vivo imaging of mouse dermal and subcutaneous structures*, Optics Express **3** (1998) 339–350.

[116] V.W. Wong, M. Sorkin, J.P. Glotzbach et al., *Surgical approaches to create murine models of human wound healing*, Journal of Biomedicine and Biotechnology **2011** (2010).

[117] J.P. Williams, S.L. Brown, G.E. Georges et al., *Animal models for medical countermeasures to radiation exposure*, Radiation research **173** (2010) 557–578.

[118] M. Sammer, E. Zahnbrecher, S. Dobiasch et al., *Proton pencil minibeam irradiation of an in-vivo mouse ear model spares healthy tissue dependent on beam size*, PLoS ONE **14** (2019) e0224873.

[119] Y. Wengström, C. Forsberg, I. Näslund et al., *Quantitative assessment of skin erythema due to radiotherapy evaluation of different measurements*, Radiotherapy and Oncology **72** (2004) 191–197.

[120] Mosby, *Mosby's Medical Dictionary*, Elsevier, 9th edition, 2013.

[121] C. Has, *Peeling skin disorders: a paradigm for skin desquamation*, Journal of Investigative Dermatology **138** (2018) 1689–1691.

[122] S.M. Jackson, M.L. Williams, K.R. Feingold et al., *Pathobiology of the stratum corneum.*, Western Journal of Medicine **158** (1993) 279.

[123] J.L. Ryan, *Ionizing radiation: the good, the bad, and the ugly*, Journal of Investigative Dermatology **132** (2012) 985–993.

[124] C.S. Potten, R. Saffhill, H.I. Maibach, *Measurement of the transit time for cells through the epidermis and stratum corneum of the mouse and guinea-pig*, Cell Proliferation **20** (1987) 461–472.

[125] A.C. Dombrowsky, J. Schauer, M. Sammer et al., *Acute skin damage and late radiation-induced fibrosis and inflammation in murine ears after high-dose irradiation*, Cancers **11** (2019) 727.

[126] M.A. Delesse, *Procédé mécanique pour déterminer la composition des roches.*, Comptes rendus de l'Académie des sciences **25** (1847) 544–545.

[127] V. Howard, M. Reed, *Unbiased stereology: three-dimensional measurement in microscopy*, Garland Science, 2004.

[128] M. Sammer, K. Teiluf, S. Girst et al., *Beam size limit for pencil minibeam radiotherapy determined from side effects in an in-vivo mouse ear model*, PLoS ONE **14** (2019) e0221454.

[129] W. Liao, T.K. Hei, S.K. Cheng, *Radiation-induced dermatitis is mediated by IL17-expressing $\gamma\delta$ T cells*, Radiation Research **187** (2017) 464–474.

[130] E.K. Parkinson, W.J. Hume, C.S. Potten, *The radiosensitivity of keratinocytes from tongue and skin; enhanced radioresistance following serial cultivation*, British Journal of Cancer **7** (1986) 81.

[131] F.A. Dilmanian, J.G. Eley, A. Rusek et al., *Charged particle therapy with mini-segmented beams*, Frontiers in Oncology **5** (2015) 269.

[132] E. Bräuer-Krisch, A. Bravin, M. Lerch et al., *MOSFET dosimetry for microbeam radiation therapy at the European Synchrotron Radiation Facility*, Medical Physics **30** (2003) 583–589.

[133] Y. Prezado, S. Thengumpallil, M. Renier et al., *X-ray energy optimization in minibeam radiation therapy*, Medical Physics **36** (2009) 4897–4902.

[134] G. Wang, W.-L. Wang, Y.-Q. Liu et al., *Positioning error and expanding margins of planning target volume with kilovoltage cone beam computed tomography for prostate cancer radiotherapy*, OncoTargets and Therapy **11** (2018) 1981.

[135] F.A. Dilmanian, Y. Qu, L.E. Feinendegen et al., *Tissue-sparing effect of x-ray microplanar beams particularly in the CNS: Is a bystander effect involved?*, Experimental Hematology **35** (2007) 69–77.

[136] T. Henry, N. Bassler, A. Ureba et al., *Development of an interlaced-crossfiring geometry for proton grid therapy*, Acta Oncologica **56** (2017) 1437–1443.

[137] R. Serduc, E. Bräuer-Krisch, E.A. Siegbahn, et al., *High-precision radiosurgical dose delivery by interlaced microbeam arrays of high-flux low-energy synchrotron X-rays*, PLoS ONE **5** (2010) e9028.

[138] T. Henry, J. Ödén, *Interlaced proton grid therapy–Linear energy transfer and relative biological effectiveness distributions*, Physica Medica **56** (2018) 81–89.

[139] L. Sun, W. Smith, A. Ghose et al., *A quantitative assessment of the consequences of allowing dose heterogeneity in prostate radiation therapy planning*, Journal of Applied Clinical Medical Physics **19** (2018) 580–590.

[140] J.O. Deasy, A.I. Blanco, V.H. Clark, *CERR: a computational environment for radiotherapy research*, Medical Physics **30** (2003) 979–985.

[141] S. Schell, J.J. Wilkens, *Advanced treatment planning methods for efficient radiation therapy with laser accelerated proton and ion beams*, Medical Physics **37** (2010) 5330–5340.

[142] K. Parodi, A. Mairani, F. Sommerer, *Monte Carlo-based parametrization of the lateral dose spread for clinical treatment planning of scanned proton and carbon ion beams*, Journal of Radiation Research **54** (2013) i91–i96.

[143] B.G. Douglas, J.F. Fowler, *The effect of multiple small doses of x rays on skin reactions in the mouse and a basic interpretation*, Radiation Research **66** (1976) 401–426.

[144] B.D. Kavanagh, F. Newman, *Toward a unified survival curve: in regard to Park et al.(IntJ Radiat Oncol Biol Phys 2008; 70: 847-852) and Krueger et al.(Int J Radiat Oncol Biol Phys 2007; 69: 1262-1271).*, International Journal of Radiation Oncology* Biology* Physics **71** (2008) 958.

[145] M.A. Bender, P.C. Gooch, *The kinetics of X-ray survival of mammalian cells in vitro*, International Journal of Radiation Biology and Related Studies in Physics, Chemistry and Medicine **5** (1962) 133–145.

[146] M. Scholz, G. Kraft, *Calculation of heavy ion inactivation probabilities based on track structure, x ray sensitivity and target size*, Radiation Protection Dosimetry **52** (1994) 29–33.

[147] F.W. McKenna, S. Ahmad, *Fitting techniques of cell survival curves in high-dose region for use in stereotactic body radiation therapy*, Physics in Medicine & Biology **54** (2009) 1593.

[148] B.K. Lind, L.M. Persson, M.R. Edgren et al., *Repairable–conditionally repairable damage model based on dual Poisson processes*, Radiation Research **160** (2003) 366–375.

[149] D. Belkić, *Parametric analysis of time signals and spectra from perspectives of quantum physics and chemistry*, Advances in Quantum Chemistry **61** (2011) 145–260.

[150] D. Belkić, K. Belkić, *Padé–Froissart exact signal-noise separation in nuclear magnetic resonance spectroscopy*, Journal of Physics B: Atomic, Molecular and Optical Physics **44** (2011) 125003.

[151] D. Belkić, K. Belkić, *High-resolution signal processing in magnetic resonance spectroscopy for early cancer diagnostics*, Advances in Quantum Chemistry **62** (2011) 243–347.

[152] S. Gholami, H.A. Nedaie, F. Longo et al., *Grid block design based on monte carlo simulated dosimetry, the linear quadratic and Hug–Kellerer radiobiological models*, Journal of Medical Physics **42** (2017) 213.

[153] B. Andisheh, *Improving the therapeutic ratio of stereotactic radiosurgery and radiotherapy*, PhD thesis, Department of Physics, Stockholm Univeristy, 2012.

[154] C. Guardiola, Y. Prezado, C. Roulin et al., *Effect of X-ray minibeam radiation therapy on clonogenic survival of glioma cells*, Clinical and Translational Radiation Oncology **13** (2018) 7–13.

[155] R. Asur, K.T. Butterworth, J.A. Penagaricano et al., *High dose bystander effects in spatially fractionated radiation therapy*, Cancer Letters **356** (2015) 52–57.

[156] F.A. Cucinotta, E. Cacao, *Non-targeted effects models predict significantly higher mars mission cancer risk than targeted effects models*, Scientific Reports **7** (2017) 1–11.

[157] C. Fournier, P. Barberet, T. Pouthier et al., *No evidence for DNA and early cytogenetic damage in bystander cells after heavy-ion microirradiation at two facilities*, Radiation Research **171** (2009) 530–540.

[158] P. Lansonneur, H. Mammar, C. Nauraye et al., *First proton minibeam radiation therapy treatment plan evaluation*, Scientific Reports **10** (2020) 1–8.

[159] J.N. Rivera, T.M. Kierski, S.K. Kasoji et al., *Conventional dose rate spatially-fractionated radiation therapy (SFRT) treatment response and its association with dosimetric parameters–A preclinical study in a Fisher 344 rat model*, PLoS one **15** (2020) e0229053.

[160] S. Kanagavelu, S. Gupta, X. Wu et al., *In vivo effects of lattice radiation therapy on local and distant lung cancer: potential role of immunomodulation*, Radiation Research **182** (2014) 149–162.

[161] M. Mayerhofer, G. Datzmann, A. Degiovanni et al., *Magnetically focused 70 MeV proton minibeams for preclinical experiments combining a tandem accelerator and a 3 GHz linear post accelerator*, Medical Physics (2021) in press.

[162] T. Schneider, L. De Marzi, A. Patriarca et al., *Advancing proton minibeam radiation therapy: magnetically focussed proton minibeams at a clinical centre*, Scientific Reports **10** (2020) 1–10.

[163] E. Debrot, D. Bolst, B. James et al., *Investigating variable RBE in a 12C minibeam field with microdosimetry and Geant4*, Radiation Protection Dosimetry **183** (2019) 160–166.

[164] B.J. Mijnheer, J.J. Battermann, A. Wambersie, *What degree of accuracy is required and can be achieved in photon and neutron therapy?*, Radiotherapy and Oncology **8** (1987) 237–252.

[165] V. Grégoire, T.R. Mackie, *State of the art on dose prescription, reporting and recording in Intensity-Modulated Radiation Therapy (ICRU report No. 83)*, Cancer/Radiothérapie **15** (2011) 555–559.

[166] T.E. Wheldon, A.S. Michalowski, J. Kirk, *The effect of irradiation on function in self-renewing normal tissues with differing proliferative organisation*, The British Journal of Radiology **55** (1982) 759–766.

[167] M. Sammer, A.C. Dombrowsky, J. Schauer et al., *Normal Tissue Response of Combined Temporal and Spatial Fractionation in Proton Minibeam Radiation Therapy*, International Journal of Radiation Oncology* Biology* Physics **109** (2021) 76–83.

[168] W. Yan, M.K. Khan, X. Wu et al., *Spatially fractionated radiation therapy: History, present and the future*, Clinical and Translational Radiation Oncology **20** (2020) 30.

[169] T. Schneider, A. Patriarca, Y. Prezado, *Improving the dose distributions in minibeam radiation therapy: helium ions vs protons*, Medical Physics **46** (2019) 3640–3648.

[170] J.G. Eley, A.S. Chadha, C. Quini et al., *Pilot study of neurologic toxicity in mice after proton minibeam therapy*, Scientific Reports **10** (2020) 1–9.

[171] G. Datzmann, M. Sammer, S. Girst et al., *Preclinical Challenges in Proton Minibeam Radiotherapy: Physics and Biomedical Aspects*, Frontiers in Physics **8** (2020) 471.

List of publications

2017

1. Optimization of beam arrangements in proton minibeam radiotherapy by cell survival simulations
   M. Sammer, C. Greubel, S. Girst, G. Dollinger
   Medical Physics **44** (2017) 6096-6104

2018

2. DNA damage interactions on both nanometer and micrometer scale determine overall cellular damage
   T. Friedrich, K. Ilicic, C. Greubel, S. Girst, J. Reindl, **M. Sammer**, B. Schwarz, C. Siebenwirth, D.W.M. Walsh, T.E. Schmid, M. Scholz, G. Dollinger
   Scientific Reports **8** (2018) 1-10

2019

3. Acute Skin Damage and Late Radiation-Induced Fibrosis and Inflammation in Murine Ears after High-Dose Irradiation
   A.C. Dombrowsky, J. Schauer, **M. Sammer**, A. Blutke, D.W.M. Walsh, B. Schwarz, S. Bartzsch, A. Feuchtinger, J. Reindl, S.E. Combs, G. Dollinger, T.E. Schmid
   Cancers **11** (2019) 727

4. Beam size limit for pencil minibeam radiotherapy determined from side effects in an in-vivo mouse ear model
   M. Sammer, K. Teiluf, S. Girst, C. Greubel, J. Reindl, K. Ilicic, D.W.M. Walsh, M. Aichler, A. Walch, S.E. Combs, J.J. Wilkens, G. Dollinger, T.E. Schmid
   PLoS ONE **14** (2019) e0221454

5. Local inhibition of rRNA transcription without nucleolar segregation after targeted ion irradiation of the nucleolus
   C. Siebenwirth, C. Greubel, G.A. Drexler, J. Reindl, D.W.M. Walsh, B. Schwarz, **M. Sammer**, I. Baur, H. Pospiech, T.E. Schmid, G. Dollinger, A.A. Friedl
   Journal of Cell Science **132** (2019) jcs232181

6. Proton pencil minibeam irradiation of an in-vivo mouse ear model spares healthy tissue dependent on beam size
M. Sammer, E. Zahnbrecher, S. Dobiasch, S. Girst, C. Greubel, K. Ilicic, J. Reindl, B. Schwarz, C. Siebenwirth, D.W.M. Walsh, S.E. Combs, G. Dollinger, T.E. Schmid
PLoS ONE **14** (2019) e0224873

2020

7. Preclinical Challenges in Proton Minibeam Radiotherapy: Physics and Biomedical Aspects
G. Datzmann, **M. Sammer**, S. Girst, M. Mayerhofer, G. Dollinger, J. Reindl
Frontiers in Physics **8** (2020) 568206

8. Author Correction: DNA damage interactions on both nanometer and micrometer scale determine overall cellular damage
T. Friedrich, K. Ilicic, C. Greubel, S. Girst, J. Reindl, **M. Sammer**, B. Schwarz, C. Siebenwirth, D.W.M. Walsh, T.E. Schmid, M. Scholz, G. Dollinger
Scientific Reports **10** (2020) 1-2

2021

9. Normal Tissue Response of Combined Temporal and Spatial Fractionation in Proton Minibeam Radiation Therapy
M. Sammer, A.C. Dombrowsky, J. Schauer, K. Oleksenko, S. Bicher, B. Schwarz, S. Rudigkeit, N. Matejka, J. Reindl, S. Bartzsch, A. Blutke, A. Feuchtinger, S.E. Combs, G. Dollinger, T.E. Schmid
*International Journal of Radiation Oncology*Biology*Physics* **109** (2021) 76-83

10. Optimizing proton minibeam radiotherapy by interlacing and heterogeneous tumor dose on the basis of calculated clonogenic cell survival
M. Sammer, S. Girst, G. Dollinger
Scientific Reports **11** (2021) 1-16

11. High-LET radiation induced chromatin reorganization revealed by live cell microscopy and targeted microbeam irradiation
B. Schwarz, **M. Sammer**, N. Matejka, S. Rudigkeit, G. Dollinger, J. Reindl
submitted

12. A new method for biological dosimetry of high-LET particle exposure to human cells using nanoscopic imaging of DSB-repair protein clusters
J. Reindl, J. Huber, W. Friedland, S. Girst, **M. Sammer**, B. Schwarz, G. Dollinger
submitted

Acknowledgments

First of all, I want to thank Professor Dr. Günther Dollinger for his competent supervision and support starting from my master's thesis to the completion of this Ph.D. project. His pure scientific curiosity in combination with the impressive view towards scientific connections always helped to improve and exploit the collected data. I also need to mention that he was never tired of helping me out in difficult situations, especially during experimental periods, giving motivational boosts and helpful advice.

Special thanks go to my "roommates" Jannis Schauer, Michael Mayerhofer, Dietrich Walsh (off-duty) and Benjamin Schwarz (off-duty), not forgetting my kite-buddy Johannes Mitteneder, who gave me an extraordinary comfortable work environment with friendly discussions about hard (sometimes hardly about) science. I also want to thank my proton minibeam predecessor and colleague Stefanie Girst for her neat corrections of my writings as well as the scientific discussions of pMBRT and our common field of applied children research. Many thanks go also to my colleagues Judith Reindl, Sarah Rudigkeit, Nicole Matejka, and former colleagues Christian Siebenwirth, and Christoph Greubel, who always helped and supported me throughout my projects.

I also want to thank Prof. Thomas Schmid and his biology team, especially Annique Dombrowsky, who was my counterpart from the biology side, for the invaluable support and motivation to successfully conduct these interdisciplinary experiments.

Furthermore, I want to thank the whole team of the LRT2 department for the discussions, advice, and all the support I got during this work. Special appreciation goes to Ralf Schubert for his constructions and the priceless advice for the mouse holder design and its positioning system. Many thanks are due to all operators of the MLL, above all to Sigfried Koschartz, for their competent work and willingness to exploit the tandem till its last nA.

Finally, I am also very thankful to all my friends and family. Above all, I want to thank my wife Filipa who always supports me in every possible way. She in combination with our dear daughter Luisa makes any stressful work-day disappear in the blink of an eye. And last but not least, many thanks go to my parents, who made my entire education and studies possible, especially by always having my back and believing without a doubt in what I was doing.